VOLATILES IN BASALTIC MAGMAS FROM CENTRAL MEXICO: FROM SUBDUCTION TO ERUPTION

by

EMILY RENEE JOHNSON

A DISSERTATION

Presented to the Department of Geological Sciences
and the Graduate School of the University of Oregon
in partial fulfillment of the requirements
for the degree of
Doctor of Philosophy

June 2008

University of Oregon Graduate School

Confirmation of Approval and Acceptance of Dissertation prepared by:

Emily Johnson

Title:

"Volatiles in basaltic magmas from central Mexico: from subduction to eruption "

This dissertation has been accepted and approved in partial fulfillment of the requirements for the Doctor of Philosophy degree in the Department of Geological Sciences by:

Paul Wallace, Chairperson, Geological Sciences
Katharine Cashman, Member, Geological Sciences
A. Dana Johnston, Member, Geological Sciences
Patricia McDowell, Outside Member, Geography

and Richard Linton, Vice President for Research and Graduate Studies/Dean of the Graduate School for the University of Oregon.

June 14, 2008

Original approval signatures are on file with the Graduate School and the University of Oregon Libraries.

An Abstract of the Dissertation of

Emily Renee Johnson for the degree of Doctor of Philosophy

in the Department of Geological Sciences to be taken June 2008

Title: VOLATILES IN BASALTIC MAGMAS FROM CENTRAL MEXICO: FROM SUBDUCTION TO ERUPTION

Approved: _____

Dr. Paul J. Wallace

Volatiles, particularly H_2O, play an important role in subduction zone magmatism, from instigating melting of the mantle wedge to influencing the explosivity of eruptions at the surface. To better understand both small-scale eruptive processes and large-scale melt generation processes, concentrations of H_2O, CO_2, Cl and S were measured in olivine-hosted melt inclusions from nine monogenetic volcanoes across the Michoacán-Guanajuato Volcanic Field (MGVF) in central Mexico.

Melt inclusions, tiny blebs of melt trapped within crystals during growth, record pre-eruptive melt compositions and dissolved volatile contents. Analyses of olivine-hosted melt inclusions from the long-lived (15 years) eruption of Volcán Jorullo illustrate the complexities of cinder cone eruptions. The later-erupted melt inclusions record decreases in crystallization depths, increases in magma storage time, and shallow

assimilation of granitic bedrock, suggesting significant evolution of the magma plumbing system over time.

Because melt inclusions are trapped at variable depths during magma crystallization, they record progressive degassing of melts during ascent and eruption. Degassing of basaltic melts is variable due to differences in solubility of the volatile components. Estimated volatile solubilities based on variations in melt inclusion data for the MGVF suggest that Cl and S have high solubility, with little to no degassing of these species during ascent and eruption, whereas H_2O and CO_2 show evidence of substantial degassing. Furthermore, increases in concentrations of incompatible elements in melt inclusions correlate with extents of degassing, suggesting that degassing during ascent drives melt crystallization in many cinder cone eruptions.

The volatile contents of mafic arc magmas as revealed by melt inclusions reflect the influx of H_2O-rich components from the subducted slab to the mantle wedge. Across-arc patterns in volatile and incompatible trace element concentrations for MGVF magmas show that the flux of H_2O-rich subduction components remains high for large distances across the arc. These data, combined with oxygen isotope analyses of olivine phenocrysts and 2-D thermo-mechanical models of the subduction zone, suggest a complex origin for the H_2O-rich subduction components, involving dehydration of subducted sediment and storage of volatiles in hydrous minerals in the mantle wedge.

This dissertation includes co-authored materials both previously published and submitted for publication.

CURRICULUM VITAE

NAME OF AUTHOR: Emily Renee Johnson

PLACE OF BIRTH: Utah, USA

GRADUATE AND UNDERGRADUATE SCHOOLS ATTENDED:

University of Oregon, Eugene, OR

University of Michigan, Ann Arbor, MI

DEGREES AWARDED:

Doctor of Philosophy in Geological Sciences, 2008, University of Oregon

Bachelor of Science, 2003, University of Michigan
High Honors in Geological Science

AREAS OF SPECIAL INTEREST:

Igneous Petrology and Geochemistry

Volcanology

GRANTS, AWARDS AND HONORS:

Geological Society of America Student Grant, 2006

Staples Fellowship, Department of Geological Sciences, University of Oregon, 2004

Academic Excellence Award, Department of Geological Sciences, University of Michigan, 2003

Camp Davis Field Geologist Award, Department of Geological Sciences, University of Michigan, 2002

PUBLICATIONS:

Johnson, E.R., Wallace, P.J., Cashman, K.V., Delgado Granados, H., Kent, A.J.R., 2008. Magmatic volatile contents and degassing-induced crystallization at Volcán Jorullo, Mexico: Implications for melt evolution and the plumbing systems of monogenetic volcanoes. Earth Planet. Sci. Lett. doi:10.1016/j.epsl.2008.03.004.

Pioli, L., Erlund, E., Johnson, E., Cashman, K., Wallace, P., Rosi, M., Delgado Granados, H., 2008. Explosive dynamics of violent Strombolian eruptions: The eruption of Parícutin Volcano 1943-1952 (Mexico). Earth Planet. Sci. Lett. doi:10.1016/j.epsl.2008.04.026.

Johnson, E.R., Wallace, P.J., Manea, V.C., 2007. Using H_2O and trace element ratios to produce a spatial map of magmatic H_2O contents throughout the Trans-Mexican Volcanic Belt, Eos Trans. AGU, 88(52), Fall Meet. Suppl., Abstract V31H-02.

Johnson, E.R., Wallace, P., Delgado Granados, H., 2007. Across-arc Volatile Variations in the Michoacán-Guanajuato Volcanic Field, Mexico: Investigating Slab Devolatilization and the Mantle Source of Basaltic arc Volcanoes, Eos Trans. AGU, 88(23), Jt. Assem. Suppl., Abstract T32A-04.

Johnson, E.R., Cashman, K., Wallace, P., Delgado Granados, H., 2007. Assessing Magmatic Processes and Hazards at two Basaltic Monogenetic Centers: Volcan Jorullo, Mexico, and Blue Lake Maar, Oregon, Eos Trans. AGU, 88(23), Jt. Assem. Suppl., Abstract V51A-07

Johnson, E.R., Wallace, P., Donegan, C., Delgado Granados, H., 2007. Volatiles in Primitive Magmas Along a Cross-arc Transect in Central Mexico: Implications for Slab Dehydration and Magma Generation Processes, State of the Arc Conference, Chile

Johnson, E., Wallace, P., Cashman, K., Delgado Granados, H., 2006. Evolution of the Plumbing System Beneath a Primitive Cinder Cone: Volcan Jorullo, Mexico, Eos Trans. AGU, 87(52), Fall Meet. Suppl., Abstract V13D-05

Johnson, E.R., Wallace, P.J., Delgado Granados, H., 2005. Magmatic Volatile Variations Along a Trench-Perpendicular Transect in the Central Trans-Mexican Volcanic Belt, Eos Trans. AGU, 86(52), Fall Meet. Suppl., Abstract V41A-1423

Ivany, L.C., Wilkinson, B.C., Lohmann, K.C., Johnson, E.R., McElroy, B.J., Cohen, G.J., 2004. Intra-annual isotopic variation in Venericardia bivalves; implications for early Eocene temperature, seasonality, and salinity on the U.S. Gulf Coast: J. Sed. Res. 74, 7-19.

ACKNOWLEDGMENTS

There are many people that have helped me throughout my PhD. First, I'd like to thank my advisor, Paul Wallace, for inviting me to work on incredible projects in Mexico. Through several field seasons I not only learned about the volcanology and petrology of cinder cone volcanoes, but I had the opportunity to use my rusty Spanish and experience the vibrant culture (and delicious food!) of Mexico. Paul's patience, eagerness to assist his students, and breadth of knowledge in petrology and geochemistry made him an excellent advisor, and someone with whom I hope to collaborate in the future. I'd also like to the Kathy Cashman, a committee member and secondary advisor, who assisted and advised me in the field and encouraged me on a project I developed in the Cascades. Thank you to our collaborator in Mexico, Hugo Delgado Granados, who kindly accompanied us in the field every year. Thank you to the many others who have helped me in the field: Laura Pioli, Mauro Rosi, Nathalie Vigouroux, Elizabeth Erlund, Colleen Donegan, Celeste Mercer, Dan Ruscitto, Isolde Belien, and Reed Burgette.

I need to thank officemates Julie Roberge and Nathalie Vigouroux, who were both wonderful friends and colleagues. I have developed an incredible group of friends here at UO that I am going to miss terribly. I need to thank in particular the "Girl Gang", with whom I shared many a "Ladies Night", clothing swap, bottle of wine, and talk of cats and our futures: Celeste Mercer, Stephanie Weaver, Lisa Emerson, Nathalie Vigouroux, Emily Gottesfeld, Daniele McKay, Kathryn Watts, Laura Stimely, and, of

course, Christine Metzger. Christine and I went through our five years at Oregon together, and I couldn't have done it without her.

I would like to thank my family, who never questioned my switch from Spanish/History to Geology and who supported me all the way through graduate school, although it meant a move to far-off Oregon. I am so incredibly lucky to have such a proud, supportive family! Finally, I would like to thank Reed Burgette for being my incredible partner for the past 4 years. You have helped me so much along the way; I can't even count the times you patiently helped me with a GIS (or Excel) question, the encouragement you've given me, and how many practice talks you've listened too. But more importantly, I appreciate all of the happiness that you gave me, from our incredible Halloween costumes, to planting our first tomato garden, to hiking the trails of Oregon. I am so excited to start the next chapter of our lives together in Tasmania!

To my parents, who have supported me unconditionally in all my endeavors.

TABLE OF CONTENTS

Chapter Page

LIST OF FIGURES

Figure Page

LIST OF TABLES

CHAPTER I

INTRODUCTION

The majority of currently active subaerial volcanoes on Earth are located in arc settings above subduction zones. The aptly named "Ring of Fire", the semi-continuous chain of arc volcanoes rimming the Pacific Ocean, is produced by subduction of oceanic plates beneath the over-riding plates (continental or oceanic). In subduction zones, the downgoing oceanic slab descends beneath the overriding plate, experiencing progressively higher pressure and temperature regimes in the mantle. Due to the increase in pressure and temperature, the subducting plate undergoes a series of metamorphic reactions that change the mineralogy of the slab. At higher pressures and temperatures, hydrous minerals become unstable and eventually break down, releasing H_2O-bearing fluids into the overlying mantle wedge. Introduction of fluids into the mantle wedge lowers the melting temperature of mantle peridotite, producing the partial melts that eventually rise to the surface and create arc volcanoes.

The processes of fluid-fluxing and melt production are complex and are affected by the material being subducted. Subducting oceanic crust is not homogenous worldwide; the age of the crust varies greatly depending on the location of the subduction zone compared to the mid-ocean ridge where the crust forms. Relatively young oceanic crust is hotter than old oceanic crust, and this temperature difference affects the stability of hydrous minerals in the subducting slab. Additionally, the crust can be variably

altered by the flow of hydrothermal fluids at the mid-ocean ridge, and some slabs are extensively hydrated prior to subduction (e.g., Abers et al., 2003). The oceanic crust is overlain by sediments, of variable thickness, that can also be subducted with the oceanic slab. These factors vary in subduction zones around the world, and thus the volcanoes produced in arcs should reflect these variations.

The release of fluids from the slab and their transfer to the mantle wedge is also complex. Until recently, the conventional model for subduction zones suggested that the breakdown of one mineral, amphibole, in the subducted oceanic crust beneath the volcanic arc front was the primary reaction driving the release of fluids into the wedge and producing melting (Tatsumi, 1986). Following this model, volcanoes behind the volcanic arc front should erupt magmas that are more H_2O-poor. However, recent experimental studies of the stability of hydrous minerals in subduction zones have suggested that not only are fluids produced by a series of continuous and discontinuous reactions in the slab (e.g., Schmidt and Poli, 2004), but hydrous minerals in both the oceanic slab and mantle wedge are stable to higher pressures than previously thought (e.g., Schmidt and Poli, 2004; Kerrick and Connolly, 2001; Grove et al., 2006). This suggests that H_2O-rich melt production may occur over a greater range of pressures and temperatures than previously thought.

Due to the involvement of H_2O in producing mantle melting beneath arcs, arc magmas can have high concentrations of H_2O. The high dissolved H_2O concentrations in turn affect the eruption style of arc volcanoes. As these H_2O-rich melts rise to the surface, the pressure decrease allows H_2O and other volatile components to exsolve, resulting in significant degassing of the melts. Recent studies have shown that degassing

can induce crystallization of arc magmas (e.g., Blundy et al., 2006; Johnson et al., 2008: Chapter II). Furthermore, the high volatile contents affect eruption explosivity (e.g., Roggensack et al., 1997; Spilliaert et al., 2006).

In this dissertation I explore the influence of volatiles, particularly H_2O, on the processes of arc volcanism from subduction to melt generation to eruption at the surface. I start by examining the evolution of melt compositions and volatile contents of a subduction-related cinder cone in Mexico that erupted explosively (Chapter II). This study illustrates that melts erupted from basaltic cinder cones in arcs can have high volatile contents, which affect crystallization of the magmas during ascent. From this study of volatile contents in a single cinder cone eruption, I compare and contrast the volatile contents and degassing behavior of cinder cones from across the Michoacán-Guanajuato Volcanic Field (MGVF) of central Mexico with the published data for larger arc volcanoes (Chapter III). Using the analyses from these nine volcanoes in the MGVF, I then investigate across-arc (trench-perpendicular) variations in melt volatile contents and compositions (Chapter IV). The across-arc patterns reflect addition of H_2O-rich components to the mantle wedge and the generation of melts in the mantle. Together with oxygen isotope analyses of olivine phenocrysts and thermal models of the subduction zone in Mexico, I assess the origin of fluid fluxing and melt production beneath the MGVF. The results presented in this dissertation provide a detailed picture of the processes of melt generation and eruption in subduction zone settings.

I am the first author on all chapters in this dissertation, and I was responsible for the bulk of the analyses in each chapter. Chapter II has been published in *Earth and Planetary Science Letters* and is coauthored with my advisor, Paul Wallace, committee

member Kathy Cashman, and scientists Dr. Hugo Delgado Granados (Universidad Nacional Autónoma de Mexico) and Dr. Adam Kent (Oregon State University). All assisted with the editorial process, and Drs. Wallace, Cashman, and Delgado Granados aided with field work. Dr. Adam Kent assisted with LA ICP-MS analyses of samples at Oregon State University. Chapter III is in preparation for submission to the *Journal of Volcanology and Geothermal Research* and is coauthored with advisor Paul Wallace and committee member Kathy Cashman, who assisted with field work and editing of the document. Chapter IV is in preparation for submission to *Geochemistry, Geophysics, Geosystems*, and is coauthored with advisor Paul Wallace and Dr. Ilya Bindeman (UO) and Dr. Vlad Manea (Universidad Nacional Autónoma de Mexico, Juriquila). All collaborators assisted in the editorial process, and Dr. Wallace aided with field work. Oxygen isotopic analyses were performed with the assistance of Dr. Bindeman in his laboratory here at the University of Oregon, and the 2-D thermal models were created by Dr. Manea. Chapter V is a summary of the work discussed in the previous chapters.

CHAPTER II

MAGMATIC VOLATILE CONTENTS AND DEGASSING-INDUCED CRYSTALLIZATION AT VOLCAN JORULLO, MEXICO: IMPLICATIONS FOR MELT EVOLUTION AND THE PLUMBING SYSTEMS OF MONOGENETIC VOLCANOES

This work was published in volume 269 of Earth and Planetary Science Letters in May, 2008. Coauthors Paul Wallace, Kathy Cashman, and Hugo Delgado Granados assisted in the field and Adam Kent assisted with the LA ICP-MS analyses, and all aided in the editorial process. I performed the laboratory work and was the primary author.

1. Introduction

Water is fundamental to magma production in subduction zones by initiating melting of the mantle wedge above the downgoing slab. Furthermore, the presence of water and other volatiles in magma prior to eruption affects crystallization during ascent and eruption explosivity. Melt inclusion analyses have shown that arc magmas can have high H_2O (3.5-8 wt%; Sisson and Layne, 1993; Roggensack et al., 1997; Cervantes and Wallace, 2003; Wade et al., 2006; Spilliaert et al., 2006) that may correlate with high explosivity (Roggensack et al., 1997; Spilliaert et al., 2006). Degassing of these H_2O-rich magmas during ascent may also induce rapid and extensive crystallization (e.g.,

Sisson and Layne, 1993; Métrich et al., 2001; Roggensack, 2001; Atlas et al., 2006; Blundy et al., 2006). However, most studies have focused on persistently active, larger volcanoes, often with evolved melt compositions.

Our research focuses on high-Mg basaltic magmas from a cinder cone eruption. Cinder cones are the most numerous volcanoes on land (Vespermann and Schmincke, 2000), and due to their small volumes and relatively short eruption durations (~1 day to 15 years), the magmas often undergo limited evolution by fractional crystallization and assimilation. In spite of their relative abundance, the hazards posed by cinder cone eruptions are commonly underestimated, and the eruption processes that form cinder cones are not well understood. Most cinder cone eruptions are brief (<1 year; Wood, 1980) and the magmas do not evolve over the course of the eruption. Longer lived eruptions, like Jorullo and Parícutin in Mexico (15 and 9 years, respectively) are more complex; at both volcanoes, magmas evolved progressively during the eruptions, and such evolution has been explained by combinations of fractional crystallization and crustal assimilation (McBirney et al., 1987; Luhr, 2001; Rubin et al., 2004). Recently, fractionation and assimilation in the lower crust in a "deep crustal hot zone" (Annen et al., 2006) or "MASH zone" (Hildreth and Moorbath, 1988) has been invoked to explain intermediate magma compositions erupted from long-lived stratovolcanoes. However, in monogenetic systems, where do fractionation and assimilation occur? A recent study of an eroded cinder cone has shown a network of dikes and sills feeding the volcano just beneath the surface (Valentine and Krogh, 2006). Such a network provides possible shallow magma storage locations where magma could evolve in composition; however,

the development and evolution of such plumbing systems during the course of an eruption are not known.

Here we use melt inclusions trapped in forsterite (Fo) -rich olivine (Fo_{85-91}, where $Fo = 100*Mg/(Mg+Fe^{2+})$), combined with measurements of melt crystallinity and estimates of crystal residence times and magma storage depths, to characterize changes in the plumbing system during the eruption of Jorullo. Our data constrain the undegassed, near-primary volatile contents of the melt and track the degassing, crystallization and compositional evolution of the magma before and during the eruption, thereby providing new insight into cinder cone eruption processes. Our results show that cinder cones, in spite of their relatively small size, are capable of evolving both compositionally and structurally during eruption. In longer-lived eruptions like Jorullo (15 years), the plumbing systems may be more complex than a simple feeder-dike.

2. Geologic setting and eruption history

Jorullo is located in the Michoacán-Guanajuato Volcanic Field (MGVF), in the central part of the subduction-related Trans-Mexican Volcanic Belt (Fig 2.1). Volcanism in the MGVF is due to subduction of the Cocos plate beneath the North American plate off the southwest coast of Mexico. The MGVF contains nearly 1000 cinder cones, many of them Holocene in age (Hasenaka and Carmichael, 1985). Jorullo is located along the volcanic front in the MGVF, roughly 80-90 km above the Cocos plate (Pardo and Suarez, 1995). The most recent activity in the MGVF was the eruption of the cinder cone Parícutin from 1943-1952, 84 km NW of Jorullo.

Jorullo erupted from 1759 until 1774, producing a thick blanket of tephra and ash as well as numerous lava flows (Luhr and Carmichael, 1985). Early accounts indicate that the eruption began violently, with explosive activity that persisted for many years (Gadow, 1930). These accounts, combined with the abundance of fine ash in the tephra blanket, suggest that like Parícutin, Jorullo exhibited violent Strombolian activity, which is characterized by simultaneous explosive eruptions producing large amounts of fine ash and effusion of lava from the base of the cone (Pioli and Cashman, 2006). The widespread lava flows at Jorullo were the focus of an important study by Luhr and Carmichael (1985) that described the eruption and the compositional evolution of the lavas over time. They noted that the earliest lavas were primitive basalt, with 9.3 wt% MgO and phenocrysts of magnesian olivine (Fo_{86-90}), and that as the eruption progressed, the lavas evolved to basaltic andesite compositions (Luhr and Carmichael, 1985).

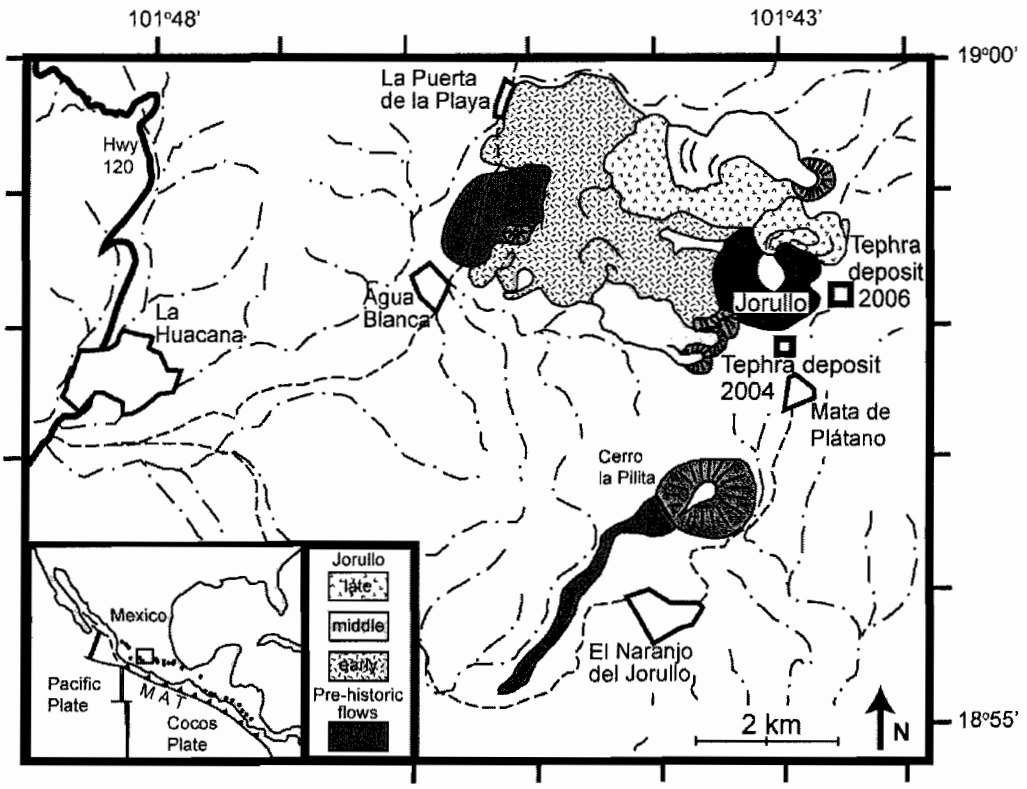

Figure 2.1. Map of Jorullo and surrounding area, modified from Luhr and Carmichael (1985). Squares mark locations of the two tephra sections used in this study; the 2004 section contains the 'Early' (in contact with the paleosol) and 'Middle' samples, and the more complete 2006 section contains the 'Late' sample. Inset shows plate tectonic boundaries associated with the Trans-Mexican Volcanic Belt, with major volcanoes shown as dots.

3. Sample description and analytical procedures

We present results from two sections excavated through the tephra deposit, located ~1 km from the vent to the south and southeast, respectively (Fig. 2.1). The tephra sections expose the earliest erupted explosive material (in contact with the underlying paleosol) and are composed of bedded ash and lapilli layers that provide a time sequence of the eruption. The tephra also contains abundant, loose olivine phenocrysts throughout the section. Samples for this study were chosen from three representative tephra layers - the basal (in contact with the paleosol), middle, and upper

parts of the section - that will be referred to as the 'early', 'middle', and 'late' samples, respectively.

We analyzed olivine-hosted melt inclusions to obtain pre-eruptive volatile and melt compositions. Loose olivine crystals from each of the three layers were separated, cleaned in HBF_4, and examined in immersion oil (refractive index 1.678). Most olivine crystals are euhedral, but subhedral and skeletal crystals are also present. Melt inclusions identified as suitable (those that are fully enclosed by host crystal, are bubble-poor, and appear to be sealed) were prepared as doubly polished wafers and were analyzed for H_2O and CO_2 (FTIR), major elements, S, and Cl (electron microprobe), and trace elements (laser ablation ICP-MS). Melt inclusion compositions were corrected for post-entrapment crystallization of olivine and Fe-loss; corrected values are shown in Table 2.1 and uncorrected values are shown in Supplementary Table 1 (Appendix A) (for details on the correction method and error propagation see Supplementary Material, Appendix B). All data shown in figures and discussed in the text are corrected values. Bulk tephra samples from the three layers were analyzed by XRF at Washington State University for major and trace elements (Supplementary Data Table 2, Appendix C). We also analyzed the compositions of olivine phenocrysts (Table 2.1) and tephra groundmass glass (Supplementary Data Table 3, Appendix D) throughout the tephra stratigraphy. Major elements, S, and Cl were measured with a Cameca SX-100 electron microprobe at the University of Oregon using a 15 kV accelerating voltage, 10 nA beam current, and a beam diameter of 10 μm. A combination of glass and mineral standards was used. Trace element concentrations in the melt inclusions were measured by laser ablation ICP-MS at

Oregon State University (Supplementary Data Table 4, Appendix E). Details of the technique are found in Kent et al. (2004).

Water and CO_2 concentrations in melt inclusions were analyzed by Fourier Transform Infrared Spectroscopy (FTIR) at the University of Oregon. Concentrations of H_2O and CO_2 were calculated using Beer's law: $c = MA/\rho d\varepsilon$, where M is the molecular weight of H_2O or CO_2, A is the measured absorbance of the band of interest, ρ is the room temperature density of basaltic glass, d is the thickness of the melt inclusion and ε is the molar absorption coefficient. In most samples, water concentrations were calculated using the total OH peak at 3550 cm^{-1} and an absorption coefficient of 63 ± 3 L/mol-cm (P. Dobson et al., unpublished data, cited by Dixon et al., 1995). In some instances, however, total H_2O was calculated using an average of the molecular H_2O peaks at 1630 cm^{-1} and 5200 cm^{-1} and the OH^- peak at 4500 cm^{-1}. In these cases absorption coefficients were calculated based on major element compositions (Dixon et al., 1995) and are as follows: 1630 cm^{-1} = 26.4 L/mol-cm, 5200 cm^{-1} = 0.66 L/mol-cm, 4500 cm^{-1} = 0.56 L/mol-cm. CO_2 was calculated using the carbonate peaks at 1515 and 1435 cm^{-1}; an absorption coefficient of 296 L/mol-cm was calculated following Dixon and Pan (1995). Based on uncertainties in thickness measurements and absorbance values, average 1 standard deviation uncertainty in H_2O is ± 0.2 wt% and in CO_2 ± 80 ppm. The background subtraction procedure that we used for the carbonate peaks is described in Roberge et al. (2005).

Table 2.1. Corrected melt inclusion major and volatile element concentrations, host olivine compositions, and inclusion entrapment pressures

Group	Early	Early	Early	Early	Early	Early	Early	Early	Early	Early	Early	Early	Early	Early	Early	Early
Inclusion	1	12_1	12_2	12_3	13_1	13_2	14	17_1	17_2	17_A	20	23	24	28	29_1	29_3
SiO_2	51.15	51.54	52.06	51.58	50.60	50.11	50.93	52.90	51.32	51.19	51.22	50.63	49.89	51.57	51.01	50.26
TiO_2	0.79	0.68	0.63	0.75	0.88	0.75	0.67	0.74	0.80	0.74	0.88	0.75	0.73	0.65	0.76	0.71
Al_2O_3	15.66	16.77	17.25	16.96	18.90	19.46	17.15	16.44	17.21	17.46	16.74	17.15	17.87	16.63	17.69	17.55
FeO^T	7.84	7.38	7.30	7.36	7.65	7.26	7.46	7.47	7.52	7.41	7.55	7.56	7.62	7.48	7.65	7.57
MnO	0.15	0.13	0.06	0.08	0.08	0.21	0.02	0.10	0.10	0.04	0.15	0.07	0.05	0.10	0.14	0.09
MgO	10.51	9.23	9.00	9.44	7.75	7.43	9.99	9.29	9.64	9.25	9.91	10.03	10.46	9.82	8.69	9.56
CaO	9.20	9.34	8.57	8.91	8.92	9.21	9.01	8.28	8.55	8.93	9.14	8.96	8.60	8.55	8.92	9.21
Na_2O	3.74	4.13	4.20	4.04	4.26	4.59	3.89	4.01	4.04	4.17	3.60	4.00	3.92	4.25	4.21	4.21
K_2O	0.77	0.65	0.77	0.73	0.81	0.83	0.70	0.65	0.67	0.68	0.61	0.66	0.72	0.84	0.77	0.66
P_2O_5	0.18	0.15	0.16	0.15	0.16	0.16	0.17	0.13	0.15	0.14	0.19	0.19	0.14	0.12	0.16	0.16
H_2O	0.9	4.7	2.5	4.2	3.4	n.a.	1.2	5.4	2.6	n.a.	1.5	3.8	2.2	1.0	2.9	3.4
CO_2 ppm	118	243	207	915	-	n.a.	307	805	692	n.a.	594	988	-	-	358	556
S ppm	1149	1195	1379	1751	1591	1560	1718	1751	1665	2066	1847	1882	1776	688	1737	1644
Cl ppm	1103	1179	1197	1239	1285	1406	1381	1239	1308	1286	1267	1196	1185	1105	1176	1206
Total *	99.17	97.05	97.18	96.28	97.07	98.22	97.50	96.18	96.14	95.42	95.34	94.10	95.88	96.99	96.36	96.72
P (bars)	343	2542	1064	3445	1152	n.a.	808	4027	2080	n.a.	1481	3444	515	101	1668	2309
Olivine (Fo%)	91.1	90.3	89.9	90.4	88.4	88.4	90.5	90.1	90.3	90.1	90.5	90.7	90.6	90.0	89.3	90.2
%PEC **	14.2	6.9	12.4	10.6	3.5	4.4	17.9	9.1	12.5	9.7	11.6	10	20.6	18	8.5	11

Group	Middle	Middle	Middle	Middle	Middle	Late	Late	Late	Late	Late	Late	Late	Late
Inclusion	4	5	6	7_1	10	1	3_1	3_2	4	5	p1	p2	p3a
SiO_2	52.92	52.99	50.15	50.24	51.70	51.34	52.54	55.21	53.66	51.95	50.66	54.13	55.14
TiO_2	0.76	0.88	0.90	0.89	0.76	0.98	0.95	1.12	0.88	0.84	1.06	0.98	0.91
Al_2O_3	17.42	18.09	20.14	19.69	20.32	19.83	19.07	18.02	18.01	20.42	20.25	18.59	17.87
FeO^T	7.48	6.75	6.79	7.07	6.92	6.76	7.07	6.69	7.47	6.68	6.89	6.73	6.76
MnO	0.12	0.11	0.10	0.12	0.07	0.08	0.15	0.03	0.06	0.10	0.08	0.06	0.04
MgO	7.26	6.53	5.97	6.93	6.80	6.06	5.83	5.53	5.91	5.15	6.15	6.05	6.06
CaO	9.05	8.87	10.61	9.70	7.28	9.71	8.96	8.29	8.13	9.55	9.50	8.26	8.72
Na_2O	4.02	4.45	4.32	4.30	5.06	4.29	4.34	4.07	4.66	4.24	4.50	4.28	3.72
K_2O	0.82	1.15	0.83	0.84	0.93	0.74	0.85	0.85	1.02	0.83	0.72	0.75	0.60
P_2O_5	0.15	0.17	0.20	0.21	0.17	0.22	0.23	0.20	0.20	0.24	0.19	0.17	0.17
H_2O	1.4	0.5	1.1	1.1	0.8	0.5	0.8	0.8	0.8	1.0	n.a.	n.a.	n.a.
CO_2 ppm	-	-	-	-	-	-	-	-	-	-	n.a.	n.a.	n.a.
S ppm	1407	1299	2040	1786	1781	1442	1143	74	918	1490	2106	1477	1479
Cl ppm	910	1247	1094	1127	1419	1239	1162	1020	994	1065	1298	1206	936
Total *	99.47	102.86	97.24	99.93	100.11	100.10	100.01	99.25	99.39	98.51	100.02	100.00	99.96
P (bars)	186	24	115	121	62	26	64	65	68	87	n.a.	n.a.	n.a.
Olivine (Fo%)	88.2	88.0	86.6	88.4	87.3	86.7	85.6	85.6	84.9	85.0	86.7	86.2	86.8
%PEC **	4.8	6.7	2.0	3.8	11.2	4.5	5.9	6.4	8.1	1.6	4.1	11.8	2.3

Table 2.1. Total * = sum of all oxides plus S and Cl in original (uncorrected) microprobe analyses, %PEC** = wt% post-entrapment crystallization. All melt inclusion data were corrected for post-entrapment crystallization (%PEC) of olivine (Sobolev and Chaussidon, 1996) and diffusive loss of Fe (Danyushevsky et al., 2000; see Supplementary Material). Major element oxides reported are normalized to 100% on a volatile-free basis. The average standard deviation (absolute) based on multiple (2-4 points) analyses is as follows: SiO_2: 0.27, Al_2O_3: 0.20, FeO: 0.16, MgO: 0.22, CaO: 0.36, Na_2O: 0.27, K_2O: 0.03, TiO_2: 0.10, MnO: 0.05, P_2O_5: 0.03, S: 90, Cl: 60.

We measured compositional profiles across zoned olivine crystals by electron microprobe. We calculated residence times for the olivine crystals predicated on the assumption that the zoning was produced by a magma mixing event (discussed in section 5.5), and followed the methods of Costa and Chakraborty (2004). We used the simple, 1-D diffusion equation:

$$C = C_1 + (C_o - C_1)*\mathrm{erf}\,[x/(2(\sqrt{D*t})] \quad (1)$$

where C is the concentration, x is distance, D is the diffusion coefficient, and t is time. We calculated diffusion coefficients, D, for Fe-Mg exchange using the equation from Jurewicz and Watson (1988):

$$D_{Fe\text{-}Mg} = 8 \times 10^{-7} * \exp(-29708/T)\ m^2 s^{-1} \quad (2)$$

where D is diffusion parallel to the c-axis, and we assumed that $D_a = D_b = 6D_c$ (Dohmen et al., 2003). Using equation (1) we fit a modeled diffusion profile to our data, and calculated the time required to produce that profile. Our calculations were based on compositional profiles along the a- and b-axes of olivine crystals, and we used eruption temperatures calculated using the method of Sugawara (2000), which generally agree with eruption temperatures calculated using MELTS and pMELTS (Ghiorso and Sack, 1995; Asimow and Ghiorso, 1998; Ghiorso et al., 2002).

To track changes in crystallinity of the melts throughout the eruption we took images of the groundmass from the three representative tephra layers. Images were collected using an FEI Quanta scanning electron microscope (SEM) at the University of Oregon. These images were then analyzed using SCION image analysis software to calculate the groundmass crystallinity and the size (crystal area) of groundmass microlites for each sample.

4. Results

4.1. Melt inclusion and groundmass compositions

Jorullo lavas evolved from initially primitive basalt to basaltic andesite over the course of the ~15 year eruption (Luhr and Carmichael, 1985). Our corrected melt inclusion compositions show a similar evolutionary pattern (Table 2.1), though there are some important compositional differences between melt inclusions and lavas. The early melt inclusions have high MgO (7.5-10.5 wt%) and low K_2O (0.6-0.8 wt%), suggesting that early olivine crystals trapped primitive melts that had undergone little to no differentiation from a parental magma (Fig. 2.2). The later-erupted melt inclusions sampled progressively more evolved melt compositions, with decreasing MgO (5-7.4 wt%) and increasing K_2O (0.8-1.1 wt%). Groundmass glasses have low MgO (3.7-4.3 wt%) and higher K_2O (1.3-1.6 wt%), indicating that extensive crystallization occurred after melt inclusion entrapment. Importantly, the lavas show increases in K_2O and decreases in CaO with decreasing MgO that differ from many of the melt inclusions. These deviations imply differences in magmatic processes for lavas and melt inclusions, and the significance of this will be discussed in section 5.3.

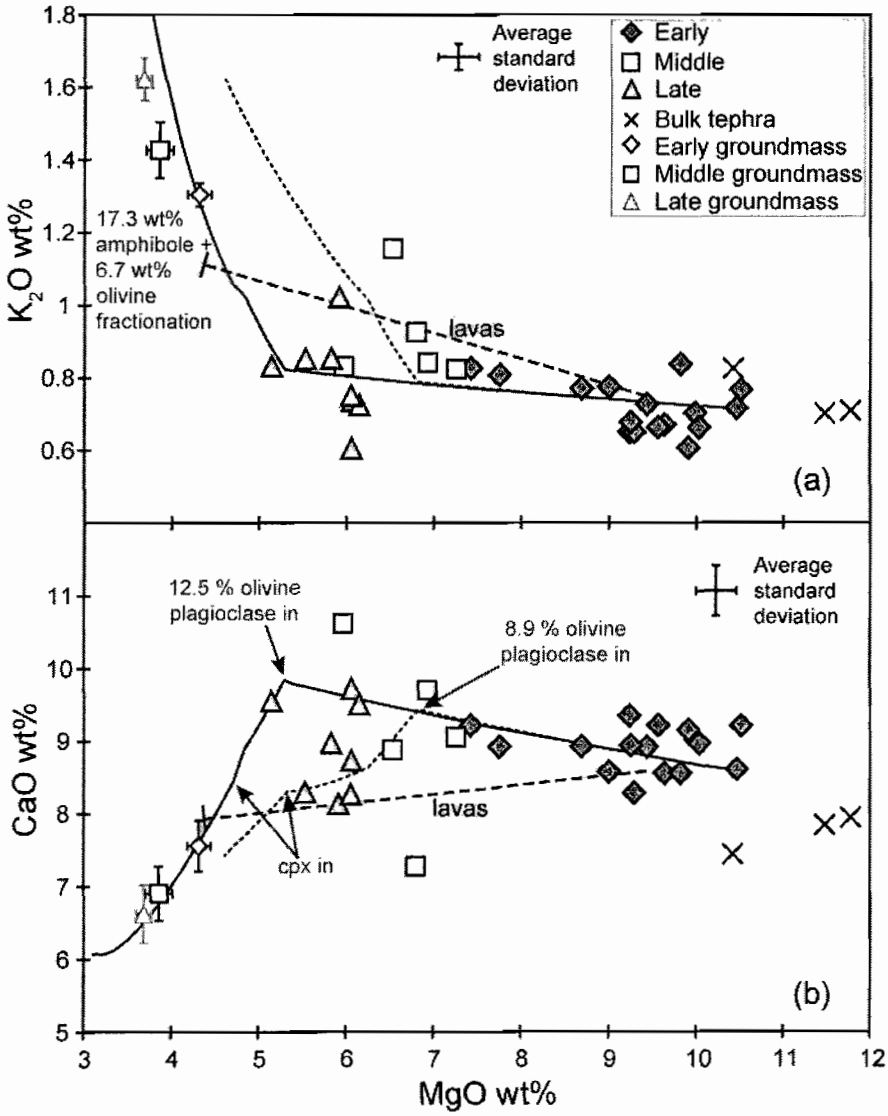

Figure 2.2. Major elements vs. MgO for Jorullo melt inclusions, tephra groundmass glass, bulk tephra, and lava whole-rock samples (lava analyses are from Luhr and Carmichael, 1985). In both figures, MELTS calculations (see Fig. 2.8) indicate that olivine-only crystallization explains much of the range in MgO, K_2O, and CaO whereas some inclusions record plagioclase ± clinopyroxene crystallization. The MELTS calculations simulate a probable ascent path (varying both pressure and temperature), and the solid line shows an ascent path with greater cooling than the path of the dotted line. In contrast, the bulk melt evolution, as shown by the lava trend, corresponds to fractionation of 17.3 wt% amphibole + 6.7 wt% olivine (thick dashed line), based on major element modeling. Also shown are the average standard deviations based on multiple analyses per sample.

Melt inclusion incompatible trace element concentrations also generally increase from the early to late stages of the eruption (Fig. 2.3). While some elements show steady increases from early to late in the eruption, several elements seem to be anomalously enriched in the late melt inclusions. Similar enrichments were seen in some trace elements in the late-stage lavas (Luhr and Carmichael, 1985).

The bulk tephra analyses from the early, middle and late tephra layers are all less evolved than the earliest lavas (Fig. 2.2), suggesting that the preserved tephra sequence that we sampled may have been erupted prior to most, if not all, of the lava flows. This interpretation is supported by descriptions of the eruption that suggest that the early phases of activity were mainly explosive and that lava flows may not have issued from the cone until the eruption was in its fifth year (Gadow, 1930). An alternative possibility is that the proximal tephra deposits that we sampled were enriched in dense olivine relative to the lower density, vesicular pyroclasts ejected during eruption and fallout of the tephra.

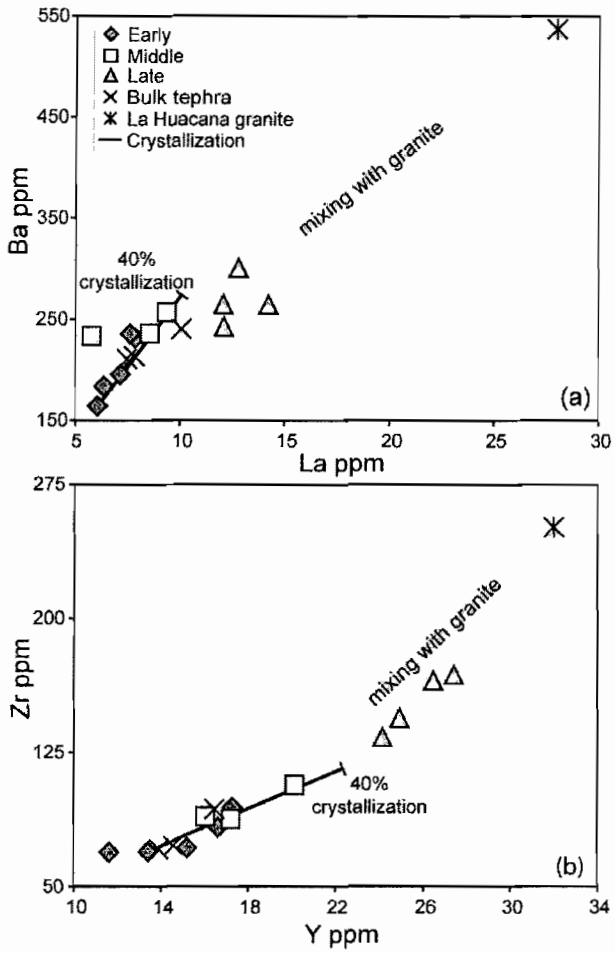

Figure 2.3. Trace element analyses for melt inclusions (laser ablation ICP-MS) and bulk tephra (ICP-MS). Figure 2.3a shows Ba vs La and Figure 2.3b shows Zr vs Y. Both figures show a solid line representing 40% fractionation (an upper limit of crystallization, as suggested by Fig. 2.9) and an analysis of the La Huacana granite bedrock (Luhr and Carmichael, 1985). Light gray bands indicate mixing between the Jorullo melts and the granite, suggesting a role for assimilation in the later melts.

4.2. Olivine compositions and zoning

Comparison of olivine compositions in the tephra and lava supports our interpretation that the explosive eruptions largely preceded effusive activity, and shows that the olivine forsterite content decreased throughout the eruption. Figure 2.4 shows probability density curves for olivine core compositions from the lava flows (Luhr and Carmichael, 1985) and the tephra throughout the eruption. Olivine from the early and

middle tephra are overall more forsterite-rich than olivine from the early and middle lava flows, suggested they were erupted prior to effusion of the lavas. The olivine cores exhibit an increasing compositional range from the early tephra (Fo_{88-91}) to the late tephra (Fo_{83-88}) to the latest lava flows (Fo_{73-87}).

Olivine crystals from both the tephra and lava flows are normally zoned (Fig. 2.5). Zoned rims range from abrupt in the early tephra (Fig. 2.5a) to more gradual in the late tephra (Fig. 2.5b), suggesting that crystals may have resided in more evolved magmas for varying lengths of time. Using transects across these zoned crystals and the equations described earlier, we have modeled the zoning profiles (solid lines, Figs. 2.5a, b) and the corresponding residence times for olivine from the early, middle and late stages of the eruption. We calculate a range of olivine residence times, from ~10-200 days for the early-erupted olivine to ~80-1300 days for the late-erupted olivine (Fig. 2.5c). Implications for these residence times are discussed in section 5.5.

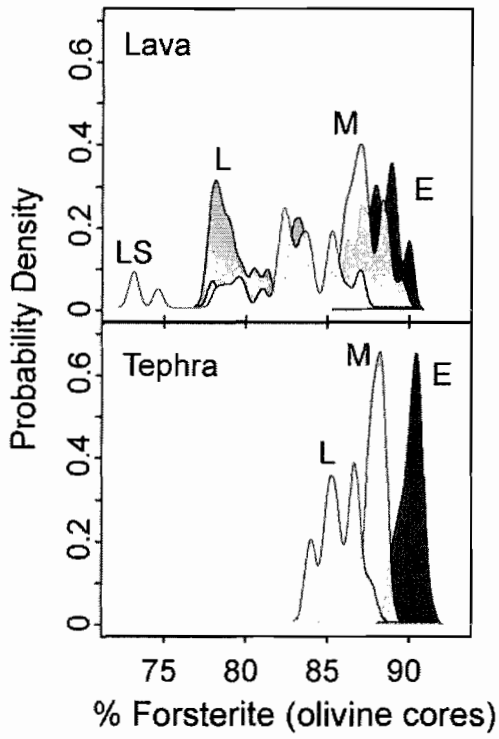

Figure 2.4. Probability density curves for olivine core compositions from tephra (lower) and lava (upper; Luhr and Carmichael, 1985), where E = Early, M = Middle, L = Late (for olivine from both tephra and lava), and LS = latest (lava). These plots illustrate the general decrease in olivine core Fo content throughout the eruption. Early and middle tephra samples appear to correspond to an earlier phase of the eruption based on high olivine Fo content, the narrow range of olivine compositions, and the primitive composition of bulk tephra. Observations of the eruption that describe explosive activity only during the first few years of the eruption (Gadow, 1930) and a thinning of tephra onto the earliest lava flows support this interpretation. The early phase of erupted lava appears to correlate roughly with our middle tephra.

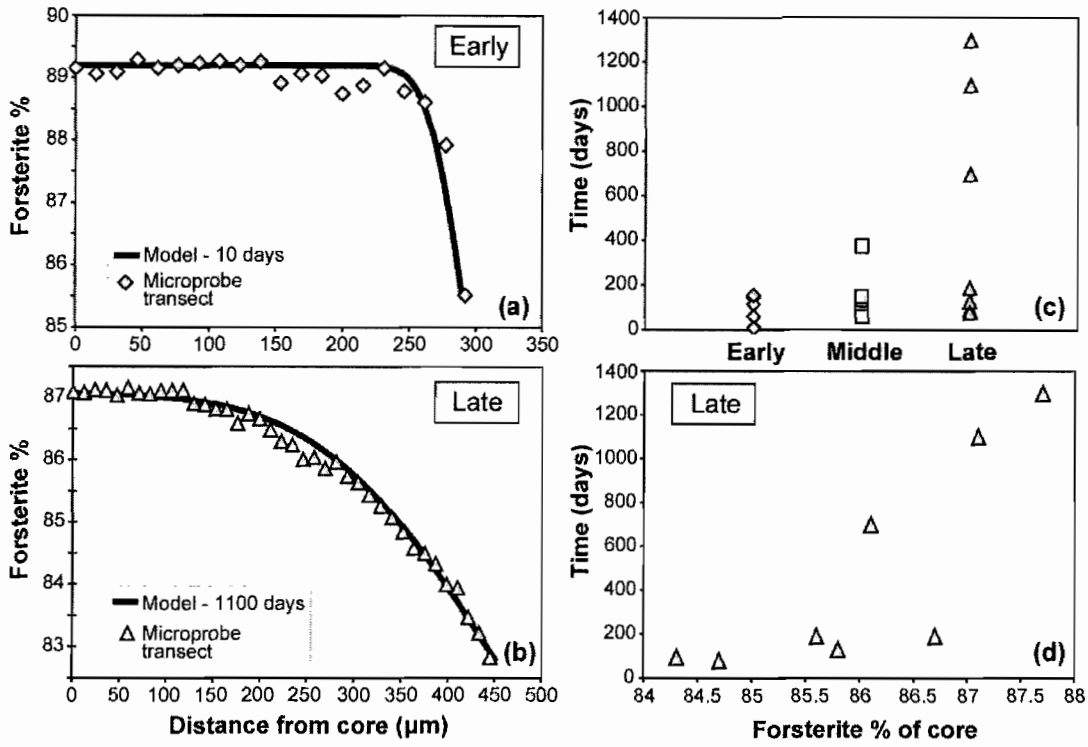

Figure 2.5. Olivine zoning and residence time calculations. Figs. 2.5a and 2.5b show representative electron microprobe transects from core-to-rim for early and late olivine crystals, respectively. Also shown are modeled diffusion profiles (thick solid lines). Fig. 2.5c shows the calculated residence times for olivine from the early, middle and late stages of the tephra section. Fig. 2.5d illustrates the positive relationship between olivine residence time and olivine core composition from the late olivine samples. This suggests that earlier, less evolved melts crystallized olivine that then resided for potentially long periods of time in more evolved melts. Standard deviations were calculated based on multiple transects and models, but error bars are smaller than the symbol size.

4.3. Melt inclusion volatile concentrations

Melt inclusions preserved in Jorullo olivine trap some of the highest volatile contents yet recorded in primitive arc magmas and suggest a complex and evolving degassing history throughout the eruption (Fig. 2.6). Inclusions in early erupted olivine record a wide range of volatile contents and trapped both relatively undegassed melts, with up to 5.3 wt% H_2O and 1000 ppm CO_2, and degassed melts, with low H_2O and CO_2 below detection (< 50 ppm). This diversity in H_2O and CO_2 concentrations indicates that

olivine crystallized over a wide range of depths, corresponding to entrapment pressures of 10 to ~ 400 MPa. The later-erupted inclusions are much more uniform in volatile concentrations, with all melt inclusions recording CO_2 below detection and consistently low H_2O (0.2-1.4 wt% in middle samples; 0.4-1.0 wt% in late samples) that indicate olivine crystallization only at very low pressures (< 20 MPa). In contrast, melt inclusion S and Cl contents do not vary significantly during the eruption (S mostly 1200-1800 ppm; Cl 1000-1400 ppm, Table 2.1) and do not correlate with H_2O.

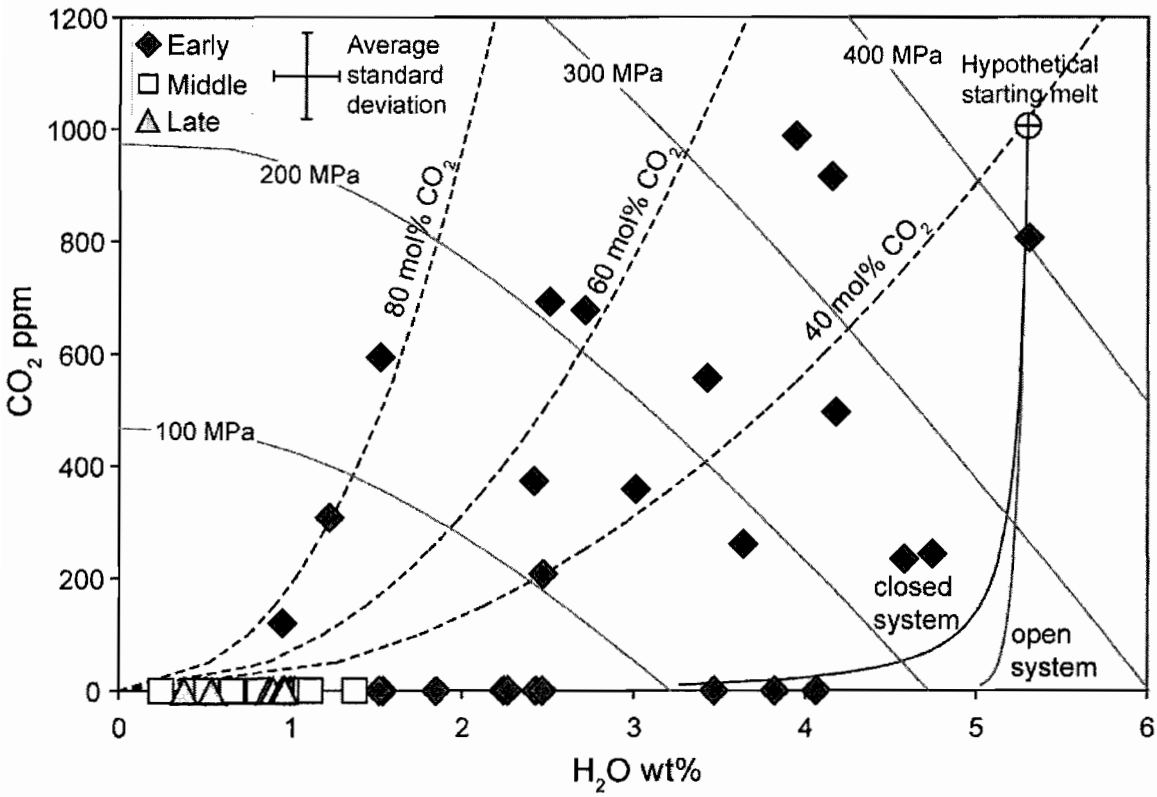

Figure 2.6. Melt inclusion CO_2 vs. H_2O for early (diamonds), middle (squares), and late (triangles) samples. Also shown are calculated vapor saturation isobars, open and closed system degassing paths, and vapor isopleths for 40, 60 and 80% CO_2, all calculated using VolatileCalc (Newman and Lowenstern, 2002). For many inclusions, the pressures based on dissolved H_2O and CO_2 are minimum values because the inclusions contain a small shrinkage vapor bubble (formed post-entrapment) that contains some additional CO_2. However, most low H_2O, low CO_2 inclusions contain no such shrinkage bubble. The average standard deviation was calculated based on multiple analyses per inclusion.

4.4. Groundmass crystallinity

The tephra groundmass contains abundant microlites of plagioclase, as well as minor olivine and clinopyroxene (Figs. 2.7a, b). Measurements of microlite abundance in the groundmass from the three tephra layers show a slight increase in crystallinity from early (41 ± 1%, average ± 1 s.e.) to late (47 ± 2%) in the eruption (Fig. 2.7c). Additionally, there are notable increases in microlite size (area), as seen visually in the comparison of the early groundmass (Fig. 2.7a) and late groundmass (Fig. 2.7b). The average size of olivine and clinopyroxene crystals increases from 60 ± 13 μm^2 (early) to 145 ± 13 μm^2 (late), and the average size of plagioclase laths increases from 124 ± 7 μm^2 (early) to 180 ± 20 μm^2 (late) (Fig. 2.7d).

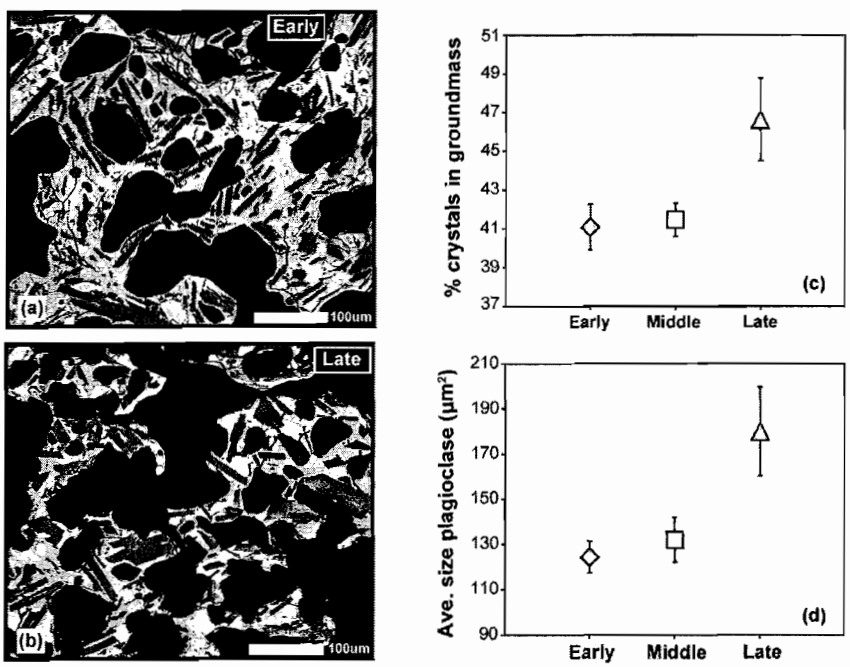

Figure 2.7. Groundmass crystallinity from SEM image analyses. Figs. 2.7a and 2.7b show images of groundmass tephra from the early and late tephra samples, respectively. Fig. 2.7c shows the average crystallinity for early, middle and late samples based on SCION image analysis estimates. Fig. 2.7d shows an increase in size of groundmass plagioclase from early to late in the eruption, where size is the area of a groundmass crystal as calculated using SCION image analysis software. Error bars show ± 1 standard error based on analysis of multiple images for each sample.

5. Discussion

5.1. Degassing processes

The scatter in the melt inclusion H_2O and CO_2 concentrations shown in Figure 2.6 reflects a complex magma degassing history. Calculated degassing paths (solid lines, Fig. 2.6) show that some of the variation in H_2O and CO_2 can be explained by either open-system degassing, where CO_2 degasses almost entirely with little loss of H_2O, or closed-system degassing, in which the ascending melt and exsolving gas remain in equilibrium. However, many inclusions have elevated CO_2 for a given H_2O content that cannot be explained by closed-system degassing models. Similar scatter has been seen in other magmatic systems (e.g., Rust et al., 2004; Atlas et al., 2006; Spilliaert et al., 2006). The low H_2O, high CO_2 inclusions could result from several processes, including disequilibrium degassing of melts before entrapment (Gonnermann and Manga, 2005) or post-entrapment diffusive loss of H_2 or H_2O through the melt inclusion host crystals. The former process is difficult to evaluate because of the lack of data on H_2O and CO_2 diffusivities in hydrous basaltic melts (Baker et al., 2005), but it is probably more effective in low temperature, silicic magmas. Loss of water by H_2 diffusion is probably limited to ≤ 1 wt% H_2O by redox effects (Danyushevsky et al., 2002), and thus could not explain all of the scatter we see in our data. Loss of water by molecular H_2O diffusion through the olivine host (Portnyagin and Almeev, 2007) is not limited by redox reactions. However, the loss of 2.5 to 4 wt. % H_2O that would be required to account for our data (assuming all high CO_2 inclusions started along the closed-system degassing curve in Fig. 2.6) would cause considerable crystallization of olivine, plagioclase, and clinopyroxene inside the inclusions and formation of a substantial shrinkage vapor bubble. None of

these features are observed in the high CO_2, low H_2O inclusions, leading us to conclude that significant H_2O diffusive loss through the host olivine has not occurred. Additionally, we see no correlation between diffusive Fe-loss from the melt inclusions (see Supplementary Material) and the deviation of H_2O contents from the closed system degassing curve in Figure 2.6.

An alternative possibility is that the scatter in Figure 2.6 may be the result of melts equilibrating with more CO_2-rich vapor percolating through the system from below, where it is released by magma degassing deeper in the system (Rust et al., 2004; Spilliaert et al., 2006). Vapors with 40-80 mol% CO_2 fit most of the scatter in our data (CO_2 vapor isopleths, dashed lines, Fig. 2.6). This gas fluxing hypothesis requires that melts have initially high CO_2 contents ($\geq$ 0.7 wt%) in order to create such CO_2-rich gases during ascent in the deep crust. Although such high values have not been found in melt inclusions, an analysis based on arc volcanic CO_2 fluxes suggests that such high values are common in mafic arc magmas (Wallace, 2005). The gas fluxing effect may be enhanced by repeated cycles of decompression and repressurization within the conduit (Rust et al., 2007).

The melt inclusions record evidence for loss of H_2O and CO_2 by degassing, but there is no indication of S and Cl degassing throughout the eruption, probably because these components have higher solubility. Lack of Cl degassing has been observed previously (e.g., Sisson and Layne, 1993), but the lack of S degassing is more peculiar and may result from relatively high oxygen fugacity and presence of S primarily as sulfate.

5.2 Crystallization during ascent and degassing

The primitive composition of the early Jorullo melts combined with initially high magmatic volatiles, gas fluxing, and degassing caused olivine-only crystallization over the wide range of depths indicated by our melt inclusion data. These inferences are supported by a phase diagram for early Jorullo melts constructed using MELTS and pMELTS (Fig. 2.8). The high MgO and H_2O contents of the early Jorullo melts produce a large field of olivine-only crystallization. Melt inclusion data demonstrate that olivine crystals formed at a maximum pressure of 400 MPa; however, at this pressure the melts are H_2O-undersaturated. Deep crystallization would have been facilitated by CO_2-rich vapor fluxing through the system, as suggested by some of the melt inclusion data (Fig. 2.6). Fluxing of CO_2-rich gas would remove H_2O from the melt, even though the melts were H_2O undersaturated. Thus the melts would have been below their relevant H_2O undersaturated liquidii (Fig. 2.8), forcing small quantities of olivine to crystallize during ascent. Larger amounts of olivine would have crystallized once the melts crossed the H_2O saturated liquidus (at ~150-200 MPa).

The phase relations (Fig. 2.8) are also consistent with the complicated degassing history shown in the plot of CO_2 vs. H_2O (Fig. 2.6). In this plot there are essentially two groups of inclusions; the first group are those that roughly fit either open or closed system degassing paths, in other words, melts that have degassed all of their CO_2 prior to olivine crystallization. These crystals would have grown along or below the H_2O-saturated olivine-in curve at pressures commencing at ~150 MPa, as recorded by the entrapment pressure of the CO_2-poor melt inclusion with the highest H_2O (Fig. 2.6). The second group of inclusions are those that cannot be explained by either closed or open

system degassing, and instead require fluxing of CO_2-rich vapor through the system. According to our melt inclusion data, nearly all inclusions trapped at pressures >200 MPa require interaction with CO_2-rich vapor; these pressures correspond to the region above the H_2O-saturated olivine-in curve where the ability to crystallize olivine depends on addition of CO_2 and subsequent loss of H_2O from the melt.

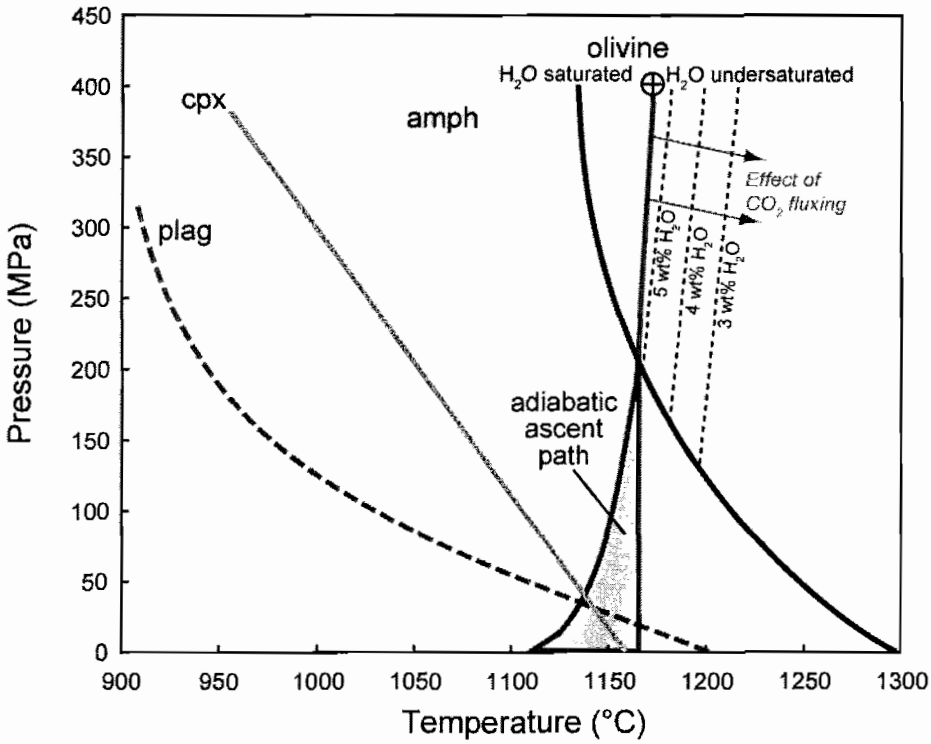

Figure 2.8. Phase diagram for early Jorullo melt composition (10.5 wt% MgO) constructed using MELTS (Ghiorso and Sack, 1995; Asimow and Ghiorso, 1998) and pMELTS (Ghiorso et al., 2002). Circle with cross indicates hypothetical starting melt based on the highest melt inclusion entrapment pressure of 400 MPa with 5.3 wt% H_2O. The adiabatic ascent path was calculated using MELTS and pMELTS and includes the effects of crystallization, gas exsolution, and gas expansion; the widening at low pressures reflects variability between the two models. Amphibole liquidus region is based on experimental studies by Holloway (1973), Holloway and Ford (1975), Moore and Carmichael (1998), Grove et al., (2003), and Nicholis and Rutherford (2004).

The adiabatic ascent path in Figure 2.8 shows that olivine would be the only crystallizing phase over a large range of pressures (~400-30 MPa), with plagioclase joining olivine only at low pressures (< 30 MPa), followed by near-surface crystallization of clinopyroxene. This predicted ascent and crystallization path agrees with the melt inclusion data, the modal abundance of olivine in the tephra, and the presence of late stage plagioclase and minor clinopyroxene as groundmass crystals in the quenched tephra glass (Figs. 2.7a, b).

The later-erupted melt inclusions indicate that crystallization moved to shallow levels as the eruption progressed. The lower MgO content of the later melts would have decreased the olivine-only field, such that olivine could only have crystallized at pressures $\leq$ 100 MPa (based on an eruption temperature of ~1150° C and the phase diagram of Moore and Carmichael, 1998). However, melt inclusion entrapment pressures later in the eruption vary only from 3-19 MPa, suggesting that either deeper crystallizing olivine fractionated out of the melt and was not erupted, or, that olivine preferentially crystallized only shallowly in the plumbing system. This shallow crystallization further suggests that the CO_2 fluxing that enabled deep olivine crystallization early had shut off later in the eruption. Additionally, some later-erupted melt inclusions show the compositional effects of plagioclase +/- clinopyroxene crystallization (see section 5.3). These phases would also have crystallized at low pressures (< 40 MPa), lending further support to the development of a shallow region of melt crystallization.

Our data show that the crystallization recorded by melt inclusions is driven by H_2O loss during ascent. At higher pressures (200-400 MPa) loss of H_2O is likely caused by gas fluxing, but at lower pressures, CO_2-depleted melts lose H_2O by direct exsolution

of H_2O-rich vapor. Both processes cause melts to degas H_2O and thus can result in crystallization. Variations in K_2O, which is incompatible during crystallization, are consistent with a model of degassing-induced crystallization (Fig. 2.9). Based on the K_2O content of the highest pressure inclusion (0.66 wt% K_2O), increases in K_2O with decreasing pressure for all early erupted melt inclusions are consistent with up to 14% crystallization. Later in the eruption, low pressure degassing resulted in extensive shallow crystallization of olivine, plagioclase, and minor clinopyroxene, producing K_2O increases that require up to 29-36% crystallization prior to melt inclusion entrapment (Fig. 2.9).

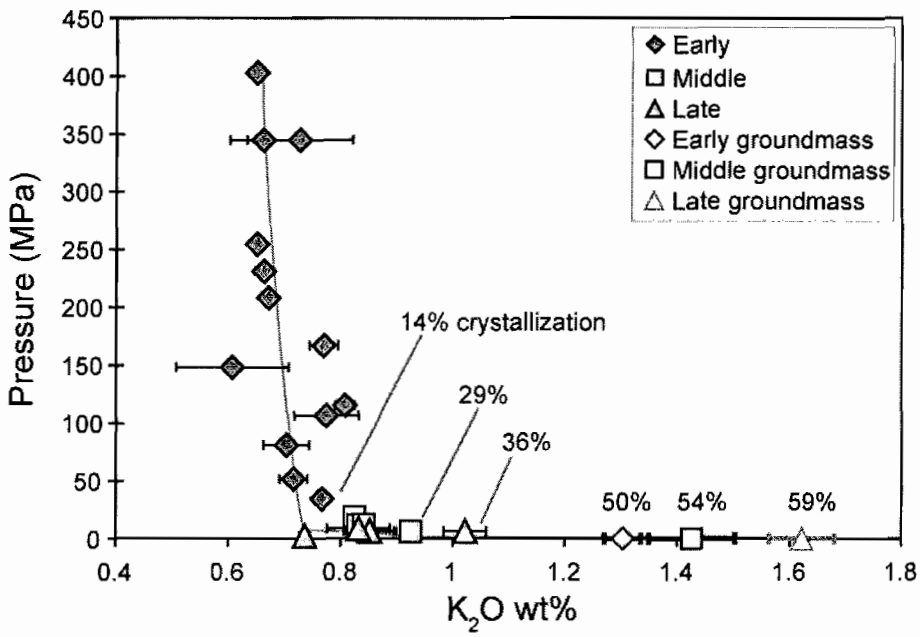

Figure 2.9. Pressure (MPa) vs. K_2O for melt inclusions and groundmass glasses. Pressures for melt inclusions were calculated based on dissolved CO_2 and H_2O (Fig. 2.6) using the VolatileCalc solubility model (Newman and Lowenstern, 2002). Percent total crystallization required to relate various compositions to the parental melt is calculated assuming that K_2O is perfectly incompatible. Also shown is the calculated MELTS ascent path, which predicts 48% total crystallization and agrees well with the data (gray curve). Error bars show ± 1 standard deviation based on multiple analyses. Where not shown, error is smaller than symbol size.

Whereas the late inclusions were trapped shallowly (3-19 MPa), crystallization of the groundmass in the tephra clasts occurred shallower still, likely during rise in the upper conduit and during eruption. Groundmass glass analyses for the three tephra layers indicate that significant crystallization of microlites occurred after the melt inclusions were trapped (Fig. 2.9). The K_2O in tephra groundmass glass increases steadily from the early (1.3 wt%) to late (1.6 wt%) samples, corresponding to approximately 50% total crystallization (early) and 59% total crystallization (late) of initially primitive melt. These values suggest that ~25% crystallization occurred between the last melt inclusion trapped and eruption and quenching of the pyroclasts, and that much of this extensive crystallization was shallow (< 10 MPa).

Additionally, the temporal increase in both crystallinity and crystal size measured in groundmass glass images (Figs. 2.7c, 2.7d) suggests an increased time scale for groundmass crystallization prior to eruption. This could have been achieved by either decreasing ascent rate in the latter stages of the eruption or storage of later melts en route to the surface. Shallow storage of magma at the base of a growing cinder cone has been suggested elsewhere (Krauskopf, 1948; Cervantes and Wallace, 2003; Pioli and Cashman, 2006) to explain both lava effusion from the base of cinder cones and shallow growth of olivine crystals.

5.3. Lava vs. tephra -- the role of deep crustal fractionation

The melt compositions trapped in olivine during the eruption of Volcán Jorullo record the importance of olivine crystallization throughout the eruption, with the addition of shallow plagioclase +/- clinopyroxene crystallization later in the eruption. Olivine

crystallization played a key role in changing the liquid composition, as evidenced by the abundance of olivine in the tephra and lava flows and the decrease in melt inclusion MgO contents as the eruption progressed (Fig. 2.2). Much of the melt inclusion data can be explained by ~ 13 wt% olivine fractionation (solid line in Fig. 2.2). However, lower CaO contents in some of the later inclusions and the groundmass glass require additional crystallization of plagioclase +/- clinopyroxene (solid and dotted lines, Fig. 2.2b).

Whereas the melt inclusion data record crystallization of olivine ± plagioclase ± clinopyroxene in the upper crust caused by ascent and degassing, the bulk lava compositions (gray field, Fig. 2.2) differ from the melt inclusions, suggesting a different fractionation history. Unlike the melt inclusions, the lavas gradually increase in K_2O and decrease in CaO with decreasing MgO beginning early in the eruption. As no combination of the main erupted phenocrysts (olivine ± plagioclase) can generate this trend, Luhr and Carmichael (1985) explained this evolution by high pressure fractionation of clinopyroxene, olivine, and plagioclase. However, they noted that this explanation was problematic because of the absence of clinopyroxene phenocrysts in most lavas, and abundances of a number of incompatible trace elements were not satisfactorily accounted for with this fractionation model.

The presence of amphibole phenocrysts in some of the late-stage, most evolved, Jorullo lavas (Luhr and Carmichael, 1985) provides strong evidence that at least some portion of the crystallization process occurred at pressures high enough to stabilize amphibole (> 500 MPa); we propose that fractionation of amphibole + olivine ± clinopyroxene drove the bulk melt evolution at depth. We modeled simple amphibole ± olivine fractionation with major element least squares modeling using the early and late

bulk lava data, the amphibole composition from an analyzed phenocryst in a late lava (Luhr and Carmichael, 1985), and Fo_{90} olivine. We found that fractionation of amphibole + olivine has a good fit ($\sum r^2 = 0.99$) compared to amphibole only ($\sum r^2 = 4.66$). Plotted in the major element diagrams of Figure 2.2 is the amphibole + olivine fractionation trend (thick dashed line), which corresponds to fractionation of 17.3 wt% amphibole and 6.7 wt% olivine. Because there is uncertainty as to whether amphibole would have been stable in the highest temperature melts (e.g., Moore and Carmichael, 1998; Grove et al., 2003; Nicholis and Rutherford, 2004), the earliest stages of fractionation may have involved olivine + clinopyroxene, with amphibole joining the assemblage (or replacing clinopyroxene by reaction relation) at temperatures between 1100-1150°C. We hypothesize that most of the original fractionating crystals were left behind at depth, perhaps in a deep crustal hot zone sill (Annen et al., 2006), and that ascending batches of melt then crystallized olivine during degassing. Thus most or all of the crystals in the tephra and lavas were formed during ascent, whereas the bulk composition of melt batches emanating from the deep reservoir became progressively more evolved over time due to deep fractionation.

5.4. Role of shallow assimilation – trace elements

While it seems that most of the bulk melt evolution can be explained by fractionation of amphibole + olivine ± clinopyroxene at depth, there is also evidence for shallow assimilation of granitic bedrock (Rubin et al., 2004). Granitic xenoliths were erupted in several of the middle and late lava flows at Jorullo, and in some localities are quite abundant. Disaggregated xenoliths in the lavas and the presence of plagioclase and

quartz xenocrysts in thin section suggest efficient consumption of the granites by the Jorullo magmas. Additionally, some trace elements are far more enriched in the late melt inclusions and bulk lavas (Luhr and Carmichael, 1985) than would be expected from simple fractionation. Figure 2.3 shows trace element data for melt inclusions and bulk tephra. The early and middle samples show increases in trace elements (Ba, La, Zr, Y) that fit well with simple fractionation (solid line). However, the late melt inclusions and late bulk tephra show enrichments in some elements (La, Zr, Y) that do not fit with the modeled 40% crystal fractionation. Also plotted in these figures are analyses of the La Huacana granite that comprises the bedrock around Jorullo and the xenoliths present in the lava flows; mixing between this granite and Jorullo melts can explain the enrichments in the later samples. Furthermore, these data suggest that the plumbing system at Jorullo evolved such that efficient assimilation of the shallow granite occurred, lending additional support to the development of a shallow storage region late in the eruption.

5.5. Olivine residence times

Olivine crystals in both the tephra and lava flows (Luhr and Carmichael, 1985) show Fo-rich cores with more evolved rims. Most olivine from the early and middle tephra have broad homogeneous cores and narrow, normally zoned rims. Olivine from the late tephra have more gradual normal zoning. We interpret the narrowness of the zoned rims in early and middle tephra to be the result of magma mixing or entrainment of earlier formed crystals by less Mg-rich melts just before eruption. Additionally, early olivine crystallized at a wide range of depths but were deposited within the same tephra layer, or eruptive unit. This suggests that olivine from various levels of the plumbing

system were re-entrained by the evolving melts rising from depth, consistent with the Jorullo bulk melt evolution driven by amphibole + olivine fractionation in the middle to lower crust.

The olivine residence time data (Figs. 2.5c, d) also support the formation of a shallow reservoir or storage system as the eruption progressed. The range of timescales for olivine storage increases from early to late in the eruption, suggesting that longer storage of crystals is facilitated late in the eruption by such a reservoir. Additionally, the observed correlation in the late-erupted olivine between crystal residence time and olivine core compositions (Fig. 2.5d) suggests that the olivine with more Fo-rich cores crystallized far earlier in the eruption (with residence times up to 1300 days), and then resided at shallow levels (based on the low entrapment pressures of middle and late melt inclusions) in a more evolved melt. Together, these data require the development of a region for long-term (months to years) crystal and melt storage at shallow levels, and support the idea of deep melt evolution followed by shallow olivine-dominated crystallization.

6. Cinder cone plumbing systems

This research gives new insight into the volatile content, crystallization processes, and plumbing system evolution of a cinder cone volcano. The eruption of Jorullo is the longest historically recorded cinder cone eruption, during which time the melts evolved. By comparing the bulk lava record (Luhr and Carmichael, 1985) to the melt inclusion record, we have found evidence for a multi-stage crystallization history at Jorullo. The melt inclusions record extensive crystallization in the upper crust driven by ascent,

degassing, and gas streaming, whereas the bulk lava and tephra compositions record deeper fractionation processes. Primitive, volatile-rich magma likely rose from the mantle beneath Jorullo, stalled and cooled in the lower crust, where it fractionated amphibole + olivine during the 15-year eruption. Such "cryptic amphibole fractionation" in the lower arc crust has recently been suggested by Davidson et al. (2007) to be a widespread phenomenon.

Whereas this initial stage of fractionation was likely driven by deep cooling, the Jorullo melt inclusions record evidence for crystallization driven by degassing during magma ascent. The early Jorullo melts rose from depth, likely in a complex network of dikes and sills, and crystallized olivine from 16 km to the near-surface (calculated assuming upper crustal density of 2600 kg/m^3). Olivine crystallized at pressures of 200-400 MPa due to fluxing of CO_2-rich gases through the conduit system, which forced melts to degas H_2O, and thus placed the melts below the relevant H_2O-undersaturated olivine-in curves. Subsequent degassing under near H_2O-saturated conditions as the melts rose induced further crystallization. The later-erupted melt inclusions record a significant change in the plumbing system, with olivine crystallization localized very shallowly beneath the volcano (80-700 m) and the addition of plagioclase ± clinopyroxene as crystallizing phases.

The shallowing of olivine crystallization depths, combined with both the extensive crystallization recorded by the groundmass and the increasing olivine residence times indicated by diffusion profiles, suggest that a shallow reservoir developed as the eruption of Jorullo progressed, facilitating degassing, crystallization, and melt storage. A similar shallow degassing region was suggested by Krauskopf (1948) to explain the

extrusion of degassed lava laterally from the base of Parícutin. This model would also hold for Jorullo, as degassed lavas effused from the base of the cone for much of the eruption. Additionally, degassing, crystallization, and release of latent heat in this shallow network would have enabled crustal assimilation of the granitic bedrock, a process seen both at Parícutin (McBirney et al., 1987) and Jorullo (Rubin et al., 2004). Development of such a reservoir seems applicable to long-lived cinder cones like Jorullo. For example, the eruption of Parícutin lasted for nine years and the melts similarly evolved over time, both due to fractionation and assimilation (Wilcox, 1954; McBirney et al., 1987). Because such reservoirs are capable of storing melts for extended periods of time and may feed the extensive lava flows, they may be a common feature of other long-lived cinder cone eruptions.

Bridge

In the previous chapter I described the degassing behavior and melt evolution of one cinder cone eruption. In the following chapter, I will compare and contrast the degassing behavior of several cinder cones throughout Mexico, and compare their behavior with that of larger volcanoes, such as Mt. Etna in Italy.

CHAPTER III

DEGASSING OF VOLATILES (H_2O, CO_2, S, CL) IN MONOGENETIC BASALTIC ERUPTIONS: IMPLICATIONS FOR VOLATILE SOLUBILITIES, VAPOR-MELT PARTITIONING, CRYSTALLIZATION, AND ERUPTION PROCESSES

This work is co-authored with Paul Wallace and Kathy Cashman who assisted with fieldwork and editing. I performed the laboratory work and was the primary author.

1. Introduction

The exsolution of volatiles from magma during ascent is the driving force for explosive eruptions. Until recently, studies of explosive volcanism have focused mainly on silicic systems. However, recent measurements of the pre-eruptive volatile concentrations in basaltic melts have demonstrated that mafic magmas can have high volatile contents (< 8 wt% H_2O, < 3000 ppm CO_2, < 4000 ppm S, < 3000 ppm Cl; Sisson and Layne, 1993; Roggensack et al., 1997; Cervantes and Wallace, 2003; Spilliaert et al., 2006a, 2006b; Wade et al., 2006; Benjamin et al., 2007; Johnson et al., 2008: Chapter II) and that these high volatile contents affect the explosivity of basaltic eruptions (Roggensack et al., 1997; Spilliaert et al., 2006b). Furthermore, an increasing number of studies have emphasized the effects of degassing on crystallization of ascending melts

(e.g., Sisson and Layne, 1993; Métrich et al., 2001; Roggensack; 2001; Atlas et al., 2006; Blundy and Cashman, 2005; Blundy et al., 2006; Johnson et al., 2008: Chapter II).

Degassing of volatiles is complex because the solubility of the different volatiles is variable and depends on melt composition, temperature, pressure, and in some cases, oxygen fugacity (e.g., Dixon and Stolper, 1995; Webster et al., 1999; Newman et al., 2000; Jugo et al., 2005). Melt inclusion H_2O and CO_2 concentrations, which can be used to calculate entrapment pressures, can be combined with S and Cl contents of melt inclusions and matrix glasses to provide estimates of the depth and extent of degassing of different volatiles (Metrich et al., 1993; Metrich et al., 2001; Gurenko et al., 2005; Spilliaert et al., 2006a, 2006b). However, these studies have focused on large or persistently active basaltic volcanoes (e.g., Etna), and similar studies have not been done on monogenetic volcanoes, in spite of the fact that they are the most abundant type of volcano on land (Vespermann and Schminke, 2002).

Here we present the pre-eruptive volatile concentrations (H_2O, CO_2, S, Cl) and major element compositions of olivine-hosted melt inclusions and matrix glasses from monogenetic volcanoes in central Mexico. Using these data, we assess the degassing behavior of volatiles in the basaltic magmas, including estimates of the vapor-melt partition coefficients for S and Cl, depths of degassing of the different volatiles, the role of degassing in causing crystallization, and the loss of S and Cl during ascent and eruption. Our data suggest that the degassing behavior of basaltic volcanoes is highly variable and may be influenced by the longevity of the eruption.

2. Samples and methods

We sampled tephra from nine monogenetic volcanoes (eight cinder cones and one maar) across the Michoacán-Guanajuato Volcanic Field (MGVF), Mexico (Fig. 3.1). When possible, samples were taken from throughout the tephra stratigraphy, from the basal layers of the tephra directly above the paleosol to the top of the tephra section. Loose olivine crystals from the tephra samples were separated, washed, and cleaned of adhered glass using HBF_4, and those with suitable melt inclusions (fully enclosed, glassy) were prepared for analysis.

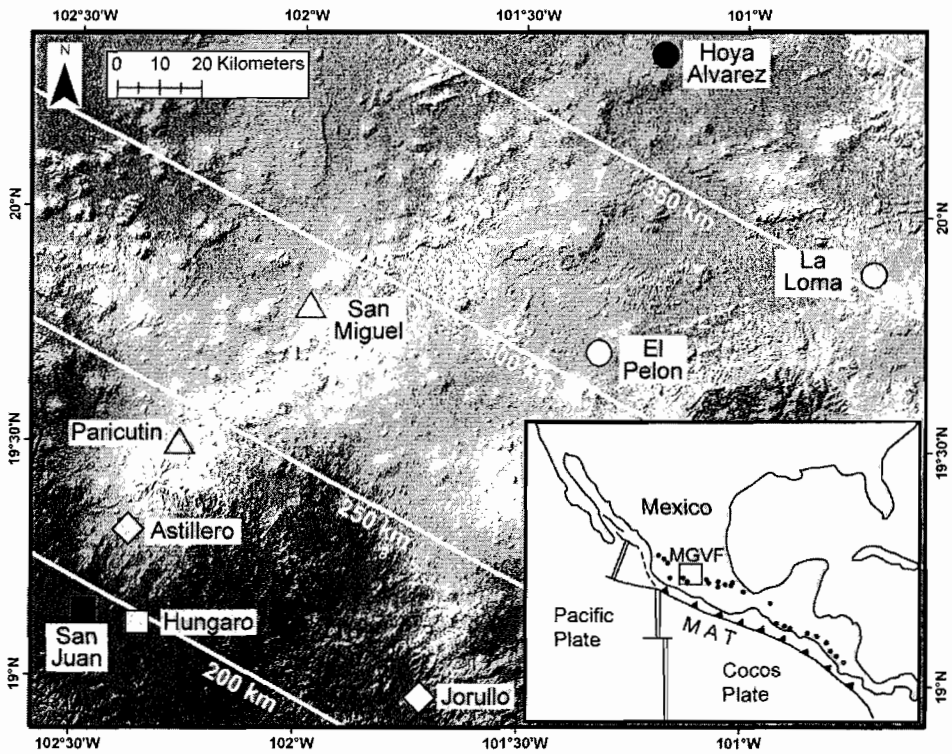

Figure 3.1. Map of samples from the Michoacán-Guanajuato Volcanic Field (MGVF). White contours indicate distance from Middle America Trench (MAT). Inset shows map of Mexico and tectonic setting, with location of MGVF denoted by a box. Dots indicate locations of volcanoes in Mexico and Central America.

Water and CO_2 concentrations in melt inclusions were analyzed by Fourier Transform Infrared Spectroscopy (FTIR) at the University of Oregon. Concentrations of H_2O and CO_2 were calculated using Beer's law: $c = MA/\rho d\varepsilon$, where M is the molecular weight of H_2O or CO_2, A is the measured absorbance of the band of interest, ρ is the room temperature density of basaltic glass, d is the thickness of the melt inclusion and ε is the molar absorption coefficient. In most samples, water concentrations were calculated using the total OH peak at 3550 cm^{-1} and an absorption coefficient of 63 ± 3 L/mol-cm (P. Dobson et al., unpublished data, cited by Dixon et al., 1995). In some instances, however, total H_2O was calculated using an average of the molecular H_2O peaks at 1630 cm^{-1} and 5200 cm^{-1} and the OH^- peak at 4500 cm^{-1}. In these cases absorption coefficients were calculated based on major element compositions (Dixon et al., 1995). CO_2 was calculated using the carbonate peaks at 1515 and 1435 cm^{-1}; an absorption coefficient was calculated (typically 290-300 L/mol-cm) based on the major element composition of each sample (Dixon and Pan, 1995). The background around the carbonate peaks is complex, and thus it is necessary to subtract a carbonate-free spectrum from each sample spectrum to obtain a flat background (Dixon et al., 1995). We measured the absorbance of the carbonate doublet peaks using a peak-fitting program (unpublished program by S. Newman).

Major and minor element (including S and Cl) compositions of melt inclusions, their olivine hosts, and tephra groundmass glass were analyzed on the Cameca SX-100 electron microprobe at the University of Oregon using a 15 kV accelerating voltage, 10 nA beam current (20 nA for olivine analyses), and a beam diameter of 10 μm. The beam current was increased to 40 nA when analyzing S and Cl, and count times were increased

to 80 s for S and 100 s for Cl. Based on previous analyses of FeO and Fe_2O_3 in MGVF lavas, we estimated the oxidation state of basaltic melts in the MGVF (Hasenaka and Carmichael, 1985). The slightly oxidized nature of the MGVF magmas (~ΔNNO + 0.5) corresponds to a peak position for S that is two-thirds of the way from anhydrite to pyrite (Wallace and Carmichael, 1994). In order to correct for decreasing counting rates for volatile elements (e.g., Na, K, Si, and Al) with time, we used a volatile correction routine that fits an exponential function to the decaying count rates for these elements, and then we extrapolated back to time zero. A combination of glass and mineral standards was used in the microprobe analyses.

To precisely determine the speciation of dissolved S in the melt inclusions, wavelength dispersive S Kα scans were performed on 2-4 inclusions per sample. Exposure to the electron beam has been shown to cause an increase in sulfur oxidation state for glasses in which most S is present as S^{2-} (Wallace and Carmichael, 1994) and to cause reduction of S^{6+} to S^{4+} in more oxidized glasses (Wilke et al., 2008). In order to minimize these effects the sample was moved relative to the electron beam every 20 seconds. A peak-fitting program was used to locate the position of the S Kα peak, and the oxygen fugacity of the melt was calculated following Wallace and Carmichael (1994).

All melt inclusion data were corrected for the effects of post-entrapment crystallization of olivine (Sobolev and Chaussidon, 1996) and diffusive loss of Fe (Danyushevsky et al., 2000). Post-entrapment crystallization correction involves adding equilibrium olivine, in incremental fractions of 0.1 wt%, into the melt inclusion composition until it is in equilibrium with its host olivine (as analyzed by electron

microprobe). There are two variables used in calculating the equilibrium olivine composition: the K_D value and the FeO/FeO^T ratio. We used a K_D of 0.3 ± 0.01 (Toplis, 2005) and FeO/FeO^T values of 0.7-0.9, based on whole rock lava data (Hasenaka and Carmichael, 1985) for each cone. Following the procedure of Danyushevsky et al. (2000) we also corrected the inclusions, if necessary, for post-entrapment Fe-loss. We plotted the melt inclusion FeO^T vs MgO data and either the bulk tephra XRF data or whole rock data from Hasenaka and Carmichael (1985). Inclusions with low FeO^T compared to the whole rock trend had FeO added back into their compositions until they matched the whole rock trend. All major element and volatile data discussed in the text and shown in figures are corrected values and are presented in tables in Appendix F.

3. Results

3.1. Melt compositions

The melt inclusions from the MGVF have mostly basaltic to basaltic andesitic compositions (Fig. 3.2). Melt inclusions from the cinder cones are medium-K calc-alkaline in composition, whereas the maar locality erupted more alkalic compositions. Fo-rich olivine (Fo_{88-91}) phenocrysts are present in tephra from many of the cones, but some of the more evolved magmas crystallized olivine (Fo_{75-87}) +/- plagioclase +/- clinopyroxene phenocrysts. Some suites of melt inclusions from individual volcanoes show decreasing MgO and increasing K_2O over time or within an individual layer suggesting evolution of the melt compositions by fractional crystallization and/or assimilation (Fig. 3.3). In general, the melt inclusions trap melts that are less evolved,

with lower incompatible element (K_2O, TiO_2, P_2O_5) concentrations, than the groundmass glasses.

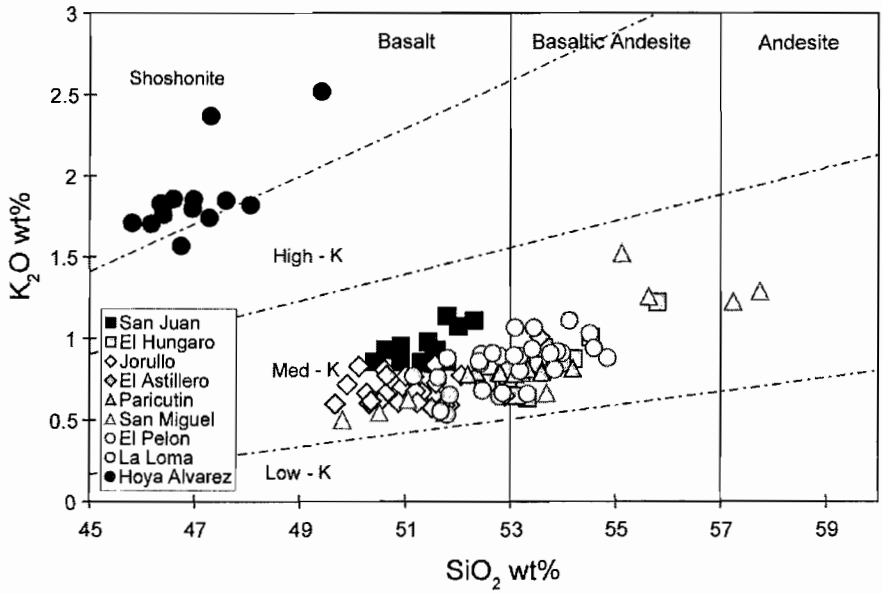

Figure 3.2. Melt inclusion K_2O and SiO_2 concentrations. Most MGVF melts plot in the medium-K basalt to basaltic andesite fields. Hoya Alvarez melts are more alkalic, with low SiO_2 and higher alkali contents.

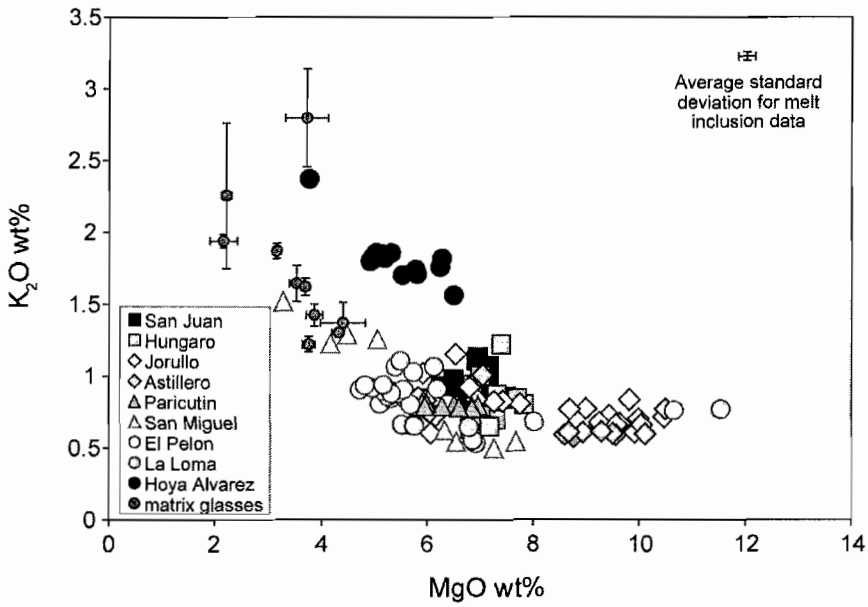

Figure 3.3. Melt inclusion and matrix glass K_2O and MgO concentrations. Melt inclusion compositions are less evolved than their respective matrix glasses.

3.2. Volatile concentrations – melt inclusions and matrix glasses

Melt inclusions trapped variably degassed melts with a wide range of dissolved volatile concentrations. The range in H_2O measured for inclusions at a given cinder cone is typically between 1 and 4 wt% H_2O, with higher concentrations (4-5.3 wt%) found at four localities (Fig. 3.4). Melt CO_2 concentrations for the cinder cones are highly variable, from levels below detection (< ~50 ppm) to 1500 ppm. However, the melt volatile contents of the maar locality, Hoya Alvarez, are consistently different from the cinder cones. Hoya Alvarez melt inclusions record low H_2O (0.4-1.4 wt%) and variable but elevated CO_2 (up to 3000 ppm, with one measurement of ~6000 ppm). The Hoya Alvarez melts roughly fit a closed-system degassing path (Fig. 3.4). Most cinder cone melt volatile contents, however, show significant variability, which cannot be explained entirely by closed-system degassing models (Fig. 3.4). Sulfur concentrations generally range between 1100 and 2000 ppm and measured Cl contents are typically between 900 and 1400 ppm, with lower Cl at Hoya Alvarez (400-700 ppm) (Fig. 3.5). The melt inclusions show no decrease in Cl as melt H_2O decreases and only low S concentrations in a few inclusions with low H_2O (Fig. 3.5). Within the cinder cones, concentrations of S in the matrix glasses are very low (< 70 ppm), indicating significant shallow degassing of S during eruption. Conversely, Cl concentrations in the matrix glasses remain high (~700-1000 ppm), suggesting Cl generally remains soluble in the melt through degassing and eruption. In a later section we use systematics of volatiles and K_2O to quantitatively assess extent of degassing and vapor-melt partitioning for Cl and S.

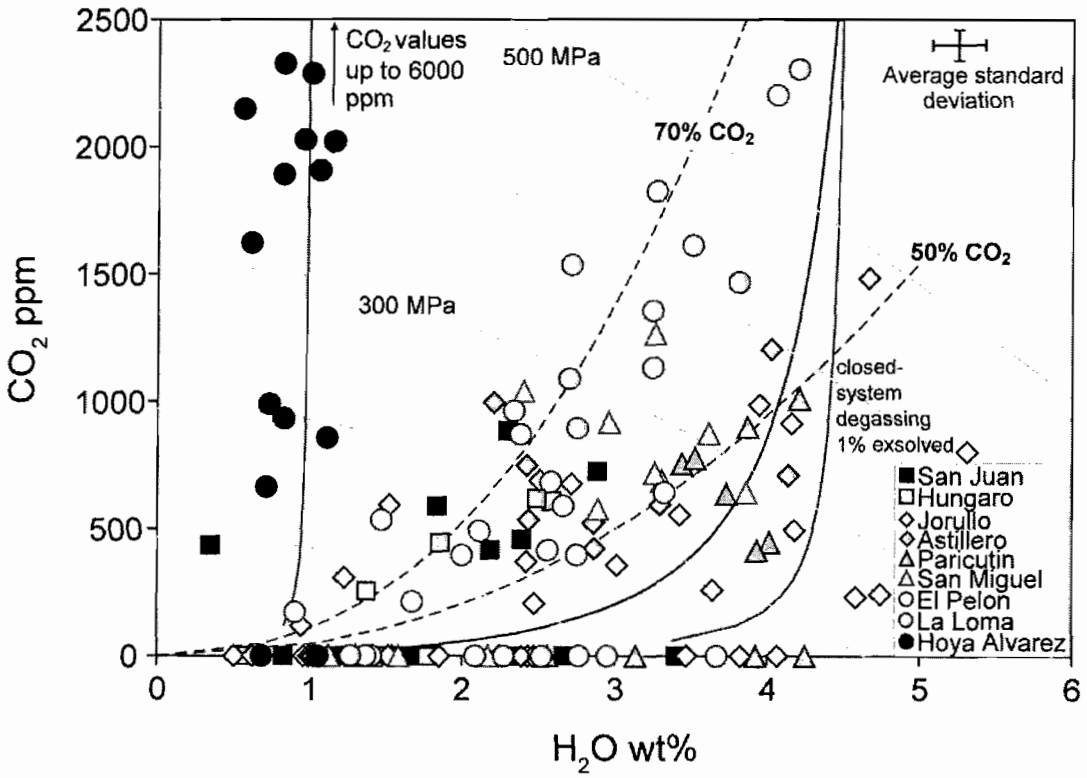

Figure 3.4. Melt inclusion CO_2 vs H_2O. Vapor saturation isobars (light gray), degassing paths (solid black), and isopleths of constant vapor composition (dashed lines) were calculated with VolatileCalc (Newman and Lowenstern, 2002). The low-H_2O degassing path (closed system, 1 wt% initial exsolved vapor) fits most of the Hoya Alvarez data. Two closed-system degassing paths are shown at ~ 4 wt% H_2O, one with 1 wt% initial exsolved vapor, the other with 2%. Neither curve sufficiently fit the melt inclusion CO_2 and H_2O data, but a large number of the melt inclusions plot between the isopleths representing vapors with 50 and 70 mol% CO_2.

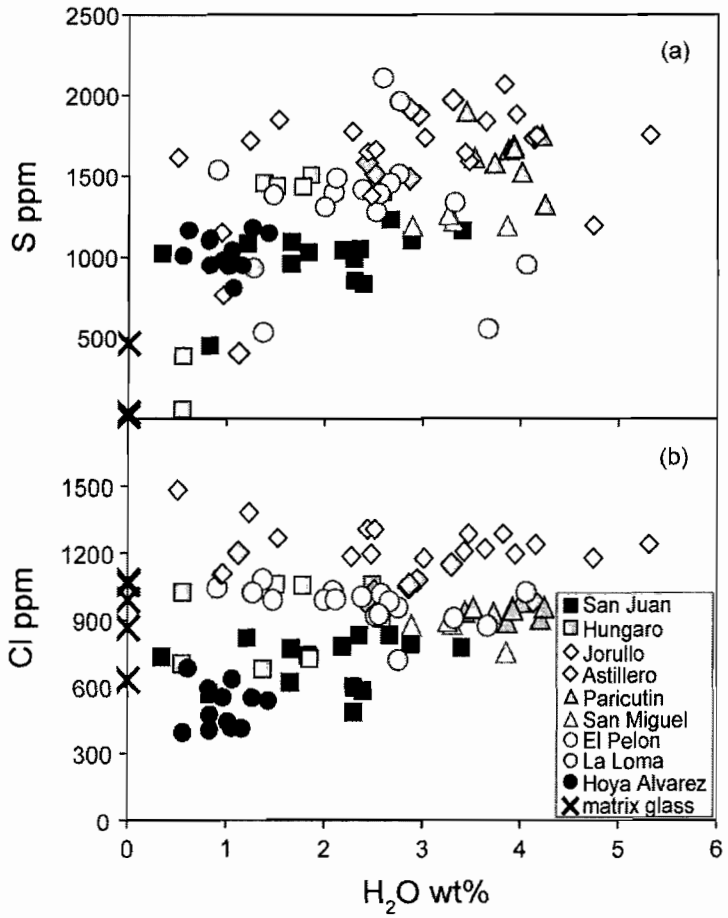

Figure 3.5. Melt inclusion and matrix glass S (a) and Cl (b) vs H_2O. Few inclusions show decreases in S with decreasing H_2O (a), but matrix glass S contents are generally low. Melt Cl concentrations show no change with decreasing H_2O, even in the matrix glasses.

4. Discussion

4.1. Melt evolution – importance of magma mixing and assimilation

Assessing the degassing behavior of a volcano requires knowledge of the melt evolution during eruption. The crystallization history of the melt is vital, as fractional crystallization can increase or decrease the concentrations of volatile elements in the melt. For example, fractionation of apatite could decrease melt Cl and F concentrations. Furthermore, as seen in studies of cinder cone eruptions like Paricutin (McBirney et al.,

1987; Luhr, 2001) and Jorullo (Luhr and Carmichael, 1995; Johnson et al., 2008: Chapter II), these systems are often very complex, and processes such as assimilation may be common, especially in longer-lived eruptions.

An additional complication in using melt inclusion data is the possibility that the compositions of trapped melts do not represent the compositions of the bulk melt. Melt inclusions form when the growing crystal traps small volumes of melt at the crystal-melt interface. Because melt inclusions are often trapped during relatively fast growth, elements that are slow to diffuse in the melt, like P_2O_5, may be preferentially enriched in the "boundary layer" surrounding the growing crystal. Thus, such elements may be more abundant in the melt inclusion than in the bulk melt. Recent crystallization experiments involving forsterite in the CMAS system (Faure and Schiano, 2005) and plagioclase and pyroxene in hydrous basaltic melt (Baker, 2008) show that crystals formed by initially rapid growth followed by isothermal annealing trap inclusions that are enriched in slowly diffusing species like Al_2O_3 and P_2O_5. In contrast, polyhedral forsterite formed by slow cooling in the CMAS system commonly trap melt inclusions that are similar to parental melt. For such crystals, there are no compositional gradients surrounding the olivine, suggesting growth is controlled by interface attachment rather than diffusion processes (Faure and Schiano, 2005).

To investigate the viability of the melt inclusion compositions in this study and to test for complexities in melt evolution, such as assimilation or magma mixing, we plotted ratios of incompatible elements in melt inclusions and bulk rock compositions (Fig. 3.6). Discrepancies between melt inclusion and bulk rock data may be indicative of factors such as boundary layer enrichment of the melts during inclusion formation, assimilation

of crustal rocks, mixing of crystals and inclusions that formed in compositionally distinct magmas, and fractional crystallization involving titanomagnetite or apatite. Figure 3.6a illustrates the generally good agreement between melt inclusion and whole rock data at Jorullo and Hoya Alvarez. However, the Hoya Alvarez inclusions record lower TiO_2/P_2O_5 concentrations than bulk rock, whereas K_2O/P_2O_5 remains constant. This suggests that the melts were affected by variable crystallization of titanomagnetite before melt inclusion entrapment, resulting in lower TiO_2 in the melts with progressive fractionation. Although this has a small affect on the Hoya Alvarez TiO_2 melt concentrations, other elements, including volatiles, should not be affected. Plotted in Figure 3.6b are melt inclusions that show significant variation from whole rock values. The samples from La Loma and San Miguel appear to have two separate melt populations; some groups of inclusions plot near the bulk rock data, whereas other groups are compositionally very different, suggesting that some of the olivines erupted may be xenocrysts. Figure 3.6c illustrates the complex evolution of the melts erupted at Parícutin. The early melt inclusions from this study and from Luhr (2001) all plot near the early lavas, but as the eruption progresses the K_2O/P_2O_5 ratio of the melts increases. This progressive evolution is likely the result of substantial assimilation of granitic bedrock, which has high K_2O/P_2O_5 and low TiO_2/P_2O_5 values (McBirney et al., 1987).

These plots illustrate the complexities of magma compositions from cinder cone volcanoes and show that they are susceptible to mixing and assimilation. However, we did not find evidence of boundary layer enrichment affects, which would cause melt inclusions to have lower ratios of K_2O or TiO_2 to P_2O_5 than whole rock samples due to very slow diffusion of P_2O_5 in the melt. This suggests that our melt inclusion

compositions are representative of the bulk melt from which they formed. Processes like assimilation would affect the bulk composition of the magma by adding certain elements, like K, to the basaltic melt, which would affect estimates of the extent of fractional crystallization based on incompatible elements. Melt inclusions from mixed populations of olivine could record very different ascent, degassing, and crystallization histories. Therefore, we have used only melt inclusion data from eruptions, or phases of an eruption in the case of Parícutin, that are representative of the bulk melt when assessing the degassing and solubility of volatile components (in section 4.3.).

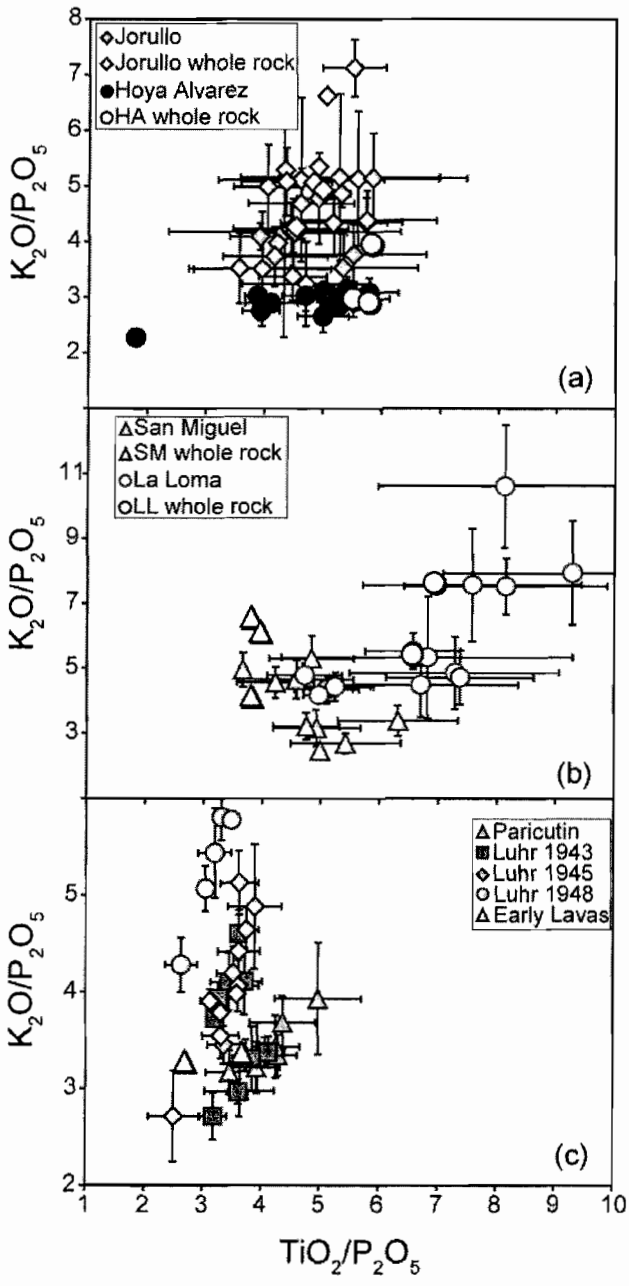

Figure 3.6. Melt inclusion and whole rock K_2O/P_2O_5 vs TiO_2/P_2O_5. (a) Melt inclusions from Jorullo and Hoya Alvarez melt plot near the whole rock compositions, illustrating that they accurately represent the bulk melt compositions. (b) Melt inclusions from San Miguel and La Loma are variable; some plot with the bulk rock compositions, while others are compositionally different, suggesting that some of the melt inclusions are hosted in xenocrystic olivine. (c) Melt inclusions from Paricutin show evolution toward higher K_2O/P_2O_5, which likely represents assimilation of granitic bedrock (McBirney et al., 1987). However, melt inclusions from this study and the early inclusions from Luhr (2001) plot near the early lava flows (McBirney et al., 1987), suggesting that these early melts have not been affected by assimilation.

4.2. Volatile degassing

Degassing of H_2O and CO_2 from magmas during ascent and eruption at MGVF cinder cones is complex. Based on vapor saturation isobars (Fig. 3.4), the melts with the highest volatile contents were trapped at pressures of 300-500 MPa. However, melt inclusions also record crystallization at very low pressures (< 50 MPa). Furthermore, whereas degassing of CO_2 and H_2O at volcanoes like Arenal and Irazú follow trends for closed-system degassing (e.g., Wade et al., 2006; Benjamin et al., 2007), closed-system models cannot account for all of the scatter in the MGVF volatile data. Similar scatter has been described at Etna (Spilliaert et al., 2006) and Jorullo (Johnson et al., 2008: Chapter II). In both cases, the melt inclusions that trapped high-CO_2, low-H_2O melts were explained by gas fluxing of CO_2-rich vapor from depth (e.g., Johnson et al., 2008: Chapter II and references therein). We find that this process not only applies to Jorullo but to many of the other MGVF cinder cones as well.

To illustrate the effects of gas fluxing, we have shown isopleths corresponding to vapors with 50 and 70 mol% CO_2 in Figure 3.4. The isopleths bracket nearly all of the data not explained by closed-system degassing, suggesting that fluxing of gases with 50-70 mol% CO_2 is a common process during basaltic eruptions throughout Mexico. These vapor compositions are similar to those estimated for Etna melts (Spilliaert et al., 2006), Jorullo (Johnson et al., 2008: Chapter II), and high-K minettes and basanites erupted at cinder cones in the Colima Graben to the west (Vigouroux et al., in review). Moreover, a compilation of basaltic melt volatile contents from arcs worldwide shows that many melts are in equilibrium with vapors with 50-75 mol% CO_2 (Fig. 3.7). This suggests that much of the variation in H_2O and CO_2 from basaltic magmas can be explained if primitive

mafic magmas in arcs typically have ≥ 0.7 wt% CO_2, similar to the estimate by Wallace (2005). The evidence for the pervasive effects of gas fluxing in volcanic conduit systems suggest that such magmas pond and degas CO_2-rich vapor at lower crustal depths

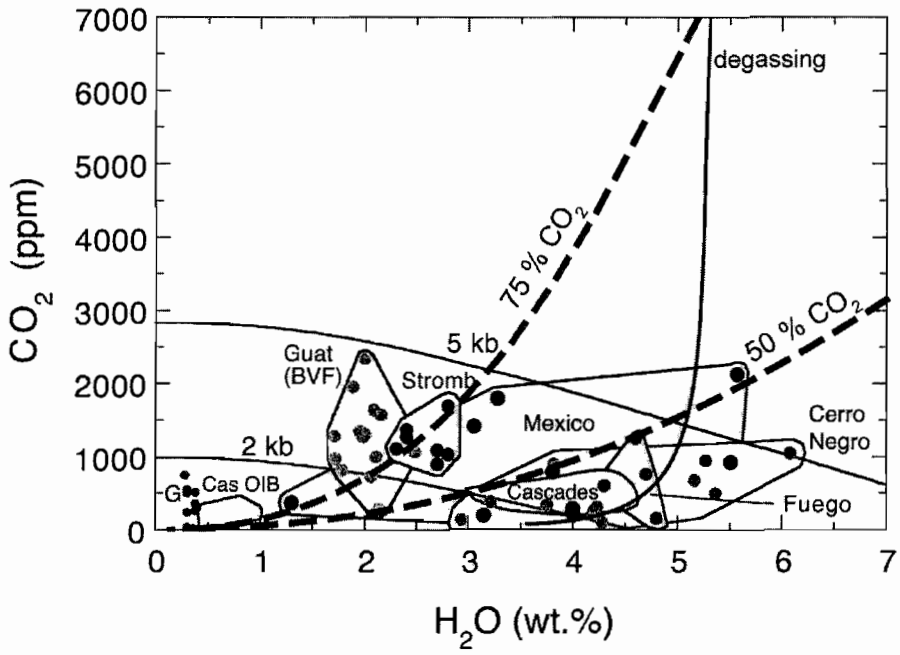

Figure 3.7. Compilation of CO_2 and H_2O from basaltic melts worldwide (from Wallace, 2005). Dashed lines are vapor isopleths, and the solid line represents the closed-system degassing path for a basalt with 5.3 wt% H_2O and 7000 ppm CO_2 at 1125°C (calculated using VolatileCalc, Newman and Lowenstern, 2002). Most of the melt CO_2 and H_2O concentrations in this plot fall between the 50 and 75 mol% CO_2 isopleths.

Furthermore, the gas-fluxing process seems to be restricted to pressures > 100 MPa. A large number of melt inclusions, from across the MGVF, were trapped between 100-300 MPa and plot between the two vapor isopleths. Spilliaert et al. (2006) reported a similar abundance of melt inclusions trapped at ~200 MPa, which they attribute to a magma ponding zone where melts stall, are fluxed with CO_2-rich gases from depth, and crystallize olivine. While a similar process may occur beneath the MGVF, the pressure

region between 100 and 300 MPa also corresponds to the pressures at which ascending basaltic andesite melts should cross the H_2O-saturated liquidus (based on eruption temperatures of ~1100-1150°C and the phase diagram of Moore and Carmichael, 1998) and begin extensive olivine crystallization. Therefore, the abundance of melt inclusions trapped between 100 and 300 MPa may simply be an artifact of the large amounts of olivine crystallization, and melt inclusion entrapment, that would occur at and below these pressures. The observation that fluxing of a vapor phase with 50-70 mol% CO_2 is common to basaltic melts throughout the MGVF suggests that the CO_2 contents of the parental basaltic magmas were similar, and that extensive and variable degassing occurred during ascent and crystallization to create the variability in CO_2 and H_2O observed in the melt inclusion data.

In spite of the complex degassing histories exhibited by MGVF magmas, it is clear from the melt inclusion data that CO_2 is less soluble in the melt than H_2O, consistent with experimental solubility data (Dixon and Stolper, 1995; Newman et al., 2000). Degassing of CO_2 must begin at pressures > 500 MPa. The degassing of H_2O is complicated by the effects of gas fluxing, but based on the closed-system degassing paths, H_2O begins substantial degassing at pressures of ~ 200 MPa.

Evidence for degassing of S and Cl, however, is minimal in the MGVF melt inclusions. Unlike other basaltic systems (e.g., Etna and Arenal; Spilliaert et al., 2006; Wade et al., 2006), the MGVF melt inclusions do not record degassing of S with H_2O (Fig. 3.5), suggesting S remains soluble in the melt during much of the magma ascent. However, the low S contents measured in matrix glasses suggest that significant degassing occurs shallowly, prior to or during eruption. Chlorine contents remain

constant with degassing of H_2O but unlike S, this pattern has been found at other basaltic volcanoes (e.g., Spilliaert et al., 2006; Wade et al., 2006). Comparison of the melt inclusion S and Cl to matrix glass S and Cl provides a rough estimate of the percent degassing of these volatile elements. For the cinder cones, the difference in melt inclusion S and matrix glass S suggest a loss of ~ 98% S during shallow ascent and eruption, whereas loss of Cl is only ~ 0-13%. The maar, Hoya Alvarez, has much higher groundmass glass S contents (~ 450 ppm) and similar Cl (~650 ppm) with a bulk loss of only ~ 50% S and no loss of Cl. This suggests that volatile degassing at this locality is different than the cinder cones, which will be explored below.

4.3. Degassing and melt evolution

Fractional crystallization of the MGVF melts increases the concentrations of incompatible elements, including volatiles and K_2O, in the melt. In order to assess the degassing behavior of volatiles during crystallization, we plotted H_2O/K_2O, S/K_2O and Cl/K_2O vs. K_2O for Jorullo, Parícutin, and Hoya Alvarez melt inclusions (Fig. 3.8). Whereas Parícutin melt inclusion compositions are clearly affected by assimilation later in the eruption, the melt inclusions analyzed in this study and those analyzed by Luhr (2001) from the early years of the eruption (1943-1945) do not show strong effects of assimilation. We assume that K_2O is totally incompatible, and thus is a proxy for the extent of fractional crystallization experienced by the melts. By normalizing the volatiles to K_2O we remove the effect of increasing volatile concentrations due to crystallization. Decreases in the volatile/K_2O ratios with increasing K_2O illustrate that degassing during crystallization occurred in both the Jorullo and Parícutin melts (Fig. 3.8). Both Jorullo

and Parícutin melt inclusions record decreasing S/K_2O with crystallization (i.e., increasing K_2O). Conversely, the constant ratios of S/K_2O and Cl/K_2O in the Hoya Alvarez melt inclusions suggests little to no degassing of these volatiles with crystallization, although lower concentrations of H_2O/K_2O and S/K_2O ratios in the groundmass suggest degassing of H_2O and S occurred shallowly. Hoya Alvarez melt Cl/K_2O contents remain constant with increasing K_2O, even in the groundmass, suggesting that no degassing of Cl occurred during eruption.

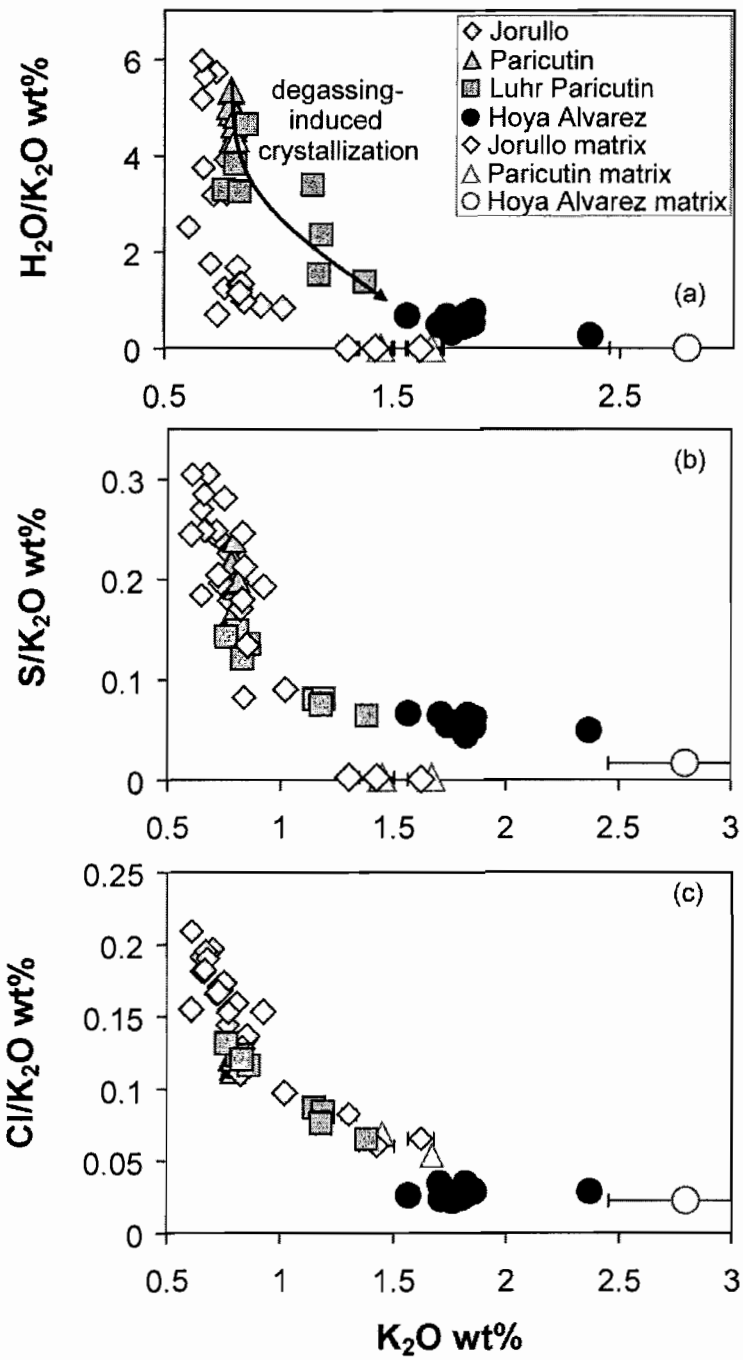

Figure 3.8. Ratios of volatiles/K_2O vs K_2O in melt inclusions and groundmass glasses from Jorullo, Parícutin (light squares from this study, dark squares from Luhr, 2001), and Hoya Alvarez. Decreases in H_2O/K_2O (a), S/K_2O (b), and Cl/K_2O (c) with increasing K_2O indicate degassing of the volatiles during differentiation of the magmas at Jorullo and Parícutin. Hoya Alvarez melts appear not to have degassed during differentiation, though decreases in H_2O/K_2O and S/K_2O in matrix glasses suggest shallow degassing of these volatiles.

Our results show that the degassing of Cl and S and crystallization of MGVF magmas were variable. The increase in K_2O with decreasing H_2O/K_2O in the Jorullo and Parícutin melts suggests that degassing of H_2O drove crystallization of these melts. The melt inclusion data show that crystallization of the melts at Jorullo and Parícutin was driven by loss of H_2O during ascent. Based on Figure 3.8, the exsolution of H_2O from the melt into the vapor phase stripped the melt of some S and Cl, resulting in decreases in these volatiles with increasing crystallization. The Hoya Alvarez melt inclusions, however, indicate that degassing of H_2O and S was minor, even during eruption. Although the melt inclusions record crystallization, as indicated by increases in K_2O, it was not induced by degassing of H_2O. This suggests a different mechanism for melt crystallization at Hoya Alvarez. Because most melt inclusions were trapped at pressures > 200 MPa (based on H_2O and CO_2), it seems likely that the Hoya Alvarez melts stalled in the middle to upper crust and cooled and crystallized without loss of volatiles. Furthermore, the relatively high S and Cl contents in the groundmass glass at Hoya Alvarez suggest that only minor degassing of S and no loss of Cl occurred during eruption. The high volatile content of the matrix glass is puzzling, as no other MGVF glasses record such high concentrations of volatiles, and possible explanations will be discussed in section 4.6.

4.4. Variations in S and Cl degassing with pressure

To further investigate the variations in degassing, we plotted melt inclusion and matrix glass S/K_2O and Cl/K_2O vs. pressure (calculated based on the concentrations of H_2O and CO_2 in the melt inclusions using VolatileCalc; Newman and Lowenstern, 2002)

for Jorullo, Parícutin, and Hoya Alvarez (Fig. 3.9). Of the three localities, Jorullo and Parícutin melt inclusions record decreases in S, more noticeably at Parícutin, beginning at pressures less than ~200 MPa. Conversely, Hoya Alvarez melt inclusions record no change in S during ascent. The low S in the groundmass glasses of Parícutin and Jorullo indicates extensive shallow degassing after the entrapment of the last melt inclusions (< 40 MPa for Parícutin, < 6 MPa for Jorullo). The high S in the matrix glass of Hoya Alvarez is unique; concentrations this high were not found at any of the other MGVF localities. Sulfur concentrations at Hoya Alvarez do not decrease over the pressures at which melt inclusions were trapped (> 200 MPa), but the slightly lower S in the groundmass suggest minimal (50%) loss of S at shallow levels. Melt inclusion Cl/K_2O decreases slightly with decreasing pressure at both Jorullo and Parícutin, but the matrix glass Cl contents are higher than the initial melt Cl, because the increase in concentration due to crystallization is greater than the decrease caused by minor degassing. Chlorine appears to degas primarily at shallow levels (< 100 MPa) in the Jorullo and Parícutin melts, and matrix glass Cl/K_2O contents are lower than in the melt inclusions. Similarly to S, Hoya Alvarez Cl contents show no change with decreasing pressure, and the matrix glass concentrations indicate no degassing of Cl, even at shallow levels. Overall, the melts at Jorullo and Parícutin degassed S deeper than Cl, at pressures similar to those calculated for Etna (~140 MPa). Based on the high concentrations of S and Cl in groundmass glasses, the Hoya Alvarez melts had not completely degassed at the time of eruption and quenching of the tephra clasts.

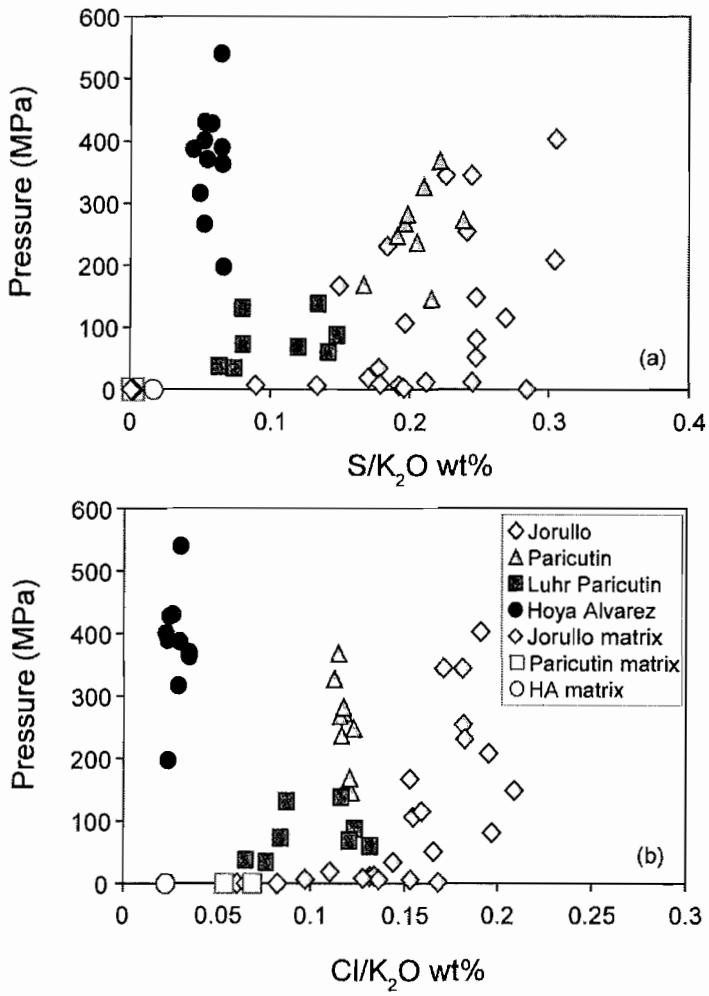

Figure 3.9. Pressure dependence of S/K_2O (a) and Cl/K_2O (b) at Jorullo, Parícutin, and Hoya Alvarez. Pressures are calculated based on the concentrations of H_2O and CO_2 in the melt inclusions using VolatileCalc (Newman and Lowenstern, 2002). Based on these plots, degassing of S occurs at pressures < 200 MPa at Jorullo and Parícutin, and Cl degasses at lower pressures (< 100 MPa). Parícutin data from Luhr (2001) shown in dark squares.

4.5. Vapor-melt partitioning of S and Cl

The degassing behavior of S and Cl in MGVF melts is variable and, based on both melt inclusion and groundmass glass analyses, is dependent on pressure. Using the melt inclusion and matrix glass S and Cl concentrations, we modeled the vapor-melt partitioning of these volatiles during differentiation. Following the method described for

simple open-system degassing in Spilliaert et al. (2006), we estimated vapor-melt D_S and D_{Cl} values for Jorullo, Parícutin, and Hoya Alvarez. The D-values are calculated assuming that during open-system degassing, the vapor phase leaves the melt and the concentration of the volatile species in the melt, X_i, can be calculated using the Rayleigh fractionation equation:

$$X_i = X_{iO} \times f^{Di-1}$$

where X_{iO} is the initial concentration of species *i*, D*i* is the vapor-melt partition coefficient, and f is the remaining melt fraction, which can be approximated from increases in melt K_2O. Thus in plots of $\ln(X_i)$ vs. $\ln(K_2O)$ best-fit lines have a slope of 1-D_i, enabling us to estimate D_i. The partition coefficients, D_i, indicate the affinity of a species for the vapor versus the melt. Values of $D_i > 1$ indicate preferential partitioning of the species into the vapor phase, whereas $D_i < 1$ indicates preferential partitioning into the melt. A partition coefficient equal to 1 indicates that the species is distributed equally between the melt and vapor, thus for $D_i = 1$ there is some loss of the volatile species into the vapor.

Figure 3.10 shows lnS and lnCl vs $\ln K_2O$ for our melt inclusion and matrix glass data. The D_S values estimated from these plots agree with the variations in S/K_2O with pressure shown in Figure 3.9; at high pressures, Hoya Alvarez melts have the lowest D_S values (0.7), followed by Jorullo (D_S ~1.2) and Parícutin (D_S ~2). The D_S values increase at low pressures, as indicated by the trends defined by the matrix glass data (D_S ~6-14). At higher pressures, the D_S values calculated for MGVF melts are slightly higher than those for high pressure Etna inclusions (D_S = 0.35; Spilliaert et al., 2006). The D_S values at Etna also increase at lower pressures, reaching high values (D_S ~25) near the surface.

Overall, the D_S values of MGVF melts are similar, although D_S values are slightly lower at Hoya Alvarez, which is consistent with the lack of S degassing deduced from melt inclusion S/K_2O. The general degassing pattern of the MGVF melts is similar to Etna (gray fields, Fig. 3.10), although Etna melts degas S more vigorously at low pressures (< 140 MPa).

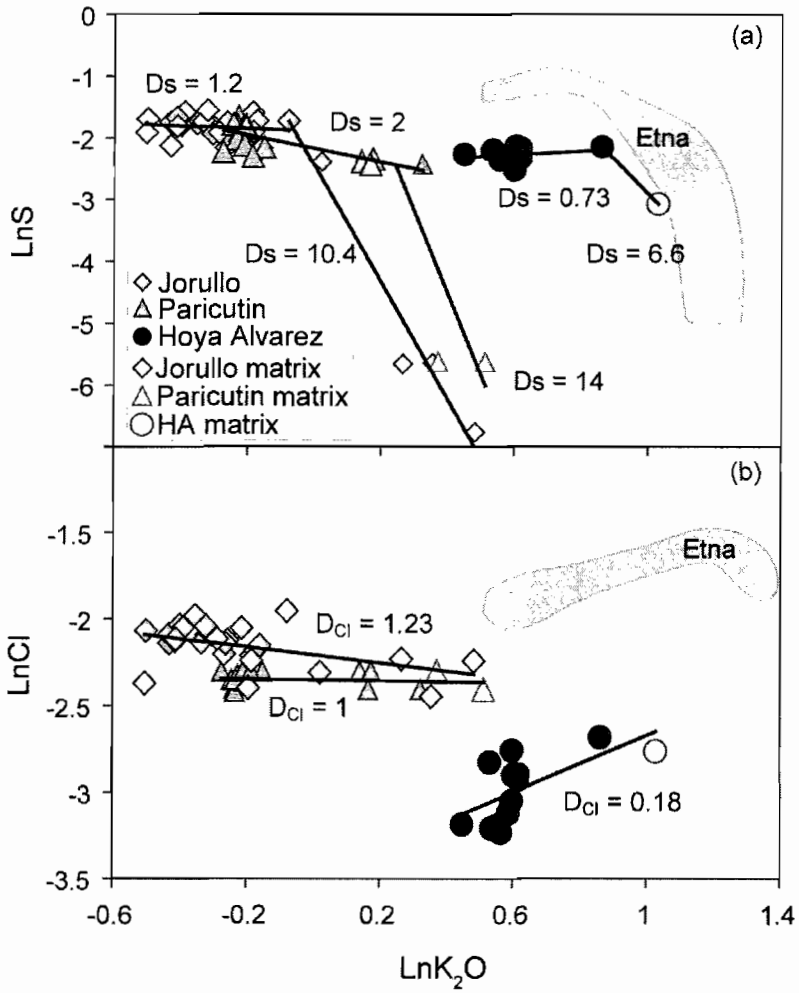

Figure 3.10. Variations of lnS (a) and lnCl (b) during melt differentiation (lnK_2O). Best fit lines were used to calculate the vapor-melt distribution coefficients D_S and D_{Cl} shown in both plots. Groundmass glasses are shown as open symbols.

These observations about the pressure dependence of D_S are supported by calculations of the behavior of D_S with pressure based on thermodynamic modeling (Scaillet and Pichavant, 2005). Figure 3.11 shows the variation in D_S with decreasing pressure, calculated at 1100°C and an oxygen fugacity of NNO +1. This modeled relationship illustrates that D_S values are < ~2.5 at pressures > 200 MPa, and that D_S increases rapidly at pressures < 200 MPa. This supports the high calculated D_S values based on the groundmass glasses and the low values at higher pressures calculated from the melt inclusion data.

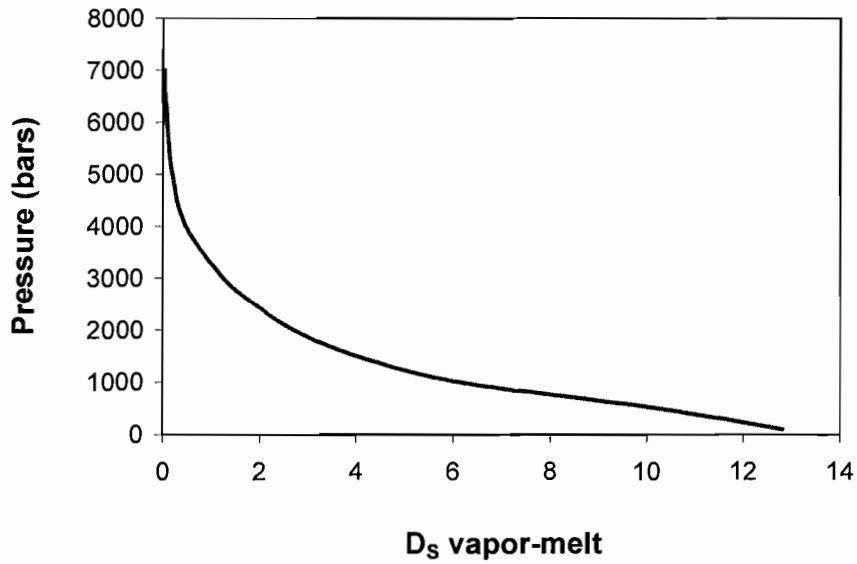

Figure 3.11. Pressure dependence of S vapor-melt partitioning based on thermodynamic modeling (Scaillet and Pichavant, 2005).

The vapor-melt partition coefficients for Cl in the MGVF melts calculated from melt inclusion data also agree with the behavior of Cl during differentiation inferred from Cl/K_2O values (Fig. 3.10). The values calculated for D_{Cl} in Hoya Alvarez melts are low (D_{Cl} ~0.18), which supports the lack of Cl degassing during differentiation. Melt inclusions from Parícutin and Jorullo have similar values of D_{Cl} (1 and 1.23; Fig. 3.10b).

Unlike S, the partitioning of Cl does not change with pressure; melt inclusion and groundmass glass measurements of Cl and K_2O plot on the same linear trend, with no indication of increased degassing of Cl at very low pressures. Overall, the values of D_{Cl} for MGVF melts suggest that Cl partitioned preferentially into the melt, with little degassing during ascent and eruption. The low values of D_{Cl} at Hoya Alvarez are strikingly similar to D_{Cl} calculated for Etna (D_{Cl} ~0), indicating that these melts, unlike Jorullo and Parícutin, degassed little to no Cl.

4.6. Sources of variable degassing in basaltic melts

Magmas erupted at three localities in the MGVF show variability in the degassing behavior of S and Cl. Although the degassing behavior of S is similar for magmas from both the MGVF and Etna, degassing of Cl is more variable. In the following sections we investigate the roles of magmatic oxygen fugacity, eruption style and longevity, and melt composition on the degassing of S and Cl in basaltic melts.

4.6.1. Oxygen fugacity

The oxygen fugacity of basaltic magmas influences the speciation of S, which in turn affects S degassing. Several studies have demonstrated that sulfate is the dominant S species in basaltic melts at high fO_2 (> FMQ +1) and that sulfide is the dominant species in low-fO_2 melts (Carroll and Rutherford, 1985; 1987; Luhr, 1990; Jugo et al., 2005). Furthermore, experimental studies have shown that S solubility in mafic magmas increases dramatically at higher oxygen fugacities (Carroll and Rutherford, 1985; 1987; Luhr, 1990; Jugo et al., 2005). Not only does the oxygen fugacity of the melt affect

concentrations of S, but it also affects degassing. Sulfate preferentially partitions into a hydrous vapor phase, thus, exsolution of H_2O during degassing should decrease melt S concentrations (Keppler, 1999). This suggests that the partitioning of S into the vapor phase should increase with increasing melt fO_2. Plotted in Figure 3.12 are the oxygen fugacities of MGVF melts and the melt S contents. Using the SKα peak positions of MGVF melt inclusions, the calculated oxygen fugacities of MGVF magmas range from FMQ +1.2 to FMQ +2.1. There is significant scatter in the data, but melts with high S contents (1500-2000 ppm) have higher fO_2 (+1.8-2). Our data generally agree with the sulfur solubility limits calculated by Jugo et al. (2005). They found that the solubility of S in a basaltic melt dramatically increases at FMQ +1.8. MGVF melts plot around this transition: Hoya Alvarez melts, with their low fO_2, were likely saturated in sulfide, Jorullo melts plot around the transition in stability from sulfide to sulfate, and the other MGVF melts generally plot in the region of much higher S solubility where solubility is controlled by sulfate saturation. Although our samples bridge the transition, the melts that should be saturated in sulfide (Hoya Alvarez) do have lower concentrations of S than those with higher fO_2.

Low fO_2 (FMQ +1.3) may also explain the lack of S degassing observed in Hoya Alvarez melts. The higher fO_2 values of Jorullo melts (FMQ +1.6), Parícutin melts (similar to Jorullo, based on SKα peak positions reported in Luhr, 2001), and Etna melts (FMQ +1.2 to +2; Kamenetsky et al., 1996) also correspond to similar S degassing behavior inferred from melt inclusions, and all have higher inferred D_S values than Hoya Alvarez. However, the difference in fO_2 between Hoya Alvarez and the other basaltic melts does not seem to be large enough to explain the surprising lack of degassing of S

even at very low pressures. Based on the calculations of the pressure dependence of D_S (Fig. 3.11) lower oxygen fugacities should correspond to lower values of D_S. However, this effect would be small for Hoya Alvarez, and we would still expect the D_S value of the melt to increase significantly at low pressures. This suggests that differences in oxygen fugacity alone are not enough to explain the lack of degassing during the eruption of Hoya Alvarez.

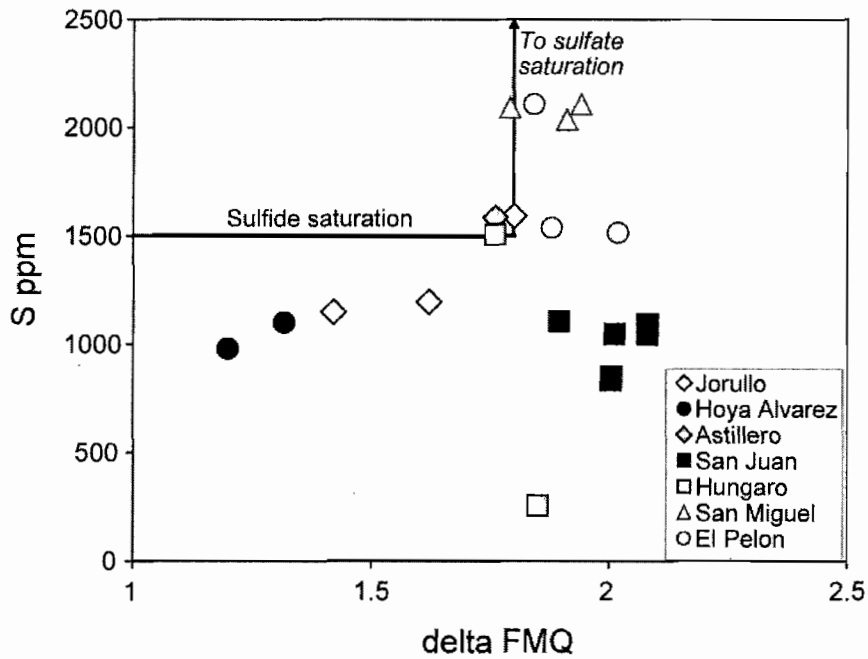

Figure 3.12. Concentration of S in MGVF melt inclusions and the oxygen fugacity of the melts (Δ FMQ). The solid horizontal line represents sulfide saturation (Jugo et al., 2005). The transition to sulfate stability occurs at fO_2 of ~ FMQ +1.8, which corresponds to an increase in the concentration of S dissolved in basaltic melts (Jugo et al., 2005). The experimentally determined sulfate solubility limit is 1.3 wt% S (Jugo et al., 2005).

4.6.2. Longevity of eruptions and eruption style

Factors such as eruption longevity and eruption style may also affect the degassing of basaltic magmas. In long-lived volcanoes, like Etna, conduit systems beneath the volcano are well-established, likely causing degassing of melts. The same

may be true for longer lived cinder cones, like Jorullo and Parícutin. The plumbing system at Jorullo evolved over the 15-year eruption, developing a shallow region of magma storage and crystallization where degassing and assimilation occurred (Johnson et al., 2008: Chapter II). Such a region may have formed during the eruption of Parícutin as well, as suggested by the localization of degassing and crystallization (< 150 MPa) late in the eruption as well as evidence for assimilation of bedrock. While the degassing behavior of these long-lived eruptions is generally similar, the lack of shallow degassing recorded by the Hoya Alvarez melt inclusions makes it unique. The eruption of Hoya Alvarez was both phreatomagmatic and magmatic, and was likely shorter in duration than the eruptions of Parícutin or Jorullo. Thus, it seems unlikely that a well-defined conduit system had time to develop during the explosive, maar-forming eruption. Furthermore, the phreatomagmatic nature of the eruption requires that the rising magma interacted with groundwater. This magma-water interaction may have occurred at or below the Earth's surface, and the groundwater would rapidly quench the rising magma (Mastin et al., 2004). This may have prevented the complete degassing of the Hoya Alvarez melts during final ascent and eruption.

4.6.3. Melt composition

While the high concentrations of S in the matrix glasses at Hoya Alvarez may be the result of quenching at higher pressures, the behavior of Cl in the melt inclusions remains perplexing. The increase in melt Cl concentrations during crystallization is not observed in any of the other MGVF melts, but the vapor-melt partitioning of Cl is very similar in the Hoya Alvarez and Etna melts (Fig. 3.10b). The Hoya Alvarez and Etna

melts are compositionally similar, with higher alkalis and lower SiO_2 than other MGVF melts (Fig. 3.2). This compositional difference may be the reason for the high solubility of Cl and low D_{Cl} at these volcanoes. Experiments by Webster et al. (1999) demonstrate the compositional dependence of Cl solubility, which increases strongly with increased molar $(Al_2O_3+Na_2O+CaO+MgO)/SiO_2$ of the melt. This suggests that the high alkali and low SiO_2 contents of both Etna and Hoya Alvarez melts increased the solubility of Cl, resulting in lower D_{Cl} values.

5. Conclusions

We analyzed the pre-eruptive compositions and volatile contents of melts from monogenetic volcanoes in the MGVF of Mexico using olivine-hosted melt inclusions. Using these data, we were able to compare and contrast the degassing behavior and melt compositional evolution within these localities, and compare them with larger, long-lived basaltic systems (Etna and Arenal). However, an important precursor to this work was assessing the reliability of our melt inclusion data. We found that, in spite of the relative simplicity and small volume of cinder cone eruptions, factors such as magma mixing and assimilation are fairly common in monogenetic volcanoes, which complicate the melt evolution and degassing history. However, we did find that most melt inclusions are representative of the bulk melt compositions from which they formed and were not affected by boundary layer effects.

Degassing in basaltic systems is complex. We found that most MGVF melts required gas-fluxing of a vapor with 50-70 mol% CO_2 to explain the CO_2 and H_2O variations in the melt inclusions. Interestingly, this vapor composition is similar to those

estimated for CO_2-fluxing in other basaltic systems, suggesting that primary basaltic magmas in arcs have similar and high initial CO_2 concentrations. In nearly all melts, S partitioned equally between the melt and vapor (inferred D_S values of ~1-2) until low pressures (< ~ 10 MPa), when extensive shallow degassing occurred prior to and during eruption (D_S values of 6-14 inferred using matrix glass compositions). The inferred D_{Cl} values of MGVF melts were low for both melt inclusions and groundmass glasses (<1.2 for all volcanoes) suggesting that degassing of Cl was not pressure dependent. Overall we find that the degassing behavior of the long-lived basaltic cinder cones in the MGVF is very similar to that of larger basaltic volcanoes, like Etna.

We discovered that there exists significant variability in degassing and crystallization processes within monogenetic volcanoes of the MGVF. Melts erupted at Hoya Alvarez, a maar, showed little to no degassing of S or Cl, even upon eruption. We attribute the lack of degassing to a combination of melt composition, low melt fO_2, which would favor partitioning of S into the melt, and the phreatomagmatic eruption style, in which groundwater would have interacted with and quenched the rising magma. The more alkaline melt compositions at Hoya Alvarez increased the solubility of Cl in the melt, which caused a low vapor-melt D_{Cl}. The melts erupted at the cinder cones, Jorullo and Parícutin, have higher D_S and D_{Cl} values, higher melt fO_2, and melt inclusions record evidence for degassing-induced crystallization.

Bridge

In the previous chapters I assessed the melt evolution and degassing of one cinder cone volcano (Ch. II) and compared and contrasted the degassing behavior of several cinder cones (Ch. III) in a subduction-zone setting. In the following chapter I discuss the origin of such subduction-zone volcanoes, in terms of subduction processes and melt generation in the mantle.

CHAPTER IV

THE ORIGIN OF H_2O-RICH SUBDUCTION COMPONENTS BENEATH THE MICHOACÁN-GUANAJUATO VOLCANIC FIELD, MEXICO: INSIGHTS FROM MAGMATIC VOLATILE CONCENTRATIONS, OXYGEN ISOTOPES, AND THERMAL MODELS

This work is co-authored with Paul Wallace, who assisted in the field, Ilya Bindeman, who aided in the oxygen isotope analyses, and Vlad Manea, who created the 2-D thermal models. All co-authors aided in the editorial process and I was the primary author and performed the laboratory analyses.

1. Introduction

The role of volatiles, most importantly H_2O, in arc magmas is broad. H_2O-rich fluids or melts released from the subducting slab flux the mantle wedge, producing the partial melts that lead to arc volcanism (Gaetani et al., 1993; Gaetani and Grove, 1998; Sisson and Grove, 1993a, 1993b; Stolper and Newman, 1994). Furthermore, the amount of H_2O added to the mantle wedge governs the extent of partial melting in the mantle (Carr et al., 1990; Stolper and Newman, 1994; Kelley et al., 2006). While some arc magmas are produced by decompression melting and have low volatile contents (Sisson and Bronto; 1998; Cervantes and Wallace, 2003; Grove et al., 2006), most arc magmas

result from flux melting of the mantle wedge. Magmas in volcanic arcs often erupt explosively and have been shown to contain high concentrations of volatiles (H_2O, CO_2, S, Cl), with H_2O concentrations of 3-5 wt% commonly measured in arc basalts worldwide (Sisson and Layne, 1993; Roggensack et al., 1997, Roggensack, 2001b; Walker et al., 2003; Cervantes and Wallace, 2003; Wade et al., 2006; Benjamin et al., 2007; Johnson et al., 2008: Chapter II).

While there have been numerous studies of the volatile contents of individual arc volcanoes in recent years (e.g., Gurenko et al.,2005; Wade et al., 2006; Benjamin et al., 2007) there have been few studies looking at volatile variations across arcs (Walker et al., 2003; Sadofsky et al., 2007; Portnyagin et al., 2007). Since volatiles are added to the mantle wedge by an H_2O-rich subduction-derived component, variations in volatile concentrations across a volcanic arc reflect devolatilization in the subducting material and melting processes in the mantle wedge. Across-arc datasets that include volatiles, trace elements, and stable and/or radiogenic isotopes are useful for determining the composition and origin of subduction-derived components added to the mantle wedge (Stolper and Newman, 1994; Eiler et al., 2005; Wysoczanski et al., 2006; Sadofsky et al., 2007; Portnyagin, 2007).

Understanding devolatilization of subducted materials and magma production in arc settings has been a fundamental problem for many fields in geology. Many studies have focused on the stability and pressure-temperature breakdown of hydrous minerals in the subducting slab (e.g., Schmidt and Poli, 1998; Kerrick and Connolly, 2001, Schmidt and Poli, 2004). Recent work has shown that the breakdown of hydrous phases in the oceanic crust is a continuous process, with H_2O being stored in a wide range of hydrous

phases that are stable at progressively higher pressures (~ 3 GPa) and temperatures (Schmidt and Poli, 2004; Kerrick and Connolly, 2001). Furthermore, studies have shown that fluids released from the downgoing slab could hydrate the mantle wedge, forming hydrous minerals such as serpentine and chlorite, and that the subsequent downdragging of this hydrated peridotite by the downgoing slab may be an important process in producing hydrous melts in volcanic arcs (Grove et al., 2006; Wysoczanski et al., 2006). However, low concentrations of H_2O and fluid mobile elements (e.g., B, Ba) measured in some arc magmas behind the volcanic front have suggested that the flux of H_2O-rich components decreases behind the volcanic front (Walker et al., 2003; Hochstaeder et al., 1996).

Knowledge of the materials being subducted and the specific pressure-temperature conditions during subduction are fundamental to understanding dehydration processes. For example, the role of sediments in formation of fluids or melts in subduction zones has been increasingly shown to be important in arcs worldwide (Plank and Langmuir, 1992; Johnson and Plank, 1999; Kelemen et al., 2003; Plank, 2005; Singer et al., 2007; Portnyagin et al., 2007). Trace element data are good indicators of sediment-derived fluids or melts (e.g., high Th/La or Th/Nd ratios; Plank, 2005) and of melts from subducted oceanic crust (e.g., high Sr/Y ratios; Martin et al., 2005). However, the stability of hydrous minerals in subducted oceanic crust and sediment varies from arc to arc and is dependent on the specific pressure-temperature conditions within the slab and mantle wedge. Recent studies of subduction zones have employed 2-D thermal models to predict the pressure-temperature regimes in the subducting slab (e.g., Rupke et al., 2002; Manea et al., 2004, 2005). Combining thermal models with phase diagrams for

subducting components (sediment, altered oceanic crust, serpentinized mantle) and geochemical data for arc magmas has been extremely useful in investigating the origin of H_2O-rich subduction components in arcs (e.g., Rupke et al., 2002).

Quantifying the composition and origin of hydrous fluids or melts added to the mantle wedge beneath arcs begins with measurements of magmatic volatile contents at the surface. Combining primary magma trace element data and measurements of melt volatile concentrations has enabled estimates of the composition of the H_2O-rich subduction component (fluid and/or melt) (e.g., Stolper and Newman, 1994; Eiler et al., 2005; Eiler et al., 2007; Portnyagin et al., 2007). However, to ascertain the origin of such H_2O-rich components, oxygen isotopic data have also proven extremely important. Recent work has shown that low $\delta^{18}O$ values in arc settings may be related to the dehydration of serpentinite in the mantle portion of the subducting slab (Eiler et al., 2005), whereas high $\delta^{18}O$ values may be the result of crustal assimilation (Harmon and Hoefs, 1995) or inherited from fluids or melts from altered oceanic crust (Dorendorf et al., 2000) or sediments (Eiler et al., 2005).

Here we present the results of an across-arc study of volatile contents and melt compositions from olivine-hosted melt inclusions from the Michoacán-Guanajuato Volcanic Field of central Mexico (MGVF). The primitive nature (e.g., Fo_{87-90} olivine in many samples) of the MGVF magmas allows us to calculate both primary melt compositions and mantle volatile contents. These data, combined with oxygen isotope ratios of olivine phenocrysts and 2-D thermal models of the subduction zone beneath the MGVF, allow us to estimate the source and composition of the H_2O-rich subduction components added to the mantle wedge. This multi-disciplinary approach permits us to

more precisely distinguish the specific components in the subducted slab that produced the H_2O-rich components and to constrain where devolatilization of the slab and flux-melting in the mantle wedge occurred.

2. Geologic setting – Michoacán-Guanajuato Volcanic Field, Mexico

Volcanism in Mexico is related to subduction of the Rivera (in the west) and Cocos plates beneath the North American plate at the Middle America Trench (Fig. 4.1). The Cocos plate subducting beneath the MGVF is young (11-17 Ma at the trench; Pardo and Suarez, 1995), and is thus relatively hot. The Trans-Mexican Volcanic Belt (TMVB) is a broad zone of volcanism that spans the country from west to east and contains several discrete volcanic fields. The Michoacán-Guanajuato Volcanic Field (MGVF) is located to the west of Mexico City and contains ~ 900 cinder cones (Hasenaka and Carmichael, 1985). The MGVF is an ideal locality for this study. First, it has an abundance of young (Holocene) cinder cones (Hasenaka and Carmichael, 1985) that are distributed over large distances behind the volcanic front. Second, most of the cinder cones are basaltic to basaltic andesite in composition, and published bulk rock geochemical data for many cones (Hasenaka and Carmichael, 1985) enabled us to sample those that are compositionally most primitive.

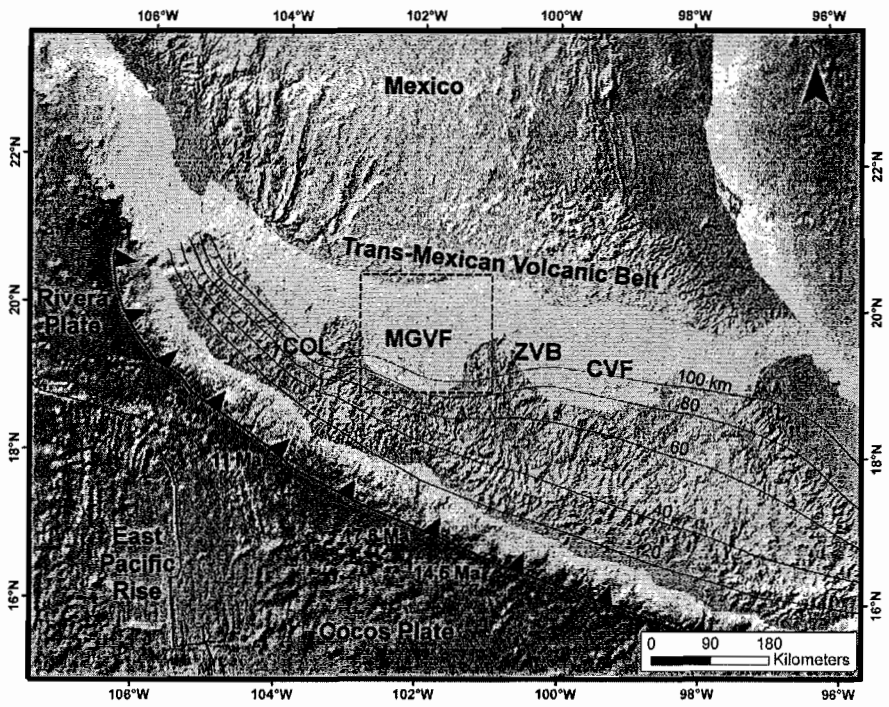

Figure 4.1.The Trans-Mexican Volcanic Belt and offshore plate boundaries. Ages of the subducting Cocos plate near the Middle America Trench and contours to the top of the subducting slab are from Pardo and Suarez (1995). Locations of discrete volcanic fields in central Mexico are abbreviated as follows: MGVF = Michoacán-Guanajuato Volcanic Field, ZVB = Zitácuaro-Valle de Bravo volcanic field, CVF = Chichináutzin Volcanic Field, COL = Colima Volcano.

3. Samples and Analytical Methods

3.1. Melt inclusions and olivine hosts

We sampled tephra from nine monogenetic volcanoes (eight cinder cones and one maar) across the MGVF at varying distances from the Middle America Trench spanning from the volcanic front to roughly 175 km behind the front (Fig. 4.1). When possible, samples were taken from the basal layers of the tephra blanket (in contact with the soil) in order to compare the earliest erupted samples at each volcano, which commonly have the most primitive compositions of the sequence (e.g., Johnson et al., 2008: Chapter II).

Loose olivine crystals from the tephra samples were separated, washed, and those with suitable melt inclusions (fully enclosed, glassy) were prepared for analysis.

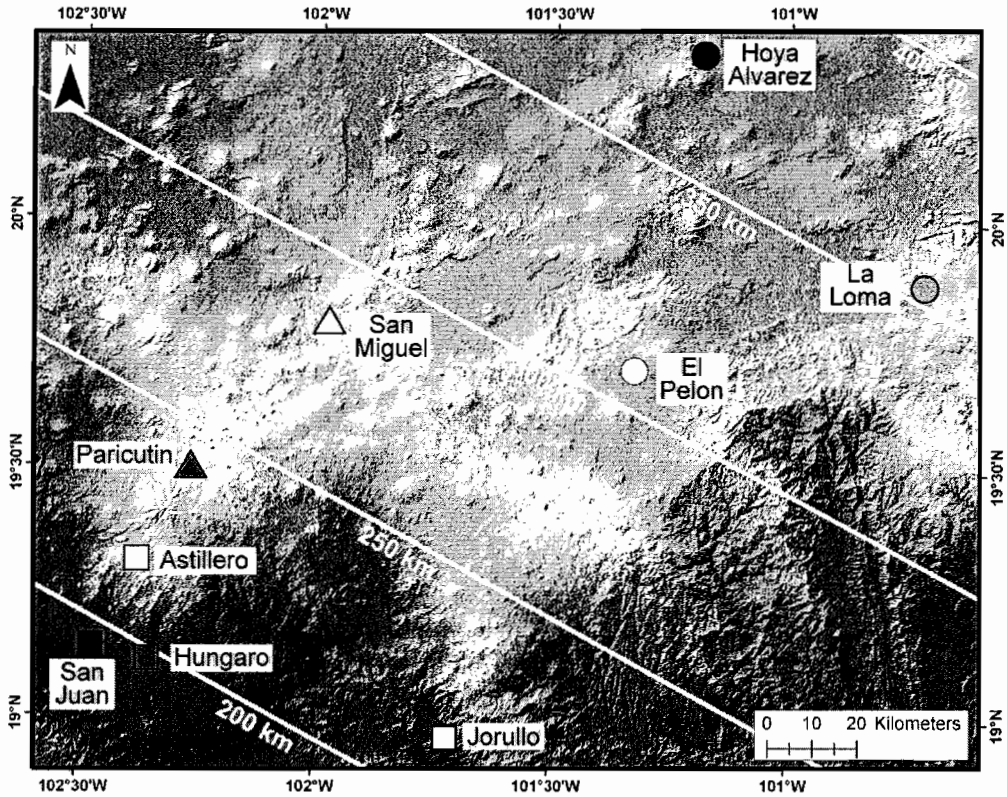

Figure 4.2. Sample locations from this study within the MGVF. White lines show distance from the Middle America Trench.

Major and minor element (including S and Cl) analyses of melt inclusions and their olivine hosts were obtained on the Cameca SX-100 electron microprobe at the University of Oregon using a 15 kV accelerating voltage, 10 nA beam current (20 nA for olivine analyses), and a beam diameter of 10 μm. The beam current was increased to 40 nA when analyzing S and Cl, and count times were increased to 80 s for S and 100 s for Cl. Based on previous analyses of FeO and Fe_2O_3 in MGVF lavas, we estimated the oxidation states of basaltic magmas in the MGVF (NNO = +0.5-1; Hasenaka and

Carmichael, 1985), which correspond to a SKα peak position that is two-thirds of the way from anhydrite to pyrite (Wallace and Carmichael, 1994). In order to minimize loss of counts on volatile elements (e.g., Na, K, Si, and Al) we used a volatile correction program that fit an exponential function to the decaying count rates for these elements and then extrapolated back to time zero. A combination of glass and mineral standards was used in microprobe analyses, and analytical errors are reported in Table 4.1. Melt inclusion trace element concentrations were measured using laser ablation ICP-MS at Oregon State University. Details of the technique are summarized in Kent et al. (2004)

Water and CO_2 concentrations in melt inclusions were analyzed by Fourier Transform Infrared Spectroscopy (FTIR) at the University of Oregon. Concentrations of H_2O and CO_2 were calculated using Beer's law: $c = MA/\rho d\varepsilon$, where M is the molecular weight of H_2O or CO_2, A is the measured absorbance of the band of interest, ρ is the room temperature density of basaltic glass, d is the thickness of the melt inclusion and ε is the molar absorption coefficient. In most samples, water concentrations were calculated using the total OH peak at 3550 cm^{-1} and an absorption coefficient of 63 ± 3 L/mol-cm (P. Dobson et al., unpublished data, cited by Dixon et al., 1995). In some instances, however, total H_2O was calculated by summing the average concentrations of the molecular H_2O peaks at 1630 cm^{-1} and 5200 cm^{-1} together with the concentration from the OH^- peak at 4500 cm^{-1}. In these cases absorption coefficients were calculated based on major element compositions (Dixon et al., 1995). CO_2 was calculated using the carbonate peaks at 1515 and 1435 cm^{-1}; an absorption coefficient was calculated (typically 290-300 L/mol-cm) based on the major element composition of each sample (Dixon and Pan, 1995). The background around the carbonate peaks is complex, and

thus it is necessary to subtract a carbonate-free spectrum from each sample spectrum to obtain a flat background (Dixon et al., 1995). We measured the absorbance of the carbonate doublet peaks using a peak-fitting program (unpublished program by S. Newman). Based on uncertainties in thickness measurements and absorbance values, average 1 standard deviation uncertainty in H_2O is ± 0.2 wt% and in CO_2 ± 80 ppm.

Oxygen isotopes were measured on separated and cleaned olivine crystals that did not contain obvious melt inclusions and that had minimal inclusions of spinel or other oxides. Isotope analyses were performed at the University of Oregon using CO_2 laser fluorination and BrF_5 reagent on multiple grains of olivine. Oxygen was converted to CO_2 gas in a platinum-graphite converter, and the gas was measured and then analyzed on an MAT 253 mass spectrometer. Measurements were made on two to three samples of olivine from each cone, with each sample weighing between 1.1-2.0 mg, yielding precision on multiple analyses of ± 0.01-0.02. Eight to eleven standards of San Carlos olivine ($\delta^{18}O$ = 5.35‰) and Gore Mt. Garnet ($\delta^{18}O$ = 5.75‰) were analyzed along with the unknowns.

3.2. Geodynamic modeling of subduction beneath the MGVF

Modeling of subduction beneath the MGVF was performed by Vlad Manea at the Universidad Nacional de México (Juriquilla). The models were created using a system of 2-D Stokes equations and a 2-D steady-state heat transfer equation, assuming a strong temperature-dependent viscosity in the mantle wedge (details in Manea et al., 2004, 2005). The rheological parameters used in the thermal models are as follows: a mantle wedge viscosity (η_o) of 10^{20} Pa s and an activation energy for olivine (E_a) of 250 kJ/mol.

Variations in E_a from 150 to 300 kJ/mol only result in very small temperature increases in the mantle wedge (< 25° C; Manea et al., 2005). A small degree of frictional heating was introduced ($\mu = 0.017$) along the thrust fault between the subducting and continental plates. Models were created for the present-day slab geometry and the geometry at 3 Ma, which is assumed to be similar to the present-day geometry to the east of the MGVF (i.e., slab depth of 100 km at 350 km from the trench). In both models, the convergence rate is 5 cm/yr and the slab age is 13 Ma.

3.3. Melt inclusion corrections

All melt inclusion data were corrected for post-entrapment crystallization of olivine (Sobolev and Chaussidon, 1996) and diffusive loss of Fe (Danyushevsky et al., 2000). We have corrected for post-entrapment crystallization by adding equilibrium olivine, in incremental fractions of 0.1 wt%, back into the melt inclusion until the melt inclusion composition is in equilibrium with its host olivine (as analyzed by electron microprobe). There are two variables used in calculating the equilibrium olivine composition: the K_D value and the FeO/FeO^T ratio. We used a K_D of 0.3 ± 0.01 (Toplis, 2005) and FeO/FeO^T values of 0.7-0.9, based on the whole rock lava data (Hasenaka and Carmichael, 1985) for each cone. Following the procedure of Danyushevsky et al. (2000) we also corrected the inclusions, if necessary, for post-entrapment Fe-loss. We plotted the melt inclusion FeO^T vs MgO data and either the bulk tephra XRF data or whole rock data from Hasenaka and Carmichael (1985). Inclusions with low FeO^T compared to the whole rock trend had FeO added back into their compositions until they matched the whole rock trend.

4. Results

4.1. Melt compositions

In order to compare volatile contents and melt compositions across the MGVF, we calculated primary (parental) melt compositions for each volcano in this study. For the purpose of calculating primary melt compositions, we have assumed that such melts were in equilibrium with mantle olivine (Fo_{90}). Two of the cinder cones sampled erupted melts with Fo_{90-91} olivine and thus were considered primary melts. With the exception of one locality, Hoya Alvarez, the remainder of our samples contained olivine crystals that are close to mantle compositions (Fo_{86-91}). For these samples, we assumed that the slightly lower-Fo olivine resulted from fractionation of olivine alone, an assumption supported by olivine being the only or dominant phenocryst in the deposits. Thus, we estimated primary melt compositions for these samples by incrementally adding olivine into the melt inclusion major element composition until it was in equilibrium with Fo_{90} olivine. As illustrated in Figure 4.3, this correction was minimal, as most melts crystallized olivine with compositions of Fo_{88-91}. One locality, Hoya Alvarez, erupted more evolved melts, with Fo_{65-78} olivine. Correcting these melts to Fo_{90} by olivine addition only yields erroneous results, as these melts were clearly evolved and contained large megacrysts of olivine, plagioclase, and clinopyroxene. Because of these complexities, we modeled the fractionation paths of melts with similar compositions (i.e., alkali basalts, see Chapter III) that were in equilibrium with Fo_{90} olivine. We found that an alkalic basalt from the Rio Grande rift, New Mexico (McMillan et al., 2000), when fractionated via isobaric crystallization in MELTS (Ghiorso and Sack, 1995), produced the melt compositions erupted at Hoya Alvarez by fractionation of 23% olivine, 20%

plagioclase, and 6% clinopyroxene (a total of 49% fractionation). Thus, we corrected the volatile and trace element compositions at Hoya Alvarez for 49% fractionation, and we assumed that the major element composition of the primary melts resembled that of the Rio Grande basalts. In this paper we present melt compositions and volatile concentrations that represent the primary mantle melts in equilibrium with Fo_{90} (both melt and primary compositions are shown in Table 4.1).

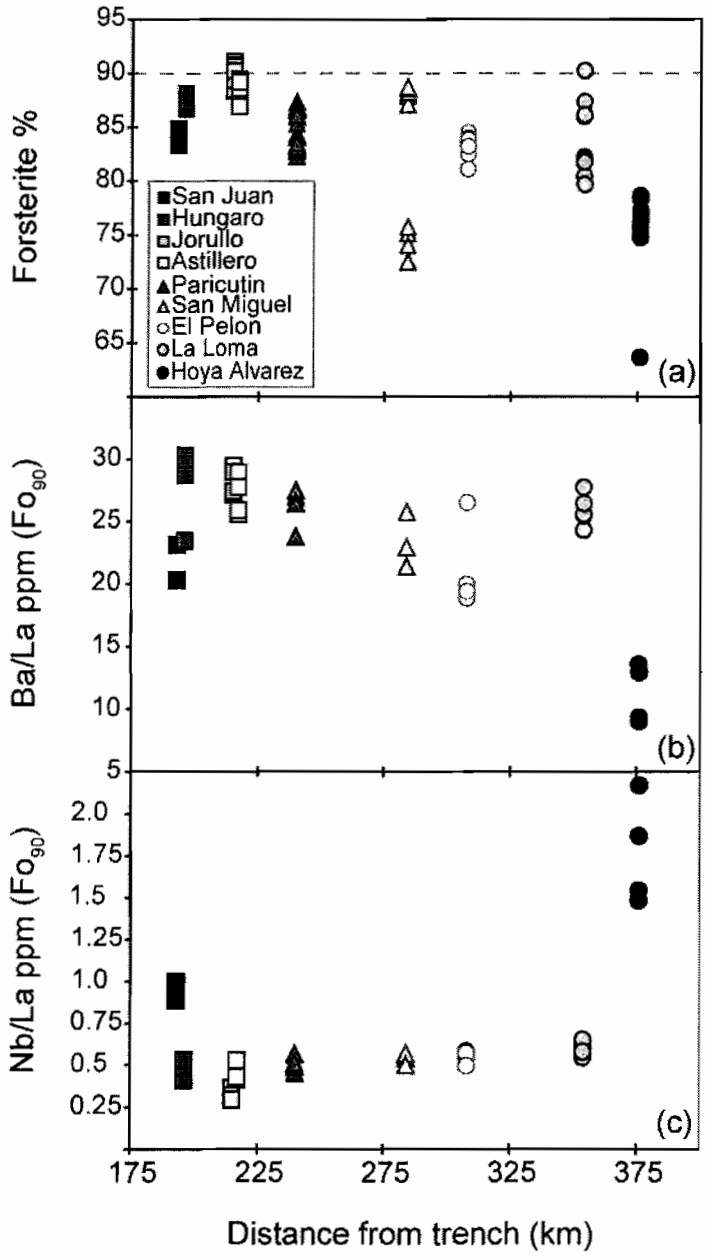

Figure 4.3. Across-arc variations in olivine and melt compositions. (a) Fo-content of olivine phenocrysts across the arc are generally high (Fo_{86-91}), with no distinct trends. Primary melt Nb/La (b) and Ba/La (c) similarly show no systematic variations across the arc.

Table 4.1. Mean compositions of melt inclusions, parental melts, and subduction-derived components

	San Juan	El Hungaro	Jorullo	El Astillero	Paricutin	San Miguel	El Pelon	La Loma	Hoya Alvarez
Melt inclusion compositions corrected for PEC and Fe-loss									
SiO_2	51.41 ± 0.53	53.69 ± 0.92	51.12 ± 0.75	51.10 ± 1.11	53.12 ± 0.61	53.62 ± 2.97	53.30 ± 0.85	52.67 ± 0.96	47.00 ± 0.91
TiO_2	1.11 ± 0.11	0.92 ± 0.05	0.74 ± 0.07	17.37 ± 1.11	18.92 ± 0.33	18.20 ± 1.75	18.82 ± 0.75	17.88 ± 1.33	17.64 ± 0.48
Al_2O_3	18.18 ± 0.43	18.01 ± 0.87	17.31 ± 0.91	8.36 ± 0.52	7.18 ± 0.07	7.87 ± 1.42	7.58 ± 0.24	8.25 ± 0.27	12.03 ± 0.50
FeO	9.29 ± 0.16	7.49 ± 0.18	7.50 ± 0.15	9.09 ± 0.95	6.44 ± 0.39	5.60 ± 1.48	5.26 ± 0.29	6.82 ± 1.90	5.25 ± 0.94
MnO	0.10 ± 0.02	0.09 ± 0.01	0.10 ± 0.05	8.73 ± 0.39	8.16 ± 0.12	8.44 ± 2.08	8.44 ± 0.35	9.05 ± 0.81	8.10 ± 0.56
MgO	6.93 ± 0.33	7.12 ± 0.51	9.38 ± 0.85	3.53 ± 0.73	4.11 ± 0.37	3.93 ± 0.22	4.09 ± 0.23	3.31 ± 0.52	4.13 ± 0.51
CaO	8.29 ± 0.36	7.85 ± 0.48	8.89 ± 0.30	0.66 ± 0.14	0.80 ± 0.01	0.91 ± 0.41	0.89 ± 0.05	0.80 ± 0.19	1.87 ± 0.26
Na_2O	3.51 ± 0.17	3.79 ± 0.47	4.08 ± 0.23	0.89 ± 0.07	0.95 ± 0.05	1.08 ± 0.10	1.21 ± 0.07	0.94 ± 0.22	2.94 ± 0.37
K_2O	0.94 ± 0.10	0.84 ± 0.17	0.72 ± 0.07	0.12 ± 0.05	0.09 ± 0.02	0.12 ± 0.05	0.10 ± 0.05	0.13 ± 0.03	0.17 ± 0.04
P_2O_5	0.25 ± 0.03	0.21 ± 0.03	0.16 ± 0.02	0.17 ± 0.02	0.24 ± 0.02	0.23 ± 0.05	0.32 ± 0.02	0.15 ± 0.06	0.65 ± 0.14
H_2O (max) wt%	3.40	3.69	5.30	4.13	4.24	3.86	3.67	4.20	1.42
S (max) ppm	1232	1507	2066	1969	1895	2107	2108	2021	1180
Cl (max) ppm	833	1061	1406	1200	980	911	1082	1172	1002
Fo % (range)	83.3 - 84.9	86.7 - 88.2	88.4 - 91.1	86.9 - 89.4	85.4 - 87.4	72.5 - 88.8	81.1 - 84.5	79.7 - 90.3	63.6 - 78.7
Parental melt compositions									
Rb	13 ± 2	9 ± 1	7 ± 1	5 ± 1	8 ± 1	6 ± 1	16 ± 1	8 ± 1	11 ± 1
Ba	263 ± 18	267 ± 26	183 ± 15	173 ± 21	211 ± 9	170 ± 5	292 ± 41	125 ± 25	154 ± 20
Th	0.93 ± 0.00	0.48 ± 0.01	0.40 ± 0.08	0.35 ± 0.09	0.62 ± 0.03	0.54 ± 0.02	1.27 ± 0.14	0.77 ± 0.16	1.43 ± 0.26
U	0.35 ± 0.15	0.26 ± 0.04	0.08 ± -	0.15 ± 0.03	0.25 ± 0.05	0.13 ± 0.05	0.51 ± 0.02	0.25 ± 0.04	0.45 ± 0.07
Nb	11.4 ± 0.9	4.6 ± 0.3	2.0 ± 0.2	2.9 ± 0.4	4.1 ± 0.3	3.9 ± 0.2	7.5 ± 0.4	2.8 ± 0.9	24.3 ± 1.7
Ta	0.53 ± 0.05	0.25 ± 0.05	0.15 ± -	0.11 ± 0.03	0.22 ± 0.05	0.17 ± 0.02	0.37 ± 0.12	0.18 ± 0.05	1.37 ± 0.16
La	12 ± 2	10 ± 1	7 ± 1	6 ± 1	8 ± 1	7 ± 1	14 ± 1	5 ± 1	14 ± 2
Ce	28 ± 2	23 ± 2	15 ± 2	16 ± 2	20 ± 1	19 ± 1	35 ± 2	12 ± 2	29 ± 1
Pb	3.72 ± 0.38	4.24 ± 0.21	3.73 ± 0.33	2.98 ± 0.64	3.97 ± 0.57	2.87 ± 0.16	4.55 ± 0.33	2.53 ± 0.42	1.28 ± 0.09
Sr	390 ± 44	478 ± 11	448 ± 35	455 ± 50	538 ± 20	450 ± 13	751 ± 104	485 ± 38	311 ± 30
Nd	13.5 ± 1.2	11.4 ± 2.0	9.8 ± 2.0	9.6 ± 0.5	10.6 ± 0.2	10.5 ± 0.9	16.8 ± 2.1	7.2 ± 1.4	13.2 ± 1.2
Zr	91 ± 6	83 ± 4	71 ± 1	58 ± 9	70 ± 5	76 ± 5	113 ± 5	48 ± 9	91 ± 11
Sm	2.75 ± 0.44	2.08 ± 0.47	3.24 ± 2.46	2.42 ± 0.28	2.58 ± 0.39	3.04 ± 1.27	3.02 ± 0.42	1.48 ± 0.46	2.70 ± 0.74
Eu	0.89 ± 0.16	0.87 ± 0.05	1.01 ± 0.31	0.85 ± 0.14	0.81 ± 0.11	0.94 ± 0.11	1.18 ± 0.08	0.74 ± 0.22	0.88 ± 0.11
Ti	5306 ± 437	4685 ± 438	3746 ± 482	4725 ± 601	4870 ± 148	5857 ± 115	6141 ± 264	3890 ± 730	7902 ± 944
Dy	2.42 ± 0.33	2.19 ± 0.46	2.54 ± 0.57	2.06 ± 0.27	2.14 ± 0.10	2.75 ± 0.61	2.64 ± 0.29	1.69 ± 0.32	1.91 ± 0.40
Y	14 ± 1	11 ± 1	14 ± 2	12 ± 2	12 ± 1	16 ± 2	16 ± 2	10 ± 2	11 ± 2
Yb	1.41 ± 0.30	1.25 ± 0.67	1.51 ± 0.50	1.06 ± 0.37	1.01 ± 0.28	1.63 ± 0.21	1.43 ± 0.26	1.04 ± 0.34	0.91 ± 0.14

Table 4.1. *(continued)*

	San Juan	El Hungaro	Jorullo	El Astillero	Paricutin	San Miguel	El Pelon	La Loma	Hoya Alvarez
Mantle melting									
F	0.16 ± 0.04	0.21 ± 0.06	0.16 ± 0.05	0.20 ± 0.05	0.19 ± 0.04	0.14 ± 0.03	0.14 ± 0.03	0.24 ± 0.06	0.09 ± 0.01
H_2O (max)	2.27 ± 0.25	3.27 ± 0.33	5.30 ± 0.76	3.99 ± 0.27	3.95 ± 0.40	3.17 ± 0.33	3.18 ± 0.28	4.06 ± 0.52	0.65 ± 0.14
H_2O-rich subduction-related components									
% added	0.580 ± 0.028	1.405 ± 0.078	1.565 ± 0.120	1.595 ± 0.035	1.530 ± 0.085	0.995 ± 0.035	0.865 ± 0.078	1.590 ± 0.071	-
Cl	17917 ± 429	14257 ± 568	11653 ± 1043	14015 ± 492	11792 ± 485	9998 ± 283	14046 ± 1021	17366 ± 1068	-
Rb	232 ± 48	89 ± 16	59 ± 9	46 ± 15	66 ± 7	59 ± 11	190 ± 5	90 ± 24	-
Ba	5690 ± 345	3352 ± 341	1727 ± 284	1815 ± 377	2322 ± 57	2143 ± 52	4318 ± 1331	1510 ± 351	-
U	4.8 ± 4.0	2.4 ± 0.8	-0.2 ± 0.0	1.3 ± 0.3	1.9 ± 0.5	0.9 ± 0.7	6.0 ± 0.1	2.8 ± 0.2	-
Th	10.2 ± 0.4	3.0 ± 0.2	1.3 ± 3.2	2.7 ± 1.6	4.4 ± 0.3	4.5 ± 0.3	11.7 ± 0.3	9.1 ± 3.5	-
K	141205 ± 5838	87349 ± 612	52080 ± 637	64329 ± 9319	69075 ± 431	52016 ± 268	85488 ± 4487	80822 ± 5882	-
Nb	- -	- -	- -	- -	- -	- -	- -	- -	-
Ta	2.6 ± 1.3	-0.2 ± 0.5	-1.0 ± 0.1	-0.3 ± 0.4	-0.5 ± 0.2	-0.3 ± 0.0	0.1 ± 2.1	0.7 ± 0.9	-
La	173 ± 49	99 ± 9	54 ± 7	52 ± 10	57 ± 2	66 ± 7	148 ± 3	40 ± 10	-
Pb	90 ± 13	58 ± 1	41 ± 4	30 ± 7	55 ± 2	37 ± 1	67 ± 2	34 ± 9	-
Ce	382 ± 49	210 ± 30	117 ± 44	129 ± 33	148 ± 0	197 ± 8	386 ± 20	101 ± 20	-
H_2O wt%	59 ± 2	48 ± 2	54 ± 5	49 ± 2	52 ± 2	54 ± 2	49 ± 4	62 ± 4	-
Nd	143 ± 31	93 ± 42	68 ± 9	80 ± 9	75 ± 1	88 ± 6	178 ± 52	59 ± 17	-
P_2O_5 wt%	0.42 ± 0.85	1.80 ± 0.32	1.36 ± 0.49	1.40 ± 0.45	1.78 ± 0.05	1.55 ± 0.63	2.40 ± 0.26	0.44 ± 0.17	-
Sr	7028 ± 1107	6094 ± 194	4305 ± 830	4781 ± 931	6100 ± 291	5654 ± 8	11928 ± 580	6322 ± 742	-
Zr	712 ± 162	693 ± 37	537 ± 45	351 ± 105	366 ± 99	595 ± 14	1059 ± 215	316 ± 147	-
Sm	8 ± 13	5 ± 2	11 ± 9	17 ± 4	13 ± 3	30 ± 25	20 ± 14	5 ± 4	-
Na_2O wt%	20 ± 3	37 ± 2	35 ± 6	39 ± 1	36 ± 2	37 ± 1	34 ± 4	24 ± 4	-
Ti	- -	- -	- -	- -	- -	- -	- -	- -	-
Y	- -	- -	- -	- -	- -	- -	- -	- -	-
Yb	- -	- -	- -	- -	- -	- -	- -	- -	-

Table 4.1. Melt inclusion major element compositions shown are the averages based on analyses of 15-25 melt inclusions per cone. Errors represent ± 1 s.d. Parental melt compositions shown are the averages of Fo_{90} normalized trace element data. H_2O-rich rich components are shown as the average ± 1 sd of two fluids calculated for each cone, with the amount of fluid added indicated by "% added".

4.1.1. Primary melt compositions

The heterogeneity of MGVF primary melt compositions is illustrated by a primitive-mantle-normalized incompatible trace element diagram (Fig. 4.4). Most melts have enrichments in large ion lithophile (LIL) elements and depletions in Nb and Ta, a pattern typical of subduction-related magmas. Elements thought to be strongly partitioned into a fluid or hydrous melt during dehydration or melting of hydrothermally altered oceanic crust or subducted sediment (eg., Ba, Pb, Sr; Kessel et al., 2005) are variably enriched, suggesting variability in the degree of addition of slab-derived components to the mantle beneath the MGVF. Additionally, there are large variations in the degree of Nb and Ta depletion. The variations in Nb and Ta concentrations are large enough that they cannot be explained by variations in the degree of partial melting of one mantle source composition, which suggests the mantle beneath the MGVF is heterogeneous in composition (Luhr, 1997). Because Nb and Ta are elements that are generally thought not to be added to the mantle by subduction-related fluids (Pearce and Peate, 1995), melts with high Nb and Ta must tap a mantle source region that is less depleted, whereas melts with depletions in Nb and Ta (i.e., most arc magmas) tap mantle that has been variably depleted by previous melting events (Pearce and Peate, 1995).

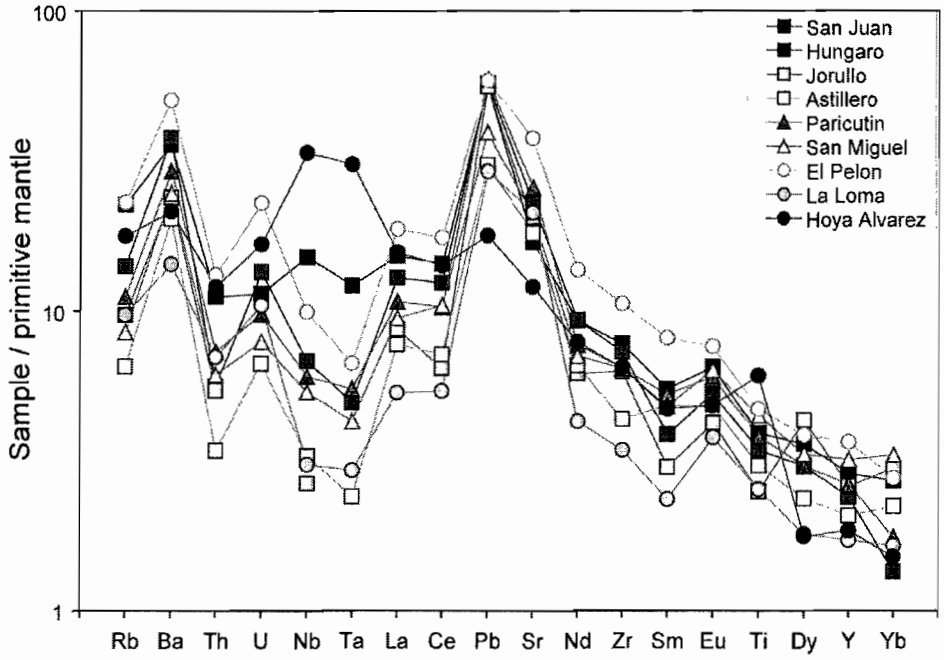

Figure 4.4. Trace elements in primary MGVF melts normalized to primitive mantle. Squares represent those volcanoes along or near the volcanic front, triangles are those between 50-100 km from the front and circles are those greater than 100 km from the front

Primary melt compositions are spatially heterogeneous, both along the arc and across the arc. For example, melts erupted along the volcanic front show variations in both extent of mantle depletion (e.g., Nb concentrations) and influence of subduction-related fluids over short spatial distances. Jorullo and Astillero (~80 km apart) erupted melts with low Nb and Ta concentrations and high concentrations of fluid mobile elements such as Ba and Pb (Fig. 4.4). However, the other arc-front volcanoes have much more variable melt compositions. Hungaro melts are less depleted in Nb and Ta than Jorullo and Astillero, and San Juan, which is located only 12 km from Hungaro, erupted melts that lack the depletion entirely (Fig. 4.4), suggesting these melts originated from less depleted mantle sources. Melts erupted far behind the front exhibit similar trench-parallel spatial variability; La Loma melts have large Nb-Ta depletions whereas

Hoya Alvarez (70 km away) erupted melts with high Nb and Ta. Additionally, Hoya Alvarez melts lack the slab-fluid signature seen at the other volcanoes, with the lowest Ba/La and Pb concentrations; together these data suggest that the mantle beneath Hoya Alvarez is less depleted and has not been significantly influenced by fluids or hydrous melts from the subducting slab.

The MGVF primary melts display no clear across-arc trends in major or trace element compositions. Figure 4.3 shows indicators of subduction-fluid addition and mantle depletion (Ba/La and Nb/La, respectively) across the arc. Primary melt ratios of Ba/La are low compared to other arc environments; melts in the Aleutian arc have Ba/La ratios of 20-50 ppm (Singer et al., 2007) and much higher values are recorded in Central America (up to 100 ppm; Eiler et al., 2005); however, values for the MGVF are elevated compared to average NMORB mantle (2.6 ppm; Stolper and Newman, 1994). There are no systematic trends in Ba/La with distance from the trench, as Ba/La remains high in melts erupted 350 km from the trench. The locality farthest from the trench, Hoya Alvarez, has much lower Ba/La (~14), suggesting a decrease in or lack of subduction derived fluids during melt generation. The mantle beneath the MGVF is variably depleted, as indicated by variable Nb/La ratios. Again, there is no systematic change in Nb/La values across the arc, with volcanoes both at the arc front (San Juan) and far behind the front (Hoya Alvarez) having erupted high Nb/La melts.

4.2. Across-arc variations in melt inclusion volatile concentrations

Melt inclusions at each volcano trapped variably degassed melts ($\leq$ 5.3 wt% H_2O and $\leq$ 1200 ppm CO_2, with CO_2 up to 6000 ppm at Hoya Alvarez), reflecting degassing

during ascent and eruption (Fig. 4.5). The maximum H_2O, CO_2, S (< 2100 ppm), and Cl (<1340 ppm) concentrations measured in melt inclusions across the MGVF are similar to volatile concentrations documented for other arc volcanoes in Central America (e.g., Roggensack et al., 1997; Wade et al., 2006; Benjamin et al., 2007), and are similar to concentrations found further to the east in Mexico in the Chichináutzin Volcanic Field (Cervantes and Wallace, 2003).

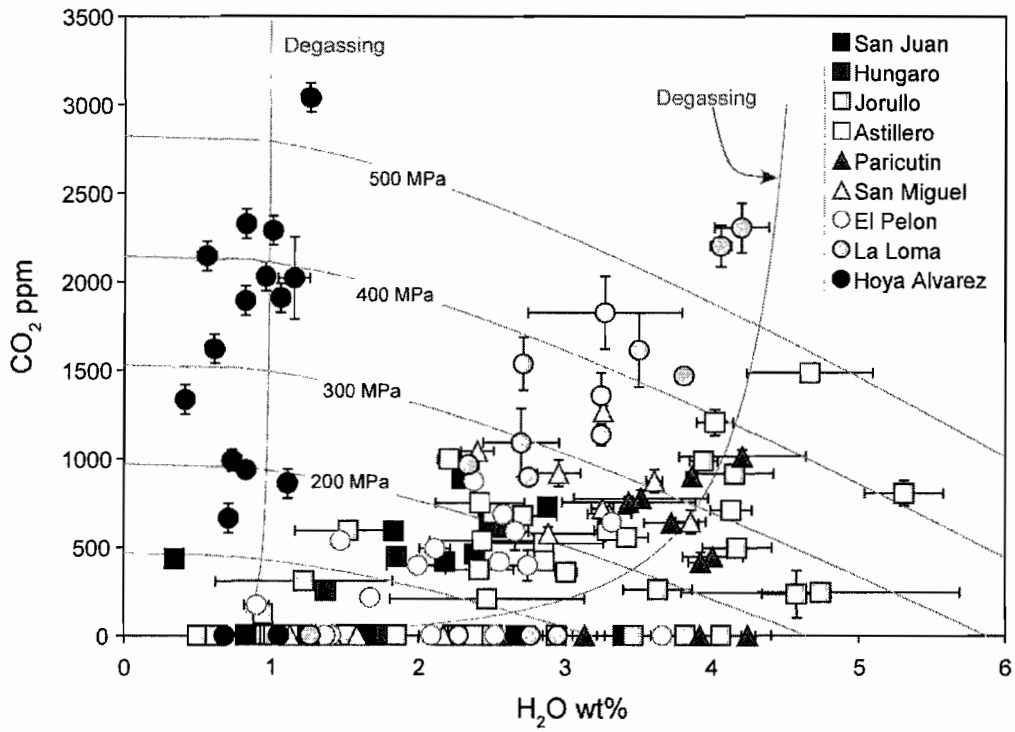

Figure 4.5. Melt inclusion CO_2 vs H_2O for all MGVF volcanoes. Melt inclusions trapped variably degassed melts, which generally fall along one of two degassing paths (calculated using VolatileCalc, Newman and Lowenstern, 2002). Most data scatter around the closed-system degassing path (1% exsolved vapor) for the high-H_2O, high-CO_2 inclusions. The Hoya Alvarez melts plot along a low-H_2O, high CO_2 closed-system degassing path (1% exsolved vapor).

The melt inclusions record variable degassing of H_2O and CO_2 during eruption, chlorine, which is highly soluble in basaltic melts (Webster et al., 1999), does not decrease with melt H_2O at individual cones, suggesting Cl was not degassed significantly

during eruption. Similarly MGVF melts exhibit little to no degassing of S during eruption. Due to the pressure dependent solubility of H_2O and CO_2 in basaltic melts, degassing during ascent and eruption decreases the concentration of these volatiles in the melt. Thus, the highest H_2O and CO_2 melts trapped within inclusions at a given volcano most closely represent the primary melt volatile contents (or at least provide a minimum value). However, due to the extreme insolubility of CO_2, melt inclusions likely never trap melts with primary CO_2 values (Wallace, 2005). Similarly, we assume that the highest S and Cl concentrations measured are closest to primary melt concentrations, although these data show less variability than H_2O and CO_2. We present here the maximum H_2O, Cl, and S concentrations (recalculated for melts in equilibrium with Fo_{90}, if necessary) at each locality across the arc.

4.2.1. Primary magma volatile contents across the arc

Maximum H_2O, Cl, and S concentrations in the primary magmas remain high (3-5.3 wt% H_2O, 700-1350 ppm Cl, 1500-2000 ppm S) for large distances (~150 km) across the arc, with the exception of Hoya Alvarez and San Juan (Fig. 4.6). The persistence of high volatile contents for great distances across the arc is surprising given the young age of the subducting Cocos plate. The relatively hot temperatures in the downgoing slab should cause most hydrous minerals to undergo dehydration reactions beneath the forearc region (based on the phase diagrams of Kerrick and Connolly, 2001). Furthermore, low concentrations of B measured in MGVF volcanic rocks led Hochstaedter et al. (1996) to suggest that H_2O concentrations in MGVF magmas must be low. The persistently high volatile contents of MGVF primary magmas differ from previous across-arc studies. In

Guatemala, measured H_2O values are variable but highest (< 6 wt%) in the volcanic front, but decrease rapidly (within < 80 km) to values of ~ 2 wt% behind the front (Walker et al., 2003). An across-arc study of the Kamchatka arc showed melt H_2O contents remain nearly constant but moderate (~2-2.5 wt%) across the arc (Portnyagin et al., 2007).

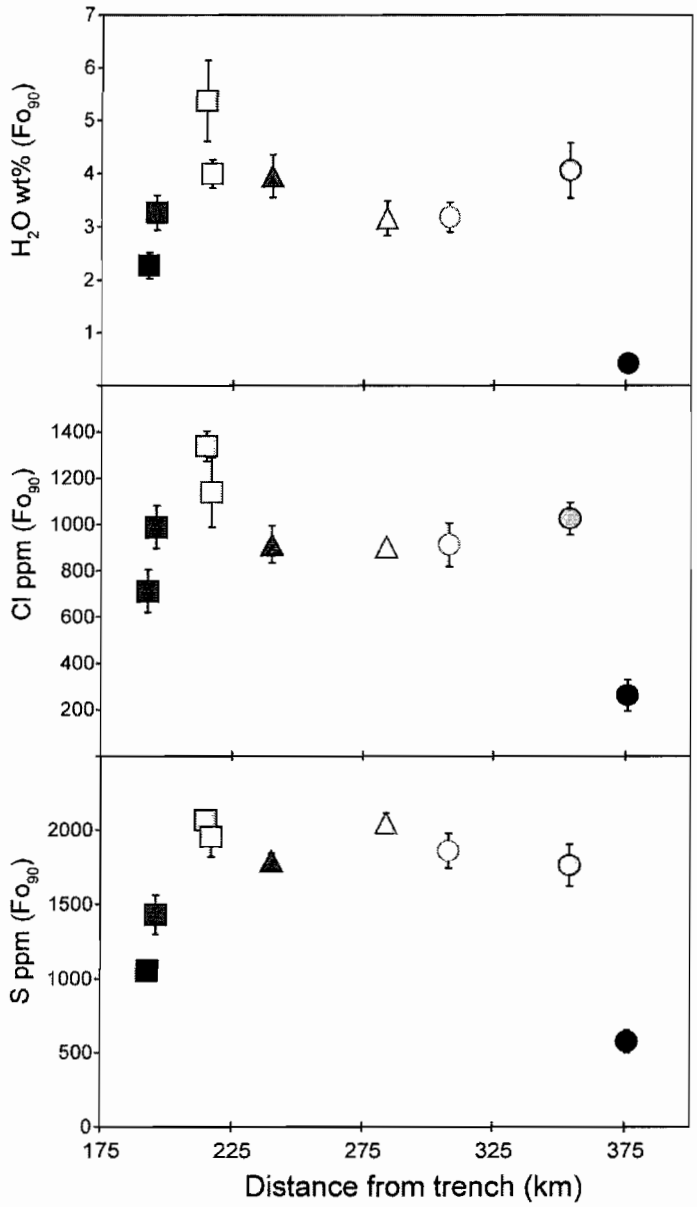

Figure 4.6. Primary melt maximum volatile contents vs. distance from the trench. In general, maximum H_2O, Cl, and S remain high for large distances (<150 km) behind the volcanic front. Symbols as in Figure 4.5.

Interestingly, the ratios of maximum Cl to H_2O and S to H_2O are constant across the arc, suggesting that the compositions of the H_2O-rich component transferred from the slab to the mantle wedge is relatively constant beneath the arc (Fig. 4.7). The Cl/H_2O ratio corresponds to a salinity of ~ 4 wt%, which is slightly higher than the salinity of seawater (~3 wt%). The strong correlations of Cl/H_2O and S/H_2O across the MGVF lends added support to our use of the maximum melt H_2O contents measured at each volcano; although H_2O degassed during ascent and eruption, the maximum melt inclusion H_2O values we measured must be very close to the primary melt H_2O concentrations in order for this ratio to be constant. Furthermore, the constant ratios of these volatile elements throughout the MGVF suggests that there is a phase or phases in the mantle or subducting material that is controlling their concentration in the subduction component added to the mantle wedge.

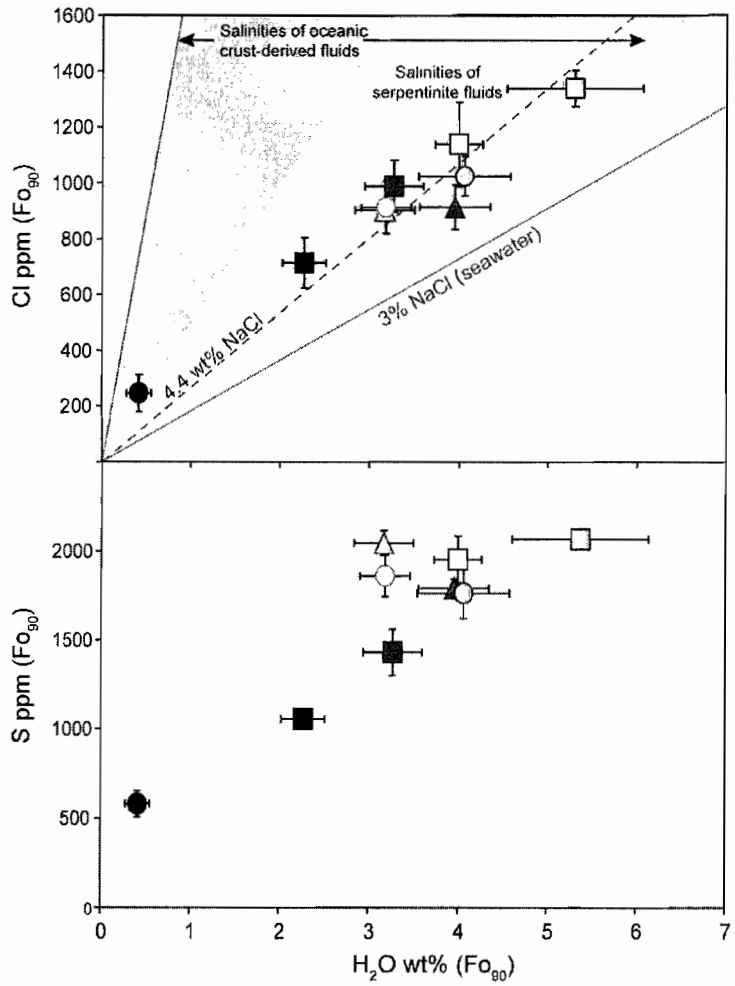

Figure 4.7. Covariations in maximum primary melt volatile contents, symbols as in Fig. 4.5. (a) Cl vs H_2O. The data fall along a line of constant salinity (4.4 wt % NaCl; after Kent et al., 2002). Also shown are the ranges of salinities for typical serpentinite-derived fluids (gray field; Scambelluri et al., 2004), oceanic crust-derived fluids (Philippot et al., 1998), and seawater. (b) S vs H_2O. The linear relationship of the data suggests a constant ratio of S/H_2O, and therefore also S/Cl, for the H_2O-rich subduction-derived components added to the mantle wedge beneath the arc.

4.2.2. Extrapolation of H_2O for the larger MGVF

Our study sampled nine of the nearly 1000 cinder cones in the MGVF (Hasenaka and Carmichael, 1985). In order to assess broader patterns in H_2O, we used correlations between H_2O and trace elements in our melt inclusion data to estimate H_2O contents for cinder cones with published geochemical data in the surrounding MGVF. WE also

applied our calibrated relationship between H2O and incompatible trace elements to data from cinder cones to the east in the Zitácuaro-Valle de Bravo (ZVB) and Chichinaútzin Volcanic Field (CVF). We found that ratios of fluid mobile trace elements (Ba, Sr) to other incompatible elements (Nb, La, Ti, Rb) in the MGVF melt inclusions correlate strongly with melt inclusion H_2O contents (Fig. 4.8). Using the linear regressions for these correlations, we calculated H_2O contents for other cinder cones in the MGVF, ZVB, and CVF where trace element data had been previously published. We filtered the available data to include only compositions similar to those in our study; thus we limited the data to basalt and basaltic andesite compositions. Because some datasets did not have reliable Nb data that particular correlation was not always used.

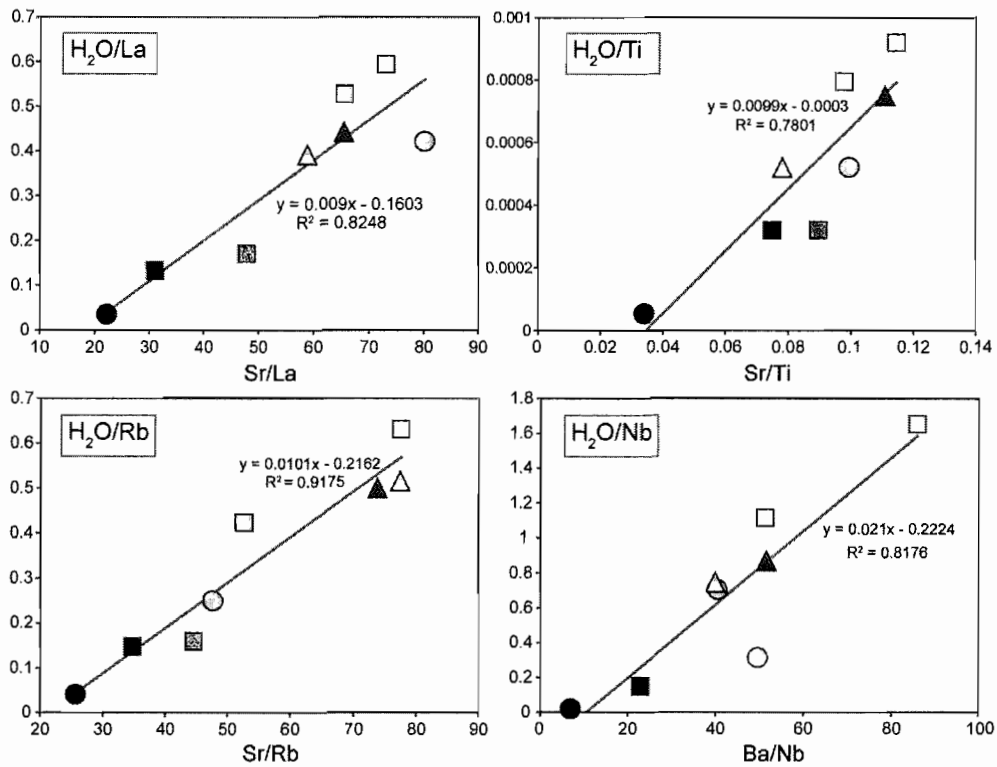

Figure 4.8. Relationships between H_2O and trace element ratios for MGVF melt inclusions. The equations for the linear regressions fit to the data were used to calculate H_2O for melts throughout the MGVF and central Mexico with existing trace element data.

We assessed the error in our calibration by back-calculating H_2O contents of the MGVF melt inclusions that were used fin the calibration and also by calculating H_2O for CVF melt inclusions of known H_2O that were not used in the calibration (Cervantes and Wallace, 2003), and for the cinder cones in our study using bulk tephra LA ICP-MS trace element data. We found that our calibration reproduced the measured H_2O values in the MGVF and CVF with a root mean squared error (RMSE) of ±1.2 wt% H_2O (see Appendix G).

We calculated H_2O contents for 284 localities in the MGVF and the central TMVB. Using these calculated H_2O concentrations we produced a map of magmatic H_2O across central Mexico (Fig. 4.9). The spatial pattern of H_2O concentrations throughout the MGVF supports the trends seen in our melt inclusion data. The map shows variable but high H_2O (< 7 wt%) along the volcanic front and a striking broad region of moderately high H_2O (> ~3 wt%) continuing over a large region behind the volcanic front. Far behind the front (~175 km) the data display an abrupt decrease in melt H_2O with a large region of consistently low H_2O contents (<1.5 wt%). In order to test how representative the nine cones sampled for this study are of the broader field, we plotted our measured melt inclusion maximum H_2O contents and the calculated H_2O contents against distance from the trench (Fig. 4.10). While there is significant scatter in the MGVF calculated H_2O contents, our nine samples seem to be broadly representative of the MGVF basaltic melts and their spatial variability in H_2O across the arc.

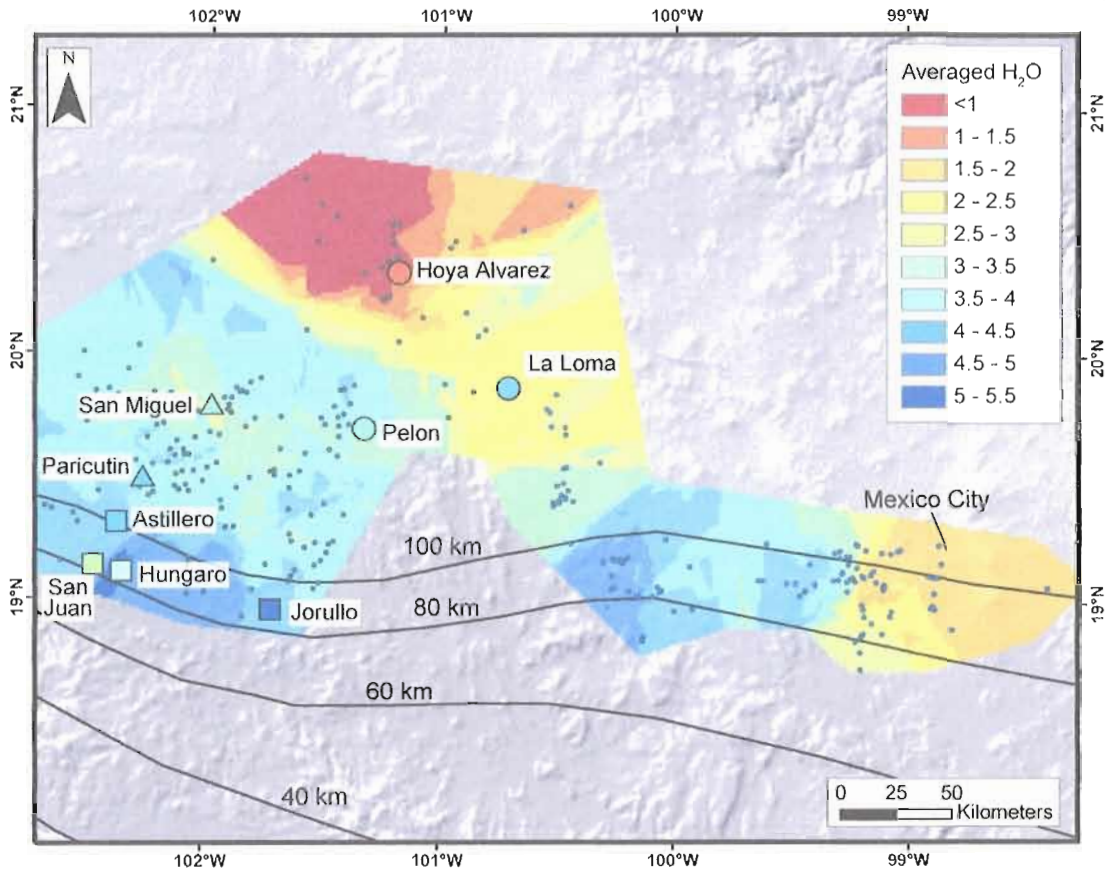

Figure 4.9. Map of interpolated H_2O contents across central Mexico. The small dots represent the locations of cones for which H_2O contents were estimated based on published trace element data (Hasenaka and Carmichael, 1985; Blatter et al., 2001; Siebert and Carrasco-Nuñez, 2002; Cervantes and Wallace, 2003; Siebe et al., 2004; Schaaf et al., 2005; Gomez-Tueña et al., 2007). The map was produced using the kriging function in ArcMap, where H_2O contents were interpolated (using the two nearest datapoints) over a defined space, and the H_2O concentrations were then contoured, grading from warms colors (low-H_2O) to cool colors (high-H_2O). Also shown are the locations of the MGVF samples from this study, whose data points are also color coded according to the legend, and contours to the top of the subducting slab (Pardo and Suárez, 1995). Some small scale features in the interpolated values (e.g., along the NW side) are artifacts of the kriging procedure.

The spatial variations in melt H_2O to the east of the MGVF are very different. In the ZVB to the east, our modeled data show high H_2O in the volcanic front (~ 6 wt%), but unlike the MGVF, the melt H_2O contents decrease with distance behind the front. Further to the east in the CVF the data are more sparse, but the volcanic front magmas

generally contain high H_2O contents. In addition to the error assessment described above for our H_2O estimates, we also assessed the validity of our H_2O calibration in the ZVB by comparison with melt H_2O contents estimated from experimental phase equilibria. For the ZVB, both the pattern of decreasing H_2O with distance from the trench and the high H_2O in the volcanic front volcanoes agree with the H_2O estimates of Blatter et al. (2007) based on phase equilibria.

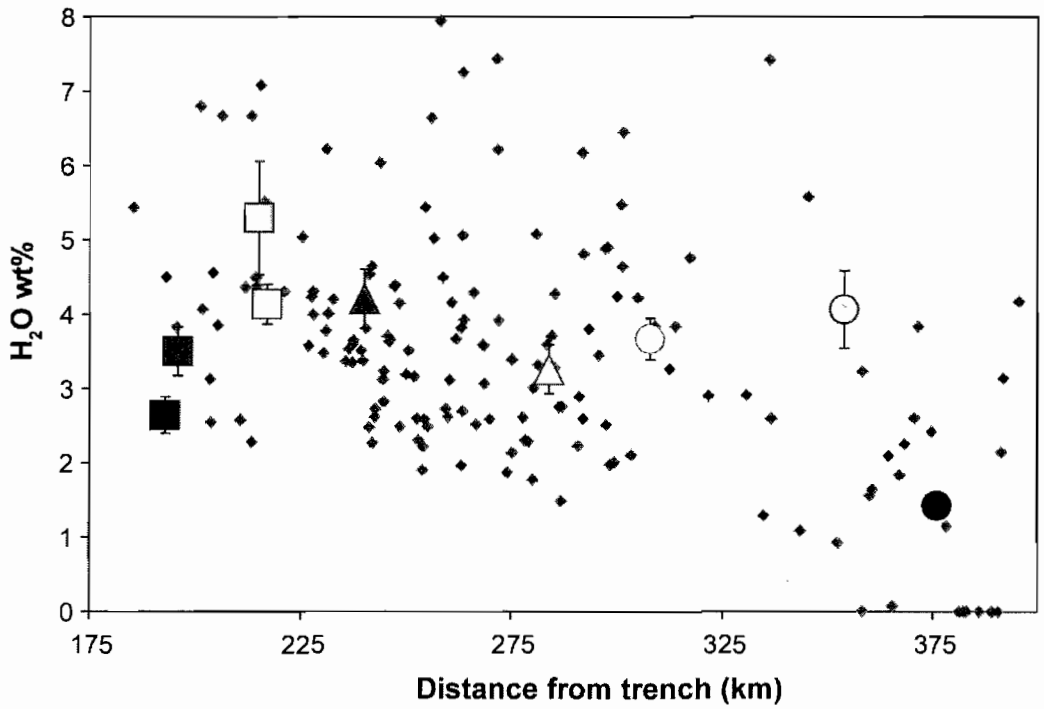

Figure 4.10. Melt H_2O contents vs. distance from the trench for all MGVF localities. The small grey diamonds are the localities in the MGVF where H_2O contents were calculated using the correlations shown in Fig. 4.8. Also shown are the maximum melt inclusion H_2O concentrations measured in this study (symbols as in Fig. 4.5).

There are two abrupt transitions from H_2O-rich magmas to H_2O-poor (< 1.5 wt%) magmas; one in the far northeast of the MGVF and one in the CVF (Fig. 4.9). The compositions of the magmas in these regions appear to be distinct as well. Because high field strength element (HFSE) concentrations are indicative of the mantle source region,

we plotted TiO_2 concentrations on the spatial map of H_2O (Fig. 4.11). The magmas in the low-H_2O regions contain higher concentrations of TiO_2 overall than do magmas in the high-H_2O regions. This suggests that either the magmas in these regions originate from a more enriched mantle source region or that they represent a different degree of partial melting of the source region. However, the melt inclusion trace element data from Hoya Alvarez, located in the far NE of the MGVF, suggest that the mantle source for this volcano is OIB-like, with enrichments in Nb-Ta. Thus, we conclude that the low H_2O regions most likely correlate with enriched, OIB-like, mantle source regions. The implications for this correlation will be discussed further in section 6.1.

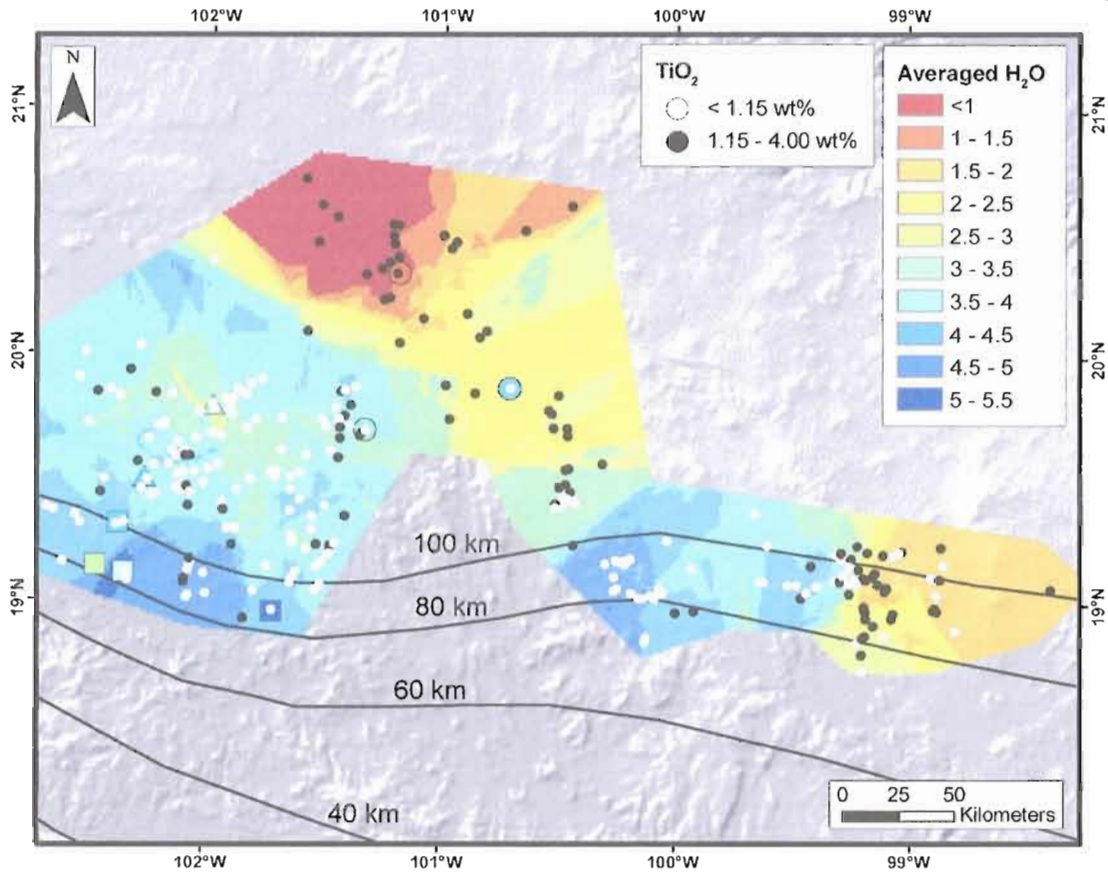

Figure 4.11. Map of H_2O for central Mexico with melt TiO_2 concentrations. Same spatial map as in Figure 4.8, but the localities have been subdivided based on melt TiO_2 content. Melts with $TiO_2 < 1.15$ wt% are represented by white circles, and melts with TiO_2 1.15-4 wt% are represented by black circles. There is a strong spatial relationship between regions of low melt H_2O contents and high TiO_2.

4.3. Oxygen isotopes in olivine

Oxygen isotope values of olivine phenocrysts across the MGVF are variable, but are high overall with respect to typical mantle values. MGVF olivine have $\delta^{18}O_{olivine}$ values that range from 5.5 ± 0.2‰ to 6.0 ± 0.1‰ (Fig. 4.12), which are high in comparison to olivine in mantle peridotites (5.2 ± 0.2‰; Mattey et al., 1994; Eiler, 2001). Arc basalts contain variable $\delta^{18}O_{olivine}$; most arc basalts around the world have $\delta^{18}O_{olivine}$ = 5.2 ± 0.2‰ (Eiler et al., 2000a; Eiler, 2001), but both lower values (4.6-4.9 ‰,

Nicaragua; Eiler et al., 2005) and higher values (<5.7‰ in Central America; Eiler et al., 2005; ≤ 7.2‰, Klyuchevskoy volcano in Kamchatka; Dorendorf et al., 2000; Auer et al., in review) have been measured. The high $\delta^{18}O_{olivine}$ values found in the MGVF are higher than in olivine from most arc basalts from Central America. Interestingly, the MGVF data extend the observed trend of increasing $\delta^{18}O_{olivine}$ values from the south (Costa Rica) to the north (Guatemala; Eiler et al., 2005) in Central America. There are no correlations between MGVF $\delta^{18}O_{olivine}$ values and distance from the trench, nor do the oxygen isotope values correlate with trace element ratios.

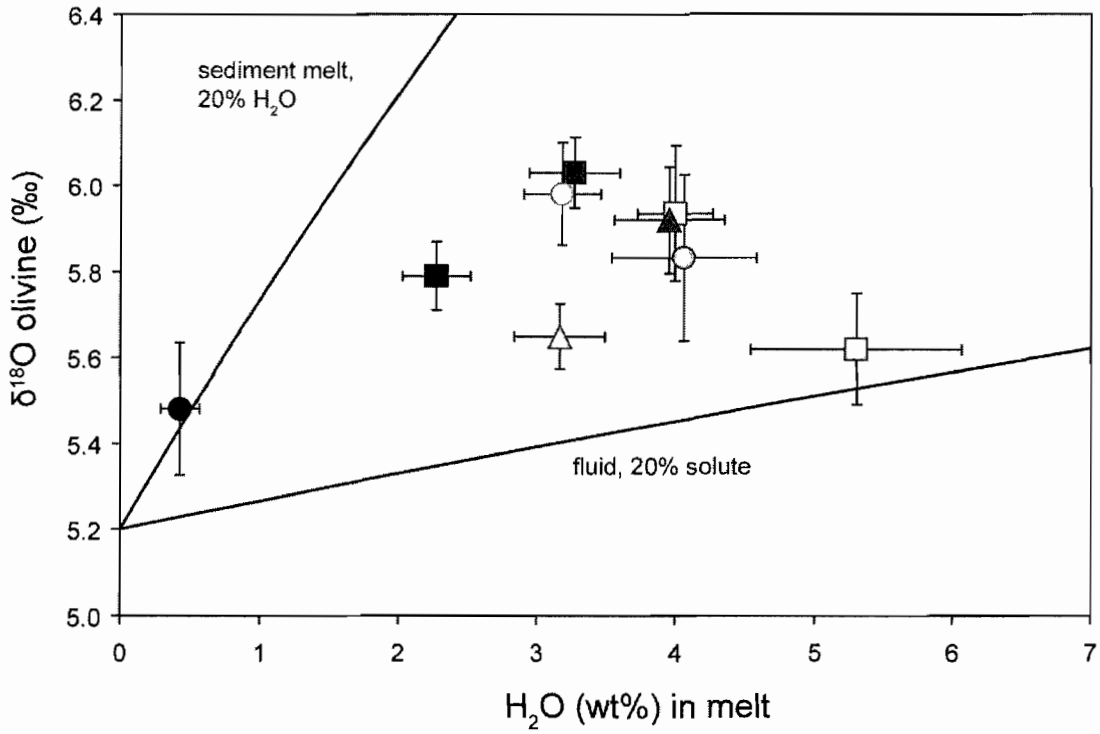

Figure 4.12. Oxygen isotope ratios for MGVF olivine and primary melt H_2O contents (symbols as in Fig. 4.5). Also shown are lines representing mixing between a peridotite mantle and a slab-derived fluid with 20% solute and between peridotite and a sediment melt with 20% H_2O. The MGVF melts plot between these two mixing lines, suggesting that the H_2O-rich component added to the wedge is a mixture of slab- and sediment-derived fluids/melts.

5. Mantle heterogeneity in the MGVF

Variability in the Nb and Ta depletion of the MGVF lavas suggests that the magmas tapped a heterogeneous mantle source at depth. In order to assess the mantle source region compositions beneath the MGVF, we plotted ratios of conservative elements, which are elements that are probably not transferred to the mantle wedge by subduction-related fluids (Pearce and Peate, 1995). Figure 4.13 illustrates the heterogeneity in the mantle source compositions and suggests that most magmas originate from mantle that is less depleted, to varying degrees, than the depleted MORB mantle (DMM) source for NMORB. The magma compositions range from highly enriched (Hoya Alvarez) to near-NMORB values (Jorullo), and unlike studies of other arc volcanoes (e.g., Kamchatka), none of the MGVF magmas originate from a depleted MORB mantle (DMM) source. For most localities the primary melts show no indication of garnet in the mantle source (i.e., low Yb, Y). However, melts at Hoya Alvarez display lower Yb and Y (Fig. 4.14). The high Dy/Yb and Y/Yb values at Hoya Alvarez (Fig. 4.14) suggest that garnet was present in the source region, as elevated Dy/Yb ratios have been shown to be indicators of the presence of garnet during mantle melting (Davidson et al., 2007) and Yb fractionates more strongly into garnet than Y. The presence of garnet creates an added complexity in modeling partial melting, as discussed below.

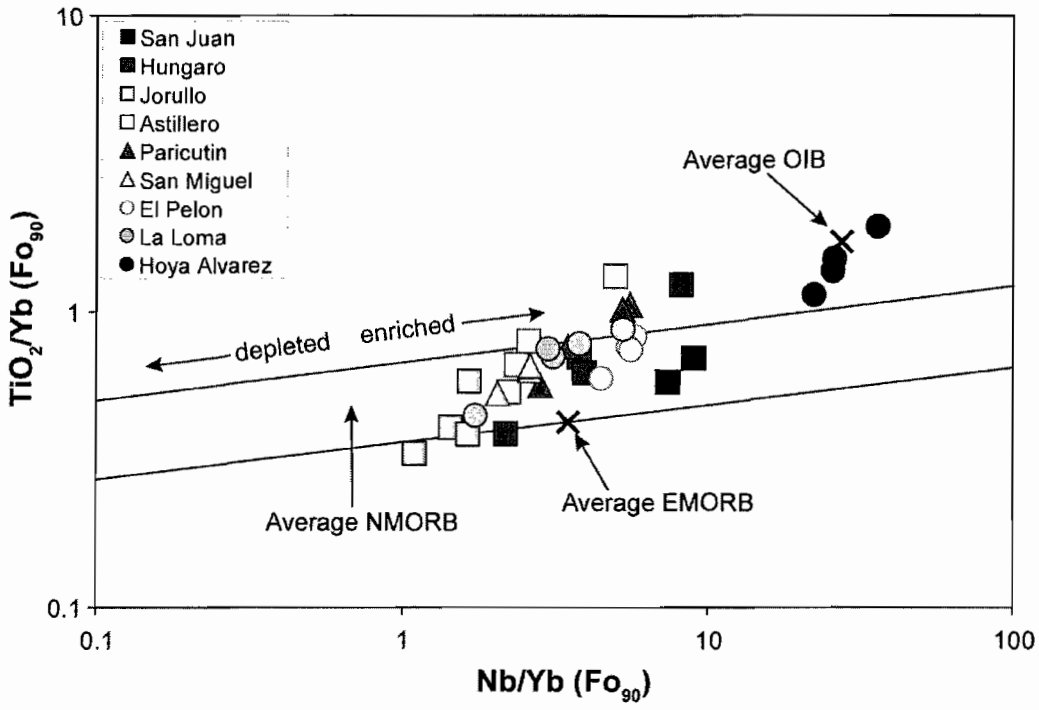

Figure 4.13. Primary melt TiO_2/Yb vs Nb/Yb (following Pearce and Peate, 1995). MGVF primary melts all have Nb/Yb concentrations higher than typical NMORB values, suggesting they originated from a more enriched mantle source region. Average NMORB and EMORB from Sun and McDonough (1989) and average OIB from Sun (1980).

The presence of garnet in the source region for an OIB-type magma is at odds with the results of work in western Mexico. Luhr (1997) suggested that OIB and calc-alkaline melts in western Mexico originated from different source regions, with OIB melts tapping spinel lherzolites (shallower melting) and calc-alkaline melts generated from garnet lherzolite (deeper melting). These conclusions were based, in part, on the high concentrations of Yb in the alkaline magmas, and low Yb in calc-alkaline samples. However, the MGVF magmas illustrate the opposite, with low Yb in the Hoya Alvarez magmas. To test whether or not the source for the calc-alkaline magmas contained garnet we calculated the Dy/Yb ratios of melts that would be generated by partial melting of a

garnet lherzolite and a spinel lherzolite to the Dy/Yb ratios in the MGVF magmas. We found that 10% partial melting of a lherzolite (EMORB in composition) with 3.7 wt% garnet produces melts with Dy/Yb = 3.4, which are much higher than the observed ratios for calc-alkaline MGVF magmas (~2). However, 10% partial melting of a spinel lherzolite produces melts with Dy/Yb = 2.2, suggesting that the calc-alkaline magmas of the MGVF originated from a spinel lherzolite, whereas the source for the Hoya Alvarez magmas contained garnet.

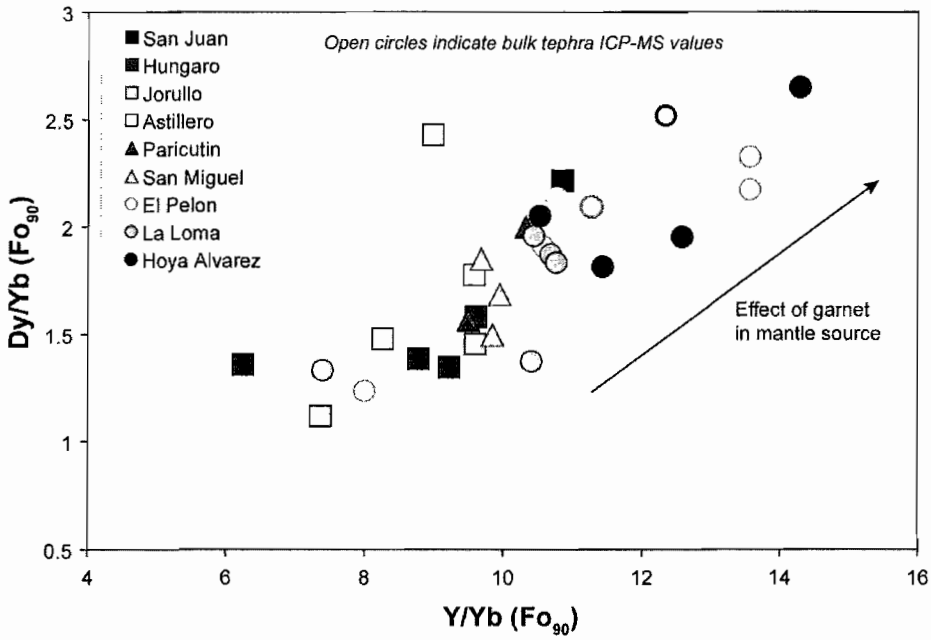

Figure 4.14. Primary melt Dy/Yb vs Y/Yb. Higher Dy/Yb and Y/Yb in Hoya Alvarez melt inclusions and bulk tephra suggest that the mantle source beneath this volcano contained residual garnet. Open circles represent bulk tephra ICP-MS analyses for El Pelon, La Loma, and Hoya Alvarez.

6. Modeling partial melting, mantle volatile contents, mantle compositions, and H_2O-rich subduction component compositions

The combination of primary melt compositions, volatile concentrations and oxygen isotope data allows us to calculate: 1) degrees of mantle melting (F) across the

arc, 2) mantle volatile concentrations, 3) mantle trace element compositions, and 4) compositions of H_2O-rich slab-derived components and their origin. We followed and expanded on the methods described in Kelley et al. (2006) to calculate F and mantle concentrations of H_2O and Cl. For calculations of mantle composition we assumed modal batch melting of a spinel lherzolite source with a mineralogy similar to that used by Eiler et al. (2000a, 2005).

6.1. Partial melting of the mantle

As shown above, the mantle beneath the MGVF appears to be less depleted than DMM and is spatially heterogeneous, and thus we have used ratios of conservative elements (Ti, Nb) to Y to determine the mantle source composition for each cone. Kelley et al. (2006) demonstrated that the ratio TiO_2/Y varies little during mantle melting at mid-ocean ridges, so variations in TiO_2/Y must reflect source composition variations. Our data show that TiO_2/Y and Nb/Y correlate positively, suggesting Nb/Y can also be used to calculate mantle compositions and degree of partial melting. In order to determine the composition of the mantle source regions, we used the ratios of TiO_2/Y and Nb/Y in our Fo_{90} melt inclusion compositions to calculate the mantle composition of each conservative element using the following equation:

$$C^{o}_{X} = \frac{(C_X/Y)_{sample}}{(C_X/Y)_{MORB}} \times C^{DMM}_{Ti} \qquad (1)$$

where $(C_X/Y)_{sample}$ is the concentration of the species (TiO_2, Nb)/Y from melt inclusion Fo_{90} compositions, $(C_X/Y)_{MORB}$ is the concentration of the species/Y in NMORB (TiO_2/Y = 0.047, Nb/Y = 0.094), and C^{DMM}_{X} is the concentration of each species in depleted

MORB mantle (TiO_2 = 0.133, Nb = 0.21; Salters and Stracke, 2004). Using these mantle source concentrations for TiO_2 and Nb we used the batch melting equation to calculate F, the fraction of melting:

$$F = \frac{(C^o_X/C^l_X) - D_X}{(1-D_X)} \quad (2)$$

where C^o_X is the concentration of species X (TiO_2, Nb) in the mantle source, C^l_X is the concentration of that species in the Fo_{90} melts, and D_X is the bulk distribution coefficient for the species during melting (D_{Ti} = 0.04, D_{Nb} = 0.003; Kelley et al., 2006).

The calculation for Hoya Alvarez, which has garnet in the mantle source region, was more complex. Garnet in the source region will deplete melts in Y, thus increasing TiO_2/Y, resulting in estimates of F that are too high. In order to account for this effect, we calculated TiO_2/Y for partial melting of a DMM mantle source that contained garnet. We used the same TiO_2 and Y values for the NMORB source region as Kelley et al., 2006 (e.g., Stolper and Newman, 1994), and we assumed that the NMORB lava is produced by 5% partial melting of the NMORB source. Using the batch melting equation, we then calculated the concentration of Y in an NMORB lava with garnet in the source region, using a higher value of D^Y (0.121, based on a 5x increase to approximate the effects of residual garnet; Stolper and Newman, 1994). This yields a lower concentration of Y in the NMORB lava (14.6 ppm), and thus the ratio of TiO_2/Y in the NMORB increases to 0.093. We did the same for Nb/Y in an NMORB from a garnet source (Nb/Y = 0.22), and then input these values for MORB in equation (1), and performed the calculation for the Hoya Alvarez melt composition. Accounting for garnet in the source results in much lower values of F (9%).

Figure 4.15 shows primary melt H_2O contents and the calculated degrees of partial melting for each volcano. The values of F are averages based on using TiO_2 and Nb in equation (2), and both models yielded similar results, with standard deviations for F of ~0.003-0.04. Based on these calculations, we conclude that most MGVF primitive magmas form by 16-24% partial melting, with lower melt fractions at Hoya Alvarez (9%). Overall, the calculated MGVF melt fractions overlap with the average values of F calculated for back-arc basins (8-18%; Kelley et al., 2006), and are slightly higher than extents of melting for the Kamchatka arc (5-14%; Portnyagin et al., 2007).

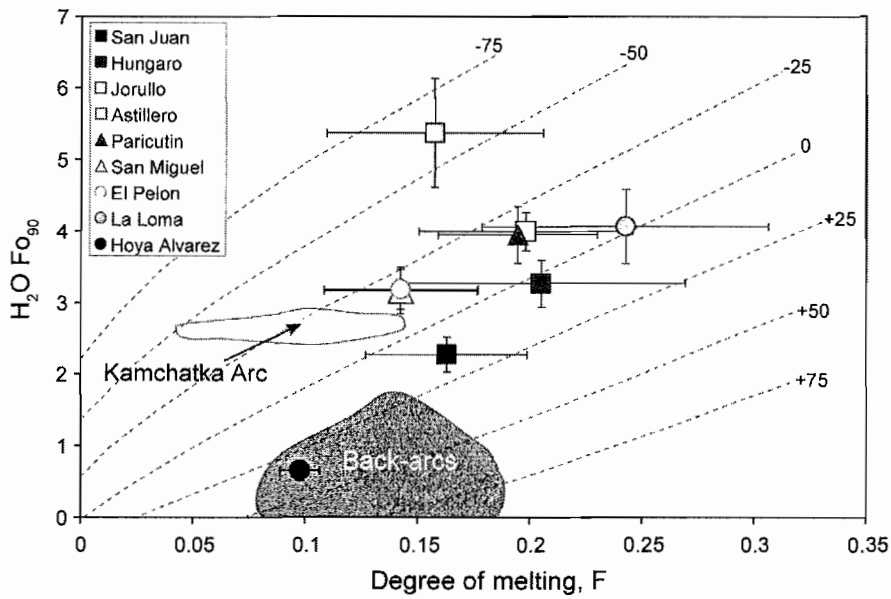

Figure 4.15. Primary melt H_2O and the calculated degree of partial melting of the mantle, F. Also shown are dotted curves that represent temperature deviations from the dry peridotite solidus (Portnyagin et al., 2007). Gray fields are data from the Kamchatka Arc (Portnyagin et al., 2007) and for back-arc basins (Kelley et al., 2006).

These partial melting calculations, combined with primary melt compositions and volatile contents, allow us to differentiate between flux melting and decompression melting of the mantle wedge beneath the MGVF. The high volatile contents, elevated

concentrations of fluid mobile elements, depletions in Nb and Ta, and moderate values of F for most of the MGVF cones suggest that fluid-flux melting generated these magmas. However Hoya Alvarez, which is the farthest locality from the trench, originated from a much less depleted (OIB-like) source region and has low concentrations of fluid mobile elements, suggesting that the mantle had not experienced previous episodes of hydration or melting. The low degree of partial melting calculated for Hoya Alvarez is uncommon for fluid-fluxed mantle melting, but is similar to other back-arc basin melts (Fig. 4.15). Furthermore, the high-CO_2, low-H_2O melts of Hoya Alvarez are similar to melts associated with decompression melting (e.g., Galunggung; Sisson and Bronto, 1998). Together these data suggest that low-H_2O, alkalic magmas erupted at Hoya Alvarez and other localities far behind the front (Fig. 4.9), result from decompression melting of the mantle, with only minor involvement of slab-derived fluids.

6.2. Using melt fractions to calculate mantle volatile contents

Using the Fo_{90} across-arc H_2O and Cl contents and the melt fractions from equation (2), we calculated mantle volatile concentrations across the MGVF using the batch melting equation:

$$C^{o}_{V} = C^{l}_{V} [F(1- D_V) + D_V]$$

where C^{o}_{V} is the concentration of H_2O or Cl in the mantle source, C^{l}_{V} is the concentration of the volatile species in the Fo_{90} melt, F is the melt fraction from equation (2), and D_V is the bulk distribution coefficient of the volatile species (assumed to be 0.012 for both H_2O and Cl, from Kelley et al., 2006).

Mantle H_2O concentrations in the MGVF remain high across most of the arc, between 0.4-1.0 wt%, with lower values at Hoya Alvarez (0.2 wt%; Fig. 4.16). Mantle Cl contents range from 130-250 ppm, but again have lower values for Hoya Alvarez (60 ppm). These mantle H_2O concentrations, with the exception of Hoya Alvarez, are higher than mantle source H_2O concentrations calculated for the Kamchatka arc (0.13-0.4 wt%; Portnyagin, 2007) and are significantly higher than NMORB mantle (70-450 ppm; Sobolev and Chaussidon, 1996; Workman and Hart, 2005) and OIB sources (< 900 ppm; Dixon et al., 1997; Wallace et al., 1998). Similarly, the MGVF mantle Cl concentrations are higher than primitive mantle (0.4-17 ppm; McDonough and Sun, 1995). Like the primary melt volatile concentrations, there is no trend in across-arc mantle H_2O or Cl, and the persistence of high mantle volatile contents requires influence of subduction-related H_2O-rich component(s) beneath a large portion of the arc.

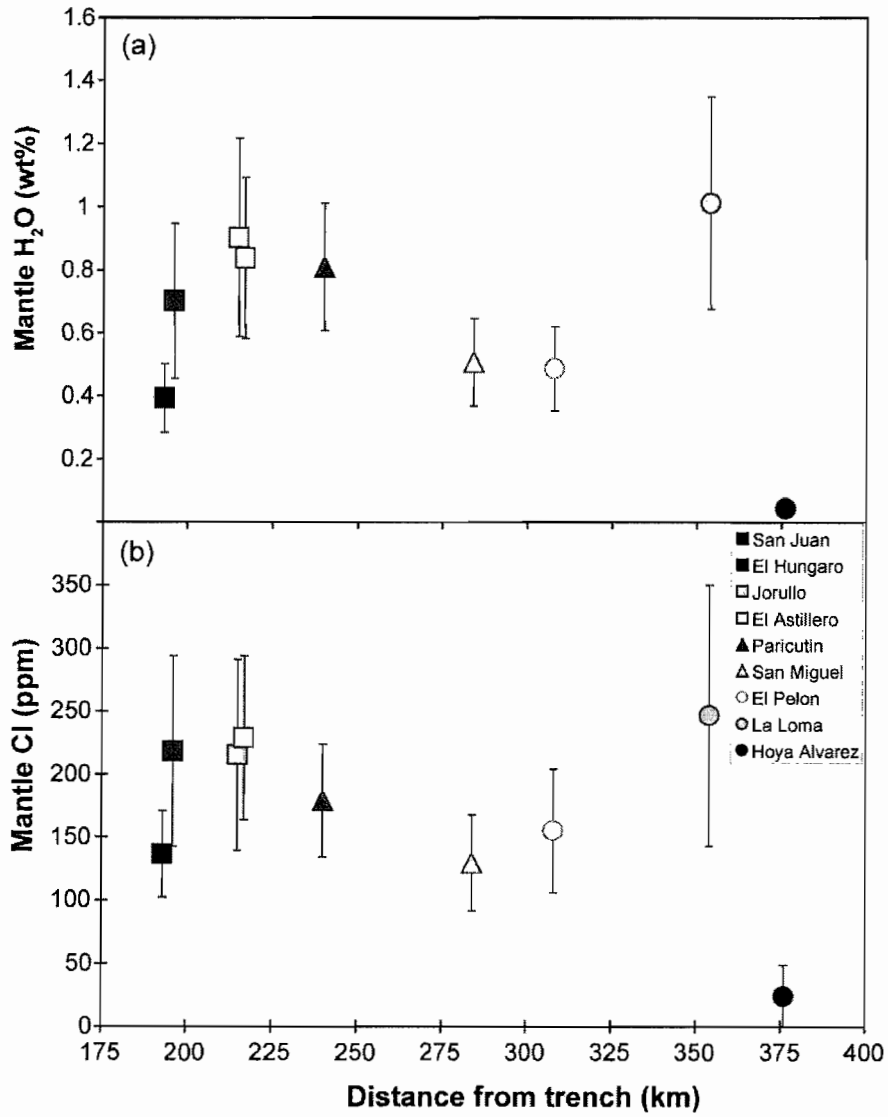

Figure 4.16. Mantle volatiles across the MGVF. (a) Mantle H_2O remains elevated (0.4-1 wt%) across much of the arc, with the exception of low H_2O at Hoya Alvarez. (b) Mantle Cl shows a similar pattern to across-arc H_2O, with elevated values (100-250 ppm) across most of the arc.

6.3. Modeling mantle source compositions

In order to estimate the compositions of the H_2O-rich components added to the mantle beneath the MGVF, we first need to calculate the composition(s) of the unmodified MGVF mantle for a more complete set of trace elements than were used in

the model described in the previous section. Due to the large variability in HFSE across the arc, applying one mantle composition to all volcanoes seems unreasonable. Thus, we used the concentrations of elements assumed not to be contributed by subduction-related components (Nb, Ta, Ti, and to a lesser extent, Y and Yb) to calculate a mantle source composition for each volcano. The procedure for calculating F included calculations of mantle concentrations of Ti and Nb (section 5.2.1.); however, the bulk trace element composition of the mantle source region for each volcano is needed in order to assess the amount of subduction components added to the mantle wedge.

In previous studies where the compositions of slab-derived components were calculated, the mantle beneath the volcanic arc has been assumed to be compositionally similar to NMORB mantle or DMM (e.g., Stolper and Newman, 1994; Eiler et al., 2005; Portnyagin et al., 2007). However, as all MGVF primary magmas have Nb/Y concentrations higher than NMORB compositions (Fig. 4.13), an EMORB mantle source composition is more applicable. Since there is not a standard EMORB source mantle composition available, we created an EMORB source by back-calculating from an average EMORB lava composition (Sun and McDonough, 1989). For these calculations we used the mantle mineralogy and melting stoichiometry of Baker and Stolper (1994), the mineral-melt D values from Eiler et al. (2005), and we calculated bulk D values for each element. However, the variations in HFSE in MGVF primary melts suggest a heterogeneous mantle source, indicating that the EMORB source itself was variably depleted by previous partial melting and melt extraction (Wallace and Carmichael, 1999). We accounted for this variability by assuming that the average EMORB composition represents 2-15% partial melting of the mantle. Using this variation in degree of melting,

we can construct more-depleted EMORB sources to more enriched EMORB sources, respectively.

Once the EMORB source compositions were calculated, we used the value of F determined for each cone in section 4.2 to partially melt each source, producing EMORB lavas with the same degree of partial melting as each of our primary melts. Plots of the incompatible element compositions of the primary magma for each cone with the melt compositions from partial melting of the EMORB sources enable assessment of the fit between the MGVF melts and the generated EMORB melts (see Fig. 4.17). Following the assumption that melt Nb, Ta, Ti, and other HFSE are contributed from the mantle source alone, the mantle source region that produced a melt that best fits these elements was assumed to be the source for that particular volcano (Fig. 4.17). Again, the only exception to this method is Hoya Alvarez, whose melt composition is so enriched that it is compositionally more similar to an OIB than an EMORB. However, when comparing the Hoya Alvarez primary melts to an OIB source region, none of the trace elements appear to be enriched above mantle values, and thus, no addition of subduction-related H_2O-rich components is necessary in the mantle beneath this volcano.

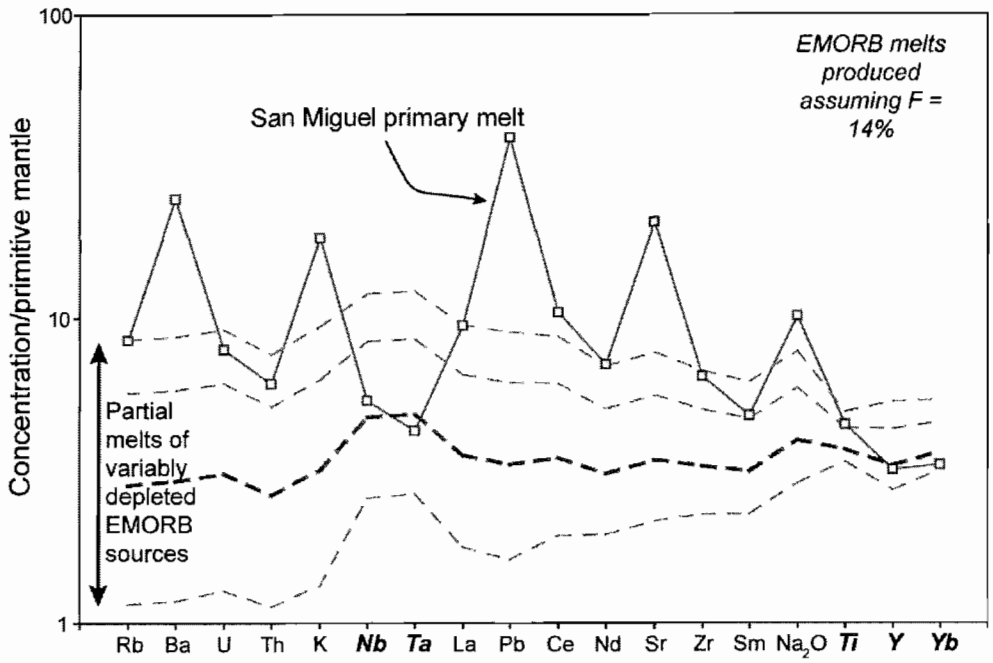

Figure 4.17. The trace element concentrations of a primary MGVF melt (San Miguel; solid line) and the compositions of four EMORB lavas generated by 14% partial melting of four variably depleted EMORB mantle source regions (dashed lines). The EMORB lava represented by the thick dashed line best fits the San Miguel primary melt in terms of Nb, Ta, Y and Yb concentrations. Thus, the mantle source composition that generated this lava is assumed to be the mantle source for the San Miguel melts.

6.4. Subduction component trace element and volatile compositions

Trace element concentrations that are high compared to the model melt from an EMORB source region are assumed to be contributed by an H_2O-rich subduction-related component (fluid and/or melt). We used the following derivation of the mass balance equation (following Stolper and Newman, 1994) to calculate the contributions and compositions of the H_2O-rich component:

$$C_V = [C_L*[F+(D*(1-F))] - (1-y)*C_O]/y$$

where C_V= concentration of a species in the "fluid", C_L = concentration of a species in the primary melt, F = degree of partial melting, D = bulk distribution coefficient, y =

fraction of "fluid" added, and C_O = concentration in the EMORB source. We calculated the concentration of incompatible trace elements as well as Cl, Na_2O, K_2O, and P_2O_5 in the H_2O-rich component. In this equation there are two unknowns, C_V and y, which were solved for by adding two constraints to this equation. First, we stipulated that the concentrations of all trace and minor elements in oxide form plus H_2O must sum to 100%. Thus the sum of all oxides subtracted from 100% gives us the concentration of H_2O in the fluid. Importantly, in this study we have the added constraint of knowing the concentration of H_2O in the primary melts. Thus we re-arranged equation (3) to solve for C_L, where C_L is the concentration of H_2O in the primary melts, and C_V is the concentration in the fluid based on input values of y. Using these constraints we then input our known parameters (C_L, F, D, and C_O) and iteratively varied y until the results yielded the concentration of H_2O we measured in the primary melts.

The H_2O-rich component compositions for the MGVF are very similar to slab fluids calculated for the Marianas (Stolper and Newman, 1994) and for Central America (Eiler et al., 2005) (Fig. 4.18). Similarly, the amount of fluid added to the mantle wedge (<2 wt%) is similar to other studies (2.5-3 wt%, Eiler et al., 2005). The concentrations of H_2O in all components are very similar, however, the MGVF subduction-related components overall have higher concentrations of some LILE and fluid mobile elements, such as Ba, K, and Pb. There are distinct trends in the concentrations of some trace elements in these H_2O-rich components across the arc. With the exception of La Loma, K, Cl, and H_2O in the fluid decrease with distance from the volcanic front, and with the exception of San Juan, P_2O_5 and Na_2O decrease behind the front. Conversely, concentrations of Th in the H_2O-rich component are much higher far behind the front.

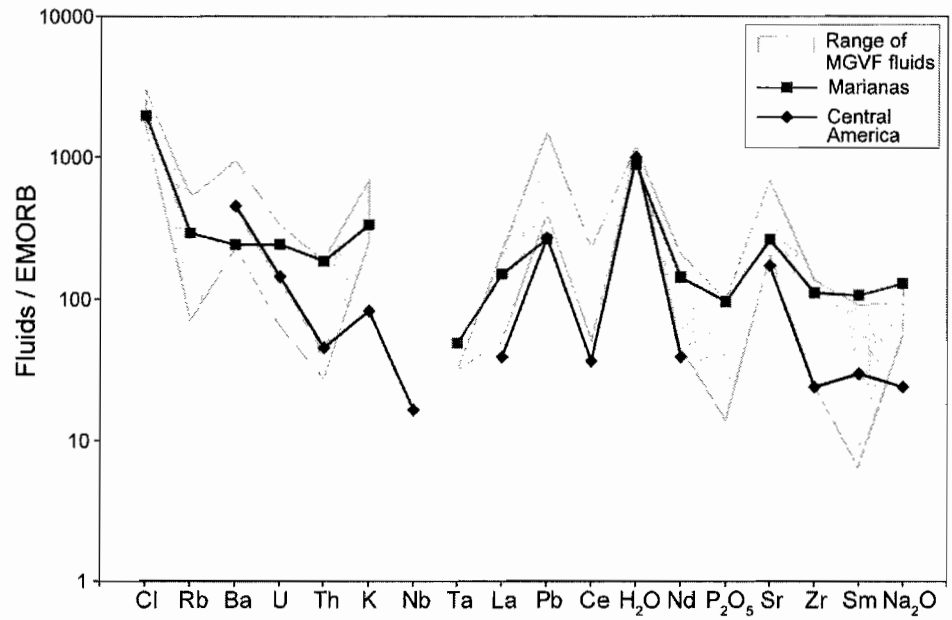

Figure 4.18. Volatile and trace element compositions of calculated MGVF H_2O-rich subduction components (gray field) and subduction components calculated for the Marianas (Stolper and Newman, 1994) and Central America (Eiler et al., 2005). All concentrations are normalized to an EMORB mantle source composition.

7. Origin of H_2O-rich subduction components

The high magmatic volatile concentrations for large distances across the MGVF are puzzling; in "hot" subduction zones such as Mexico, devolatilization of hydrous phases in the subducting slab should occur mainly beneath the forearc (Kerrick and Connolly, 2001; Schmidt and Poli, 2004). Here we use a combination of $\delta^{18}O_{olivine}$ values, trace element data, estimated compositions of H_2O-rich components, and 2-D thermal models of the subducted slab and mantle wedge to develop hypotheses regarding the origin of subduction-related H_2O-rich components beneath the MGVF.

7.1. Isotopic and trace element evidence for sediment involvement

The high $\delta^{18}O_{olivine}$ values found in the MGVF provide an important constraint on the origin of subduction fluids, in that they require that the fluid added to the mantle wedge is isotopically heavy. Olivine in the mantle wedge typically has $\delta^{18}O$ values of 5.2 ± 0.2‰ (Eiler et al., 2000a), significantly lower than the values measured in the MGVF (5.5-6‰). Fluids or hydrous melts derived from subducted sediment and altered oceanic crust would have higher $\delta^{18}O$ than mantle values. The uppermost altered oceanic crust has $\delta^{18}O$ values of 7-15‰ (Alt et al., 1986; Staudigel et al., 1995) and hemipelagic and pelagic sediments are even more isotopically heavy (15-25‰; Kolodny and Epstein, 1976; Arthur et al., 1983; Alt and Shanks, 2006). Fractional crystallization of primitive magma can increase $\delta^{18}O$ values, but the MGVF melts are compositionally primitive, with only minor fractionation of olivine (in most cases) having occurred. Fractionation of olivine would increase the $\delta^{18}O$ value of the melt by ~ 0.1‰ (Zheng, 1993); such a small increase does not explain the high MGVF values. Although crustal assimilation can enrich $\delta^{18}O$ in arc magmas (Harmon and Hoefs, 1995), the primitive nature and small volumes of the MGVF melts suggest that this process is unlikely.

The high $\delta^{18}O_{olivine}$ values in the MGVF most likely originated from components with heavy $\delta^{18}O$ values such as altered oceanic crust and/or subducted sediment. The contribution of slab and sediment (or both) to the H_2O-rich components can be assessed by modeling the $\delta^{18}O$ values of slab- and sediment-derived fluids or melts during progressive partial melting of the mantle wedge. Assuming a slab-derived fluid with a $\delta^{18}O$ value of 9‰ and a sediment-derived melt with a $\delta^{18}O$ value of 15‰, these components were mixed with variable proportions of mantle material, which has a $\delta^{18}O$

value of 5.2‰. This calculation involves multi-step modeling of the melt or fluid composition as it ascends (following Grove et al., 2006). As hydrous melts ascend, the temperature increases due to the inverted thermal gradient in the mantle wedge, resulting in further melting of the surrounding peridotite. As the melt ascends to regions of higher temperature and lower pressure, continued melting of peridotite causes a decrease in the H_2O concentration of the hydrous melt due to dilution. The slab and sediment H_2O-rich component curves produced from this model are shown in Figure 4.12, plotted with the MGVF $\delta^{18}O_{olivine}$ values and melt H_2O contents. These curves suggest that the high $\delta^{18}O_{olivine}$ values in the MGVF require components of both slab-derived fluid (from altered oceanic crust) and sediment-derived melts, with higher $\delta^{18}O_{olivine}$ values corresponding to greater input of sediment components. Some magmas, such as Jorullo, plot closer to the slab-derived H_2O-rich component curve, suggesting that sediment-derived melts were not important in melt generation.

The isotopically heavy $\delta^{18}O_{olivine}$ values in the MGVF suggest that the subduction component added to the mantle wedge is composed of a combination of slab-derived fluid and sediment-derived melts. Sediment-derived melts have been shown to be an important component in many arcs worldwide (e.g., Marianas, Kamchatka, Aleutians; Plank, 2005; Portnyagin et al., 2007). Although the sediment package subducted at the Middle America trench is relatively thin compared to other subduction zones (~170 m; Plank and Langmuir, 1998; Lagatta, 2003), recent work in central Mexico has suggested a role for sediments in generating the melt compositions erupted in the Zitácuaro-Valle de Bravo volcanic field. Isotope ratios (Pb, Sr, Nd) suggest that melts result from mixing of subducted sediment and fluids or melts from altered oceanic crust (Gómez-Tueña et

al., 2007). Furthermore, this interpretation is supported by the results of Eiler et al. (2005) in Central America, where $\delta^{18}O_{olivine}$ values up to 5.7‰ were measured. They concluded that to produce these values, which are slightly lower than the MGVF (up to 6‰), the subduction-derived component must be a partial melt of sediment.

Although Mexico is a low sediment flux margin, there are correlations between arc magma Th/Rb and subducting sediment Th/Rb (Fig. 4.19). Plotting MGVF primary magma Th/Rb and an average Th/Rb ratio for the entire package of subducting sediment (Lagatta, 2003) shows that most MGVF magmas fall close to a 1:1 line, suggesting that sediment melts are required to impart Th to the magmas (e.g., Johnson and Plank, 1999). The low concentrations of Th/Rb in the subducting oceanic crustal slab and slab-derived fluids (< 0.01, slab data from Verma, 2000) suggest that the elevated Th/Rb seen in MGVF magmas is not inherited from a slab source.

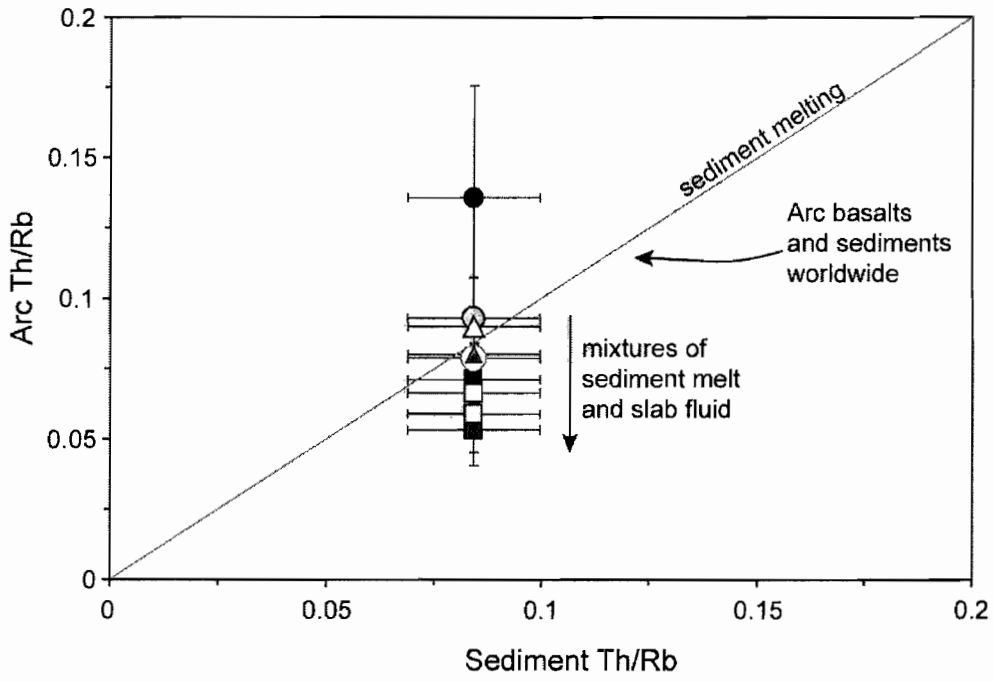

Figure 4.19. Comparison of MGVF Th/Rb and average sediment Th/Rb (data from Lagatta, 2003). MGVF Th/Rb and sediment Th/Rb fall on or near a 1:1 line, suggesting sediment influence on arc Th concentrations (e.g., Johnson and Plank, 1999). Also shown is a field for the correlation between arc basalts and subducting sediments worldwide (gray field, Johnson and Plank, 1999). Because the oceanic crustal slab contributes virtually no Th, mixtures of sediment melt and slab fluid shift some magma Th/Rb values to lower values than the 1:1 line.

Furthermore, if sediment-derived melts were important in flux melting of the MGVF mantle wedge, the compositions of the H_2O-rich components added to the mantle should reflect this influence. Figure 4.20 shows Ba and Th vs La concentrations in the calculated subduction components for each volcano. Using bulk compositions of sediments overlying the Cocos Plate (Lagatta, 2003), an average altered oceanic crust composition (Staudigel et al., 1996), the composition of the subducting Cocos plate (Verma, 2000), and fluid-eclogite D-values (Kessel et al., 2005), we calculated hypothetical slab and sediment fluid and melt compositions. Comparison of the MGVF fluids and slab and sediment components suggest that, similar to our interpretation based

on $\delta^{18}O$ values, the material added to the MGVF mantle wedge is a combination of slab and sediment components. Again, some of the modeled H_2O-rich components plot near the slab fluid field, suggesting less involvement of sediments. However, compositions with elevated Ba, Th, and La suggest higher amounts of sediment melt involvement.

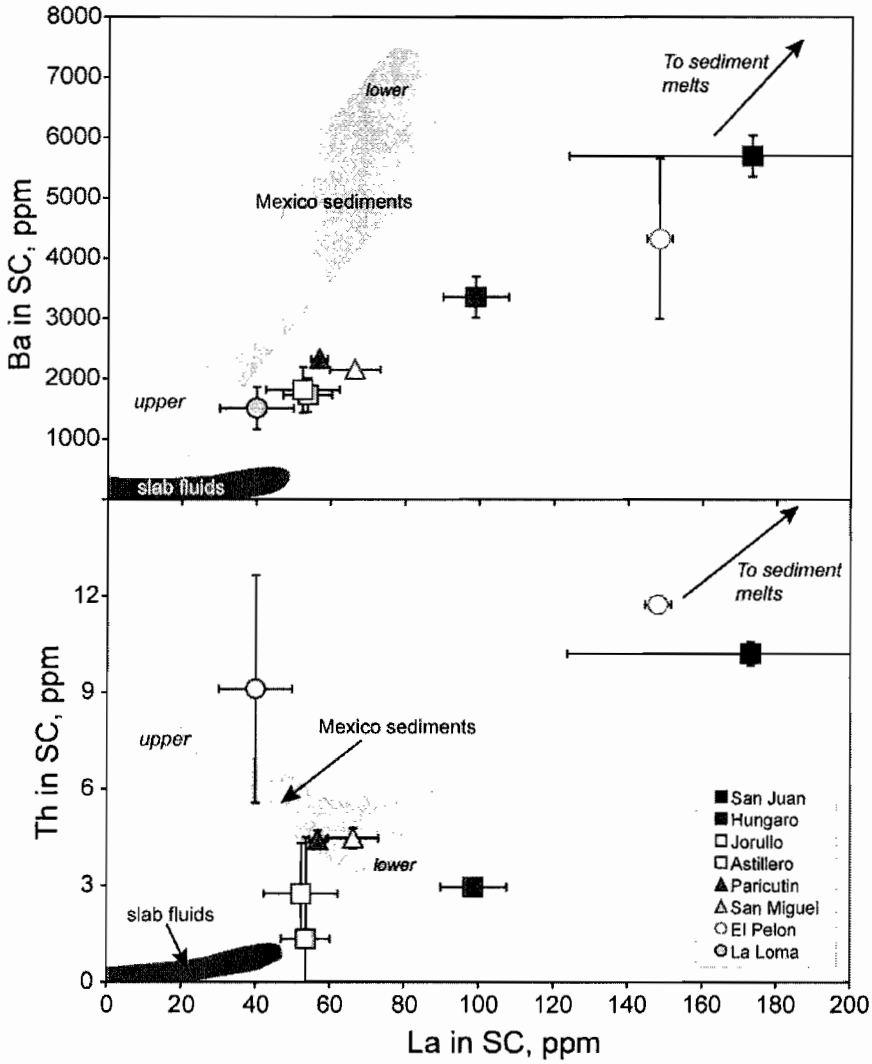

Figure 4.20. Concentrations of Ba and Th vs La in the subduction components (SC) of MGVF melts and hypothetical fluid/melt sources. Compositions of slab fluids were calculated using oceanic crust compositions (Staudigel et al., and Verma, 2003) and fluid-solid D values at 4 GPa and 700-800°C from Kessel et al. (2005). Mexico sediment compositions are from Lagatta (2003), and sediment melt compositions were calculated using fluid-solid D values at 4 GPa and 900-1000°C from Kessel et al. (2005).

Mixing of slab fluids and sediment melts is also evident in plots of Rb and Pb vs La, but the relationship fails for Sr, Zr, and Ce. The subduction-derived components appear to have higher Sr, Zr, and Ce than can be produced by slab or sediment fluids or melts. However, as seen in Figure 4.18, the subduction components calculated for the MGVF are very similar to those calculated for other arcs worldwide. Calculated subduction components contain high levels of Sr (3000-15000 ppm; Stolper and Newman, 1994; Eiler et al., 2002; Portnyagin et al., 2007), but dehydration or melting of oceanic crust or sediment cannot produce such high concentrations. One possibility is that the presence of components such as Cl, F, and S in subduction-derived fluids changes the partitioning of elements compared to experimental systems lacking these elements. Another possibility is that mineral breakdown reactions in natural systems are more complex than in equilibrium experiments, leading to greater concentrations of some elements in the fluid phase (John et al., 2008).

7.2. Devolatilization of subducted material

While trace elements and oxygen isotopes provide information on the origin of the H_2O-rich subduction components, understanding the thermal structure of the subduction zone is vital to assessing the stability of hydrous phases in the subducted slab. Two-dimensional thermal models of the MGVF subduction zone were created to estimate the pressure-temperature (P-T) conditions of hydrous phase breakdown reactions in the slab and melt generation in the mantle wedge. However, the history of subduction beneath the MGVF is complex, and this requires consideration when assessing production of subduction-related fluids and melts. Currently the subducting slab dips at

an angle of approximately 30° (Pardo and Suarez, 1995) beneath the MGVF, but there is evidence that the slab geometry has changed in the past 3 Ma. To the east of the MGVF, the Cocos slab trenchward of Mexico City is currently flat to shallowly dipping, and it is likely that >3 Ma the slab geometry in the MGVF resembled that of central Mexico today. Between 3 Ma and the present, the Cocos plate geometry steepened, recorded by the progressive trenchward movement of MGVF volcanism in the last 2 Ma (Fig. 4.21; Hasenaka and Carmichael, 1985; Ban et al, 1992). This transformation in slab geometry creates an added complexity in the assessment of slab dehydration over time. To account for this, we used two different 2-D thermal models to look at production of subduction-related H_2O-rich components: 1) using the current slab geometry, and 2) using the inferred flat slab geometry of 3 Ma.

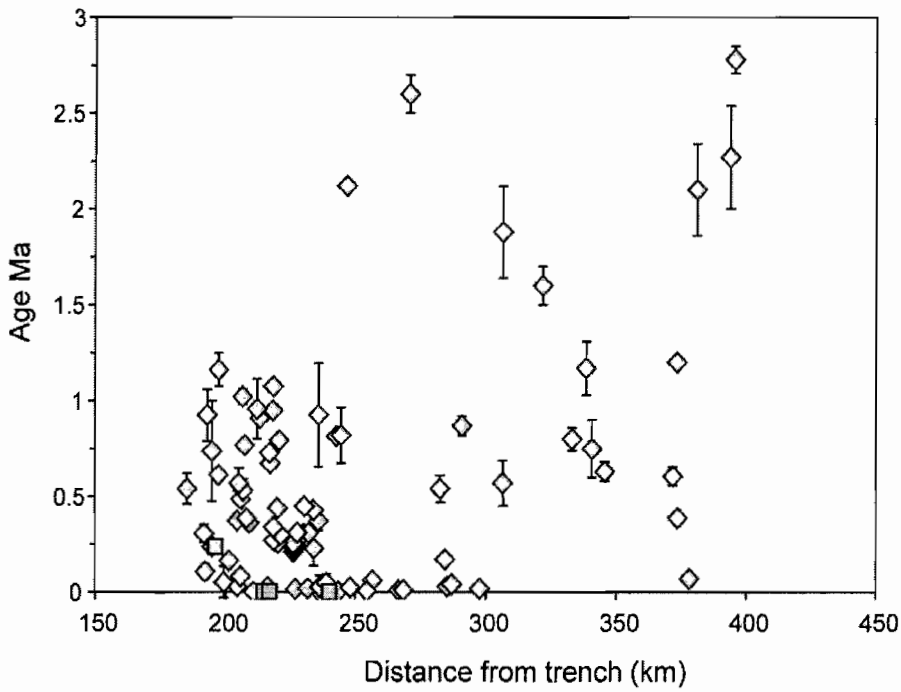

Figure 4.21. Age of MGVF volcanic rocks vs distance from the trench. Ages based on C^{14}, K-Ar, and ^{40}Ar-^{39}Ar dates (Hasenaka and Carmichael, 1985; Ban et al., 1992; Suter et al., 2001; Ownby et al., 2007; S. Ownby and R. Lange, unpublished data). Squares indicate four volcanoes sampled in this study: Hungaro, Paricutin, Jorullo, and Astillero.

7.2.1. Dehydration of subducted material – present-day slab configuration

Figure 4.22 shows the thermal model of the MGVF subduction zone with the location of the MGVF volcanoes at the surface. Using this thermal structure, magmas erupted in the volcanic front region of the MGVF correspond to oceanic slab depths of ~80 km and maximum slab surface temperatures (SST) of ~ 600°C. Melts erupted far behind the front (350 km from the trench) correspond to slab depths of ~170 km and maximum SSTs of ~850°C.

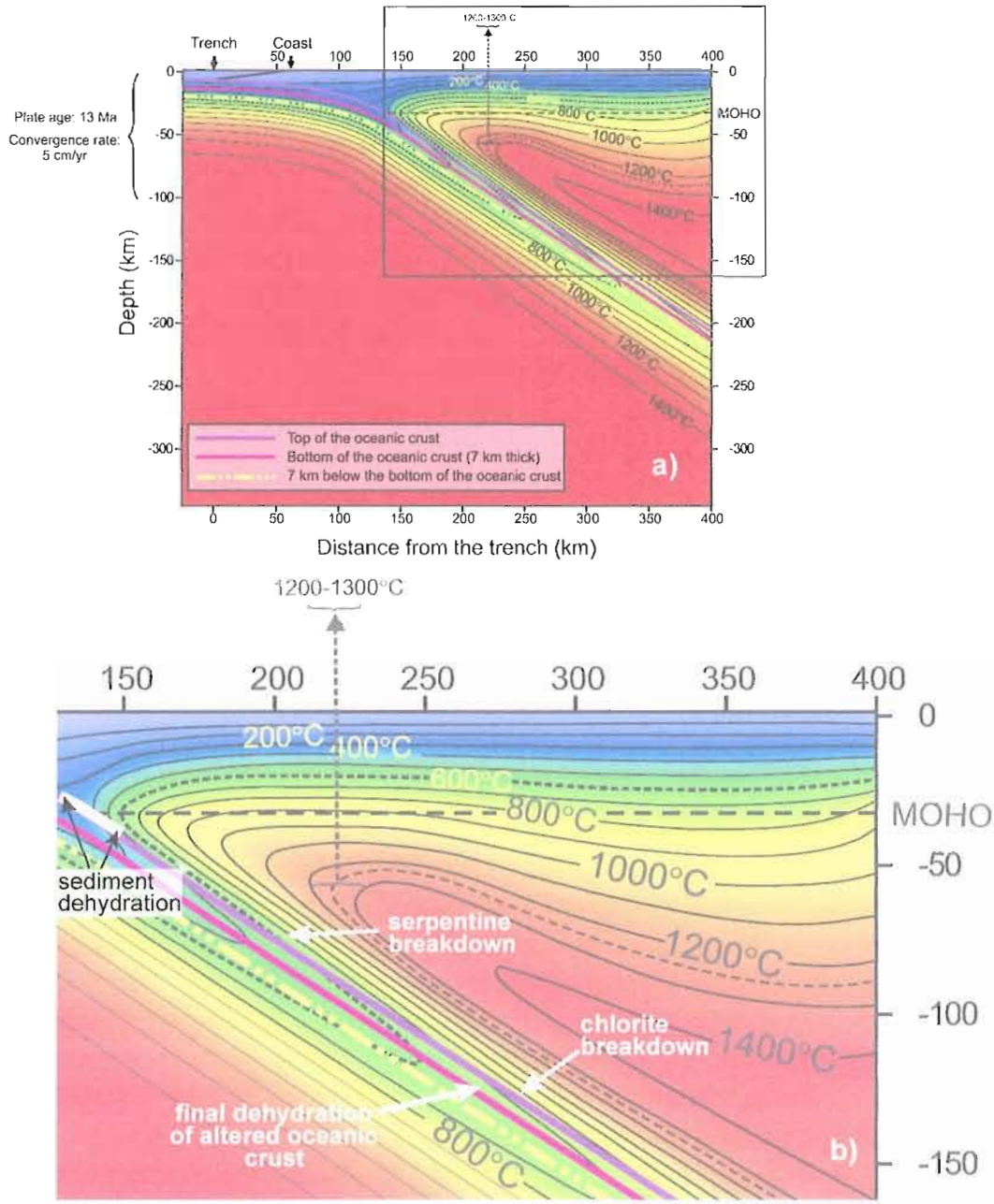

Figure 4.22. (a) 2-D thermal model of the subduction zone beneath the MGVF from the Middle America Trench to 400 km from the trench. (b) thermal structure beneath the MGVF, showing regions where sediment should dehydrate (tan region; based on sediment phase diagram of Rupke et al., 2004), and upper stability limits of serpentine (from Rupke et al, 2004) and chlorite (Grove et al., 2006), and the depth at which dehydration of the entire section of altered oceanic crust should be complete (Rupke et al., 2004).

Using the P-T conditions predicted for the subducting oceanic crust and phase diagrams for altered oceanic crust, serpentinized mantle, and sediments (Schmidt and Poli, 2004; Rupke et al., 2004; Grove et al., 2006), we can predict where H_2O should be released from the subducted slab. Based on the P-T conditions in the slab and mantle wedge and P-T diagrams for fluid release from subducted sediment (Rupke, 2004), the subducted sediment should release most of its H_2O beneath the forearc region (Fig. 4.22b). The altered oceanic crust should dewater beneath the forearc and extend to the region beneath the volcanic front. Based on the temperatures at the top of the slab, dehydration of the uppermost oceanic crust should cease at depths of ~ 100 km, but limited fluid release from deeper in the subducted crust would continue to greater depths. Our model results are supported by correlations between the cessation of earthquakes in subducting slabs and the transition from blueschist (hydrous) facies to eclogite (dry) facies (Abers et al., 2006). Applying this theory to the subducting Cocos plate, which lacks seismic events at depths > 70 km (Pardo and Suarez, 1995), suggests that beyond the volcanic front in Mexico the oceanic slab is eclogitic and is no longer dewatering. While these results are not surprising given the young age (and thus higher temperature) of the subducting slab, they do conflict with the presence of volatile-rich, high- $\delta^{18}O$ melts erupted over large distances from the volcanic front across the MGVF.

Although the subducted sediment and altered oceanic crust largely dehydrate beneath the forearc and volcanic front, there are several ways that an H_2O-rich, high $\delta^{18}O$ fluid could consequently partially melt the mantle further down-dip beneath the MGVF. First, several studies of subduction zones have suggested that hydration and subsequent

down-dragging of the overlying mantle wedge through corner flow may aid in transferring hydrous phases to greater depths. Recent experimental work by Grove et al. (2006) suggest that fluids released at lower pressures and temperatures into the mantle wedge could react with the peridotite to form hydrous phases, such as chlorite, that are subsequently coupled with the plate and dragged to higher pressures and temperatures. Their experimental work also shows that a high pressure chlorite phase in mantle peridotite may be stable up to 3.2 GPa and could contain up to 12 wt% H_2O (Grove et al., 2006). The stability of this phase to great depths could expand the P-T zone over which hydrous melts are produced during subduction. A similar model has been recently invoked to explain homogenous fluid compositions in an arc, where fluids released by the subducting slab serpentinize the overlying mantle wedge, which subsequently couples to the plate and is similarly dragged to greater depths beneath the arc (Wysoczanski et al., 2006).

Added to the 2-D thermal model in Figure 4.22b are the upper stability limits for serpentine and chlorite in the overlying mantle wedge. Dehydration of subducted sediment and altered oceanic crust at low P-T beneath the forearc region could release fluids into the overlying mantle wedge, where mantle peridotite would react with the fluids to form serpentinite. This hydrated material would be down-dragged with the slab, and eventually the serpentinite would break down at depths of <100 km and temperatures of ~600°C (based on the phase stability of serpentinized mantle; Rupke et al., 2004). However, the fluids released by this breakdown could be incorporated into chlorite in the mantle wedge, which would continue its slab-coupled movement to greater depths until the breakdown of chlorite at ~800°C (Grove et al., 2006). The stability of chlorite to

these depths would enable production of hydrous fluids over fairly large distances (~100 km) behind the volcanic front in the MGVF. However, there is still a significant region of the MGVF at distances > 100 km behind the front with high H_2O that still cannot be explained by these mechanisms (Figs. 4.9, 4.10).

The strong correlations of H_2O with both Cl and S in the MGVF primitive melts support the role of a single phase, such as serpentine or chlorite, controlling fluids released into the mantle wedge. Figure 4.7a illustrates the constant salinity displayed by the MGVF melts. In order for such a constant Cl/H_2O ratio to be maintained across the arc, it seems that a single phase must be controlling this ratio. Studies of serpentinite and associated fluids suggest that the salinities of fluids released during serpentinite breakdown range from 4-8 wt% NaCl (light gray field in Fig. 4.7; Scambelluri, 2004), which overlaps with the MGVF data. The salinity of fluids related to chlorite breakdown is unknown, but the fluids released by serpentinite should be incorporated by chlorite and may have similar salinities. The MGVF Cl/H_2O data are also very similar to the salinities of fluids released from the upper oceanic crust (4-30 wt% NaCl; Philippot et al., 1998).

Another model invoked for fluid release at great depth involves the breakdown of serpentinite in the subducting oceanic lithosphere (Rupke et al., 2002; Abers et al., 2003; Schmidt and Poli, 2004; Spandler et al., 2008). For example, the subducting Cocos plate beneath Nicaragua is extremely H_2O-rich (Abers et al., 2003); such hydration has been linked to extensive fracturing of the subducting slab prior to subduction that allowed sea water to penetrate the oceanic crust to great depths, resulting in converstion of the mantle in the subducting slab to serpentinite (Rupke et al., 2002; Abers et al., 2003). Rupke et al. (2002) showed that the serpentinite in the slab beneath Nicaragua is stable to high

pressures, releasing its H_2O at depths of 130-160 km. However, fluids released by serpentinite breakdown should have low $\delta^{18}O$; Nicaragua magmas have $\delta^{18}O_{olivine}$ values of 4.6-5.2‰ (Eiler et al., 2005), the only arc in the world to have $\delta^{18}O_{olivine}$ values lower than normal mantle. Furthermore, fluids released from the breakdown of serpentinite typically have high fluid mobile element concentrations (Tenthorey and Hermann, 2004), and magmas in Nicaragua have high Ba/La ratios (Fig. 4.23; Eiler et al., 2005). In order to reconcile this model of oceanic lithosphere-derived fluids with the high $\delta^{18}O$ values for MGVF olivine and the influence of sediment fluids/melts suggested by trace element data, the fluids rising through the slab from serpentinite breakdown would have to interact with the previously dehydrated sediment overlying the slab and partially melt it. While this model could potentially produce the high MGVF $\delta^{18}O$ values, the MGVF magmas lack the high Ba/La ratios associated with serpentinite-derived fluids, and there is no evidence for pervasive serpentinization of the Cocos plate offshore of Mexico. Therefore, we conclude that this model is unlikely for generation of H_2O-rich components beneath the MGVF.

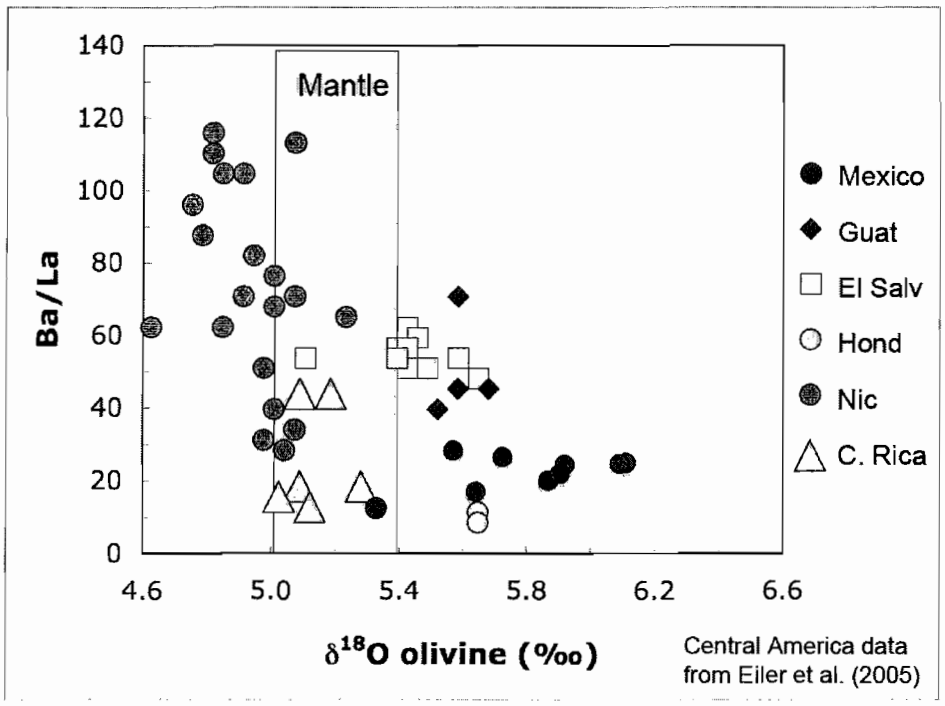

Figure 4.23. Whole rock and bulk tephra Ba/La vs olivine oxygen isotopic compositions for Central America and Mexico.

The H_2O-rich, high $\delta^{18}O$ fluids in the MGVF could be produced by dehydration of sediment and altered oceanic crust beneath the forearc, where the fluids are subsequently stored in hydrous phases like serpentine and chlorite in the mantle wedge. Down-dragging of this hydrated mantle material with the subducting slab and breakdown of the hydrous minerals could release fluids further behind the volcanic front. Although this model can explain the oceanic crust-derived fluid signature in the MGVF magmas, the high $\delta^{18}O$ values and trace element compositions of MGVF magmas and modeled subduction components all suggest involvement of sediment melts in the H_2O-rich component rather than fluids generated by sediment dehydration. In order to melt the subducted sediment beneath the volcanic arc, fluxing of fluids is required to lower the melting temperature of the sediments. Although the top of the altered oceanic crust has

dehydrated by ~ 100 km depth, the temperatures at the bottom of the subducting crust are cool enough that dehydration should occur until ~130 km (based on the phase equilibria of meta-basalt; Rupke et al., 2004). Based on wet solidus temperatures for pelagic clays of ~650°C (Nichols et al., 1996), the percolation of fluids through the oceanic crust and into the overlying sediment package could induce melting of the sediments. The rising sediment melt may in turn melt the overlying hydrated mantle, or the sediment melts may mix with the fluids being released from the downdragged chlorite. Either scenario can produce the complex high-H_2O, high- $\delta^{18}O$ subduction component with both sediment melt and altered oceanic crust-derived fluid components. However, based on our thermal model of the subduction zone and constraints on the origin of the subduction-derived components, it does not appear possible to generate high-H_2O, high- $\delta^{18}O$ magmas derived from sediment melts and slab fluids beyond slab depths of ~130 km (or ~ 175 km behind the volcanic front). Thus, another model is required to explain the broad region of H_2O-rich melts far behind the front in the MGVF.

7.2.2. Dehydration of subducted material – 3 Ma

As mentioned earlier, modeling slab devolatilization beneath the MGVF has the added complexity of changes in the subducting slab geometry over the past ~ 3 Ma. While it is not possible to know the exact slab geometry at 3 Ma, it seems likely that the slab had a configuration similar to the current geometry near Mexico City. Following this assumption, a second 2-D thermal model was created for the MGVF at 3 Ma (Fig. 4.24). Employing the same P-T assumptions for sediment and metabasalt dehydration (Rupke et al., 2004) in this configuration, fluids released from dehydration of sediment

could have hydrated the mantle wedge in the region now just behind the modern arc (~250 km from the trench, Fig. 4.21b). Dehydration of the altered oceanic crust would have continued into the regions of the MGVF now ~300 km from the volcanic front; such fluids could also have melted the overlying sediment package, as discussed above. Additionally, the stability fields for serpentine and chlorite in the mantle wedge in the shallow slab configuration suggest that fluids could have been efficiently transported to depths in the mantle wedge that correspond to the regions of high-H_2O far behind the front today (~ 350 km from the trench, Fig. 4.21b). Thus, the slab geometry at 3 Ma would have enabled production of sediment melts and hydrous, oceanic crust-derived fluids at the high-H_2O localities located far behind the volcanic front today.

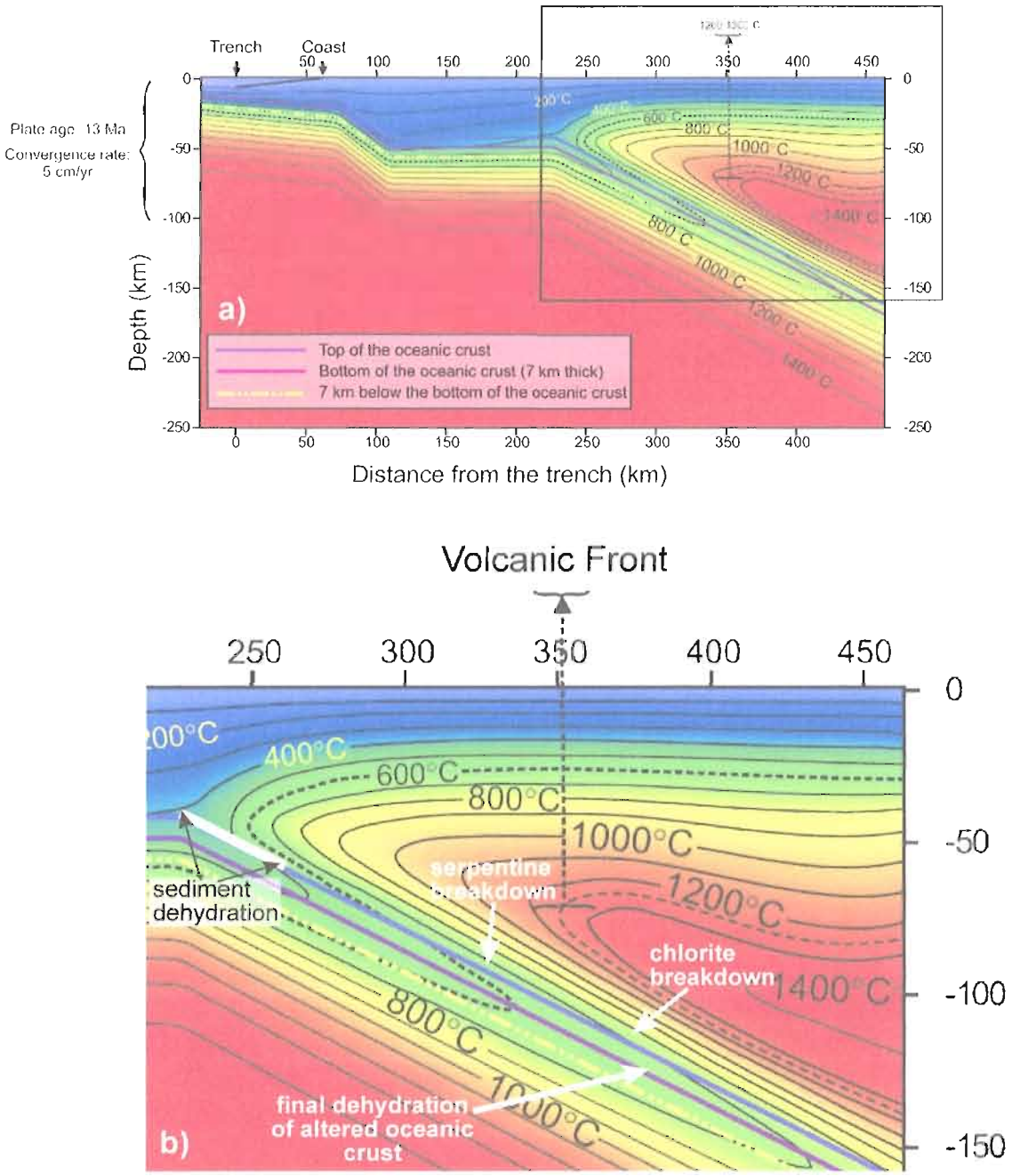

Figure 4.24. (a) 2-D thermal model of the subduction zone beneath the MGVF at 3 Ma. (b) thermal structure of the mantle wedge, with regions indicated for sediment dehydration and the maximum stability of serpentine and chlorite, and the depth at which dehydration of the entire section of altered oceanic crust should be complete (as in Fig. 4.20).

Unfortunately, it is not possible to definitively resolve the influence of slab migration on the generation of hydrous melts across the MGVF. While much of the volcanism at 3 Ma is concentrated in the region far behind the front, it is also clear that activity in this region has persisted into recent times. Using a compilation of age estimates of MGVF cinder cones (Hasenaka and Carmichael, 1985; Ban et al., 1992; Suter et al., 2001; Ownby et al., 2008) it is clear that most of the volcanic activity younger than 1 Ma is located near the region of the current volcanic front (Fig. 4.21). However, there is wide variability in the ages of cinder cones across the arc, and volcanoes far behind the front have been active as recently as ~ 50,000 ybp (Suter et al., 2001; Fig. 4.21). Thus, it is possible that at least some of the volatile-rich magmas erupted far behind the front at 2-3 Ma when the slab was shallower or moving trenchward. However, it is also possible that some of the volatile-rich magmas far behind the front erupted more recently, produced by melting of previously hydrated mantle. Whether or not this same process affected volcanoes near the current volcanic front is difficult to ascertain. The geometry of the slab in the 3 Ma 2-D model (based on the present-day configuration near Mexico City) is relatively flat until ~250 km from the trench, suggesting that no mantle wedge was present trenchward of the change in slab dip. Based on this geometry, pre-hydration of the mantle wedge near the current volcanic front is not a viable option. However, this is based on our best estimate of the previous slab configuration, and other geometries could allow for a larger mantle wedge that could have been affected by pre-hydration.

The change in slab geometry over the past 3 Ma has important implications for mantle flow and production of melts by decompression. Trenchward migration of

subducting slabs creates suction in the mantle wedge, which would increase the corner flow of mantle from far behind the arc. Melting of this mantle, which has not undergone previous fluid-flux melting, would yield melts that are relatively enriched (i.e., high HFSE). This advection of mantle has been suggested to produce alkaline, decompression melts erupted in western Mexico (Luhr, 1997). This model fits well with the relatively enriched, low-H_2O, low degree partial melts present far behind the front in the MGVF (e.g., Hoya Alvarez). The abrupt transition into low-H_2O, high HFSE melts seen in the spatial map of H_2O contents (Figs. 4.9, 4.11) may indicate a region dominated by decompression melts, resulting from strong advection caused by the trenchward migration of the Cocos slab in the past 3 Ma.

The arc in Mexico has the added complexity of having been active since the Miocene (Nixon et al., 1987; Ferrari et al., 1994), suggesting that the mantle wedge has potentially been metasomatized over the past 10-20 Ma. Changes in the geometry of the subduction zone over this time would have permitted different regions of the mantle wedge to be hydrated by fluids derived from a variety of subducted material (e.g., slab, sediments). Furthermore, it is possible that repeated hydration of the mantle wedge could also produce melts with high $\delta^{18}O$ values (Dorendorf et al., 2000). These pre-hydration events are difficult to detect because they are not old enough to cause strong isotopic aging of the mantle wedge, but it does seem likely that in such a long-lived subduction zone the mantle wedge (particularly lithospheric mantle) may have been repeatedly hydrated by a variety of fluids and melts. However, our data and modeling suggest that such older hydration and enrichment are not required to produce the geochemical patterns of magmatism during the past 3 Ma.

8. Conclusions

In spite of the young age of the subducting Cocos plate, primary melt H_2O (~3-5 wt%) and other volatile concentrations remain high for large distances (~150 km) behind the volcanic front in the MGVF. Additionally, $\delta^{18}O_{olivine}$ values measured for the MGVF (5.6-6‰) are higher than values obtained in Central America and most other arcs worldwide. The MGVF magmas originate from an EMORB mantle source that has been variably depleted by previous partial melting and melt extraction, producing compositional heterogeneity. By calculating source region compositions specific to each volcano, we were able to calculate the amount and composition of H_2O-rich subduction-derived components added to the mantle wedge.

The combination of high $\delta^{18}O_{olivine}$ values, correlation between magma and sediment Th/Rb, and trace element compositions of the modeled H_2O-rich components all suggest that the H_2O-rich, subduction-related components originated from mixtures of sediment melts and altered oceanic crust-derived fluids. However, 2-D thermal models suggest that dehydration of sediment and much of the oceanic crust should occur beneath the forearc region. To reconcile these data, we propose two models, which are not mutually exclusive:

1. Sediments and much of the altered oceanic crust dehydrated beneath the forearc, hydrating the overlying mantle wedge and producing hydrous minerals such as serpentine. The hydrated mantle wedge was subsequently down-dragged with the subducting slab and the serpentine eventually broke down, causing H_2O to be stored in chlorite, a hydrous mineral stable to higher P and T. Dehydration of the middle and lower portions of the oceanic slab

continued until depths of ~130 km. Percolation of these fluids through the overlying subducted sediment induced melting of the sediment. The sediment-derived melts rose and melted or mixed with the hydrated overlying mantle wedge, producing high-H_2O, high-$\delta^{18}O$ magmas with variable sediment melt and oceanic-crust-derived fluid signatures. However, this model is incapable of producing hydrous melts at distances far behind the volcanic front.

2. The MGVF mantle wedge was previously hydrated over the past ~3 Ma, when the slab migrated trenchward from a relatively flat geometry. The shallower slab dip at 3 Ma and subsequent slab steepening would have caused hydration of large regions of the mantle wedge, which now underlie the MGVF. Dehydration and melting would have proceeded as outlined in model 1, however, the shallow slab dip would have enabled production of H_2O-rich, high- $\delta^{18}O$ magmas far behind the current volcanic front.

These scenarios are not necessarily applicable to all arcs worldwide, due to the fact that Mexico is a "hot" subduction zone. In comparison with other arcs where young crust is subducted, the MGVF $\delta^{18}O_{olivine}$ values are similar only to northern Central America, where $\delta^{18}O_{olivine}$ values reach 5.7‰. These regions share similarities in subducting material, specifically that the mantle beneath the oceanic crust in the downgoing slab is not heavily serpentinized, and oceanic sediments are being efficiently subducted. Both of these factors contribute to high magmatic $\delta^{18}O$ values. Furthermore, it is important to remember that the MGVF magmas are unique in both the persistently high volatile contents across the arc and their high $\delta^{18}O_{olivine}$ values. It seems that the

longevity of subduction beneath the MGVF and the recent change in slab geometry make this volcanic field somewhat unique. These factors allowed for hydration of a much larger region of mantle wedge than in other some other arcs. Slab rollback and trenchward migration of subduction-related volcanism have occurred in other arcs as well, so results of this study have applicability to other arcs that have migrated over time.

CHAPTER V

CONCLUSIONS

In this dissertation I investigated the physical and chemical processes of subduction zone volcanism from the crust and Earth's surface (degassing, crystallization, and eruptions of cinder cone volcanoes) to the mantle (melt generation) and subducted slab (release of H_2O-rich components). In this chapter I summarize the results and implications of this work.

In Chapter II, I presented a detailed study of the eruption of one subduction-related cinder cone, Volcán Jorullo, in central Mexico. Using a variety of datasets, I showed that, in spite of the relatively small size of cinder cone volcanoes, their eruptions can be complex. Analysis of melt inclusion volatile contents and compositions revealed the high initial volatile concentrations and compositional evolution over time of the Jorullo magmas. The evolution of Jorullo magmas was driven by deep crystallization of several phases – amphibole + olivine ± clinopyroxene. Pressures of melt inclusion entrapment indicate that olivine crystallized over a wide range of depths early in the eruption, and that crystallization depths shallowed as the eruption progressed. Olivine compositional zoning and measurements of groundmass crystallinity suggest that crystals were stored for increasing periods of time shallowly beneath the volcano as the eruption progressed, and that more extensive crystallization of the groundmass occurred late in the eruption. Together, these data point to the formation of a shallow storage region beneath

the volcano where degassing, crystallization, and melt storage occurred late in the eruption. Overall, this study illustrates that the magmatic processes driving cinder cone eruptions can be very complex, and this may be true especially for long-lived volcanoes like Jorullo. The longevity of the eruption (15 years) may have allowed the plumbing system to develop such a storage region over time, whereas in shorter-lived cinder cone eruptions, the plumbing systems are simpler, dike-like systems.

I hope that this study motivates further research on the intricacies and variability of cinder cone eruptions and for hazard assessment of cinder cone volcanoes. Such an explosive, 15-year cinder cone eruption could be devastating on the surrounding population and environment from a hazards perspective. Considering that cinder cones are the most abundant type of volcano on land, assessing their potential hazards is essential.

Building on my study of the Jorullo cinder cone eruption, I then assessed the degassing behavior of subduction-related several cinder cone eruptions from Mexico (Chapter III). Using melt inclusion and groundmass glass volatile concentrations, I investigated the degassing of volatiles (H_2O, CO_2, S, Cl) in these basaltic melts. I concluded that the process of gas fluxing – or flushing of CO_2-rich gas from depth through the conduit system – seems to be a common process at most of the cinder cones in Mexico. Interestingly, the composition of the fluxed vapor is very similar for basaltic melts worldwide (50-75% CO_2), suggesting that subduction zone magmas have similar and high CO_2 concentrations (> 7000 ppm) at depth. In this chapter I also investigated the vapor-melt partitioning of S and Cl in basaltic melts. In most melts degassing of S was minimal until low pressures, when extensive shallow degassing occurred prior to and

during eruption, whereas degassing of Cl was not pressure dependent. I suggested that the variations in degassing behavior among the MGVF volcanoes can be attributed to several factors: 1) melt composition, 2) oxygen fugacity of the melt, and 3) eruption style.

Overall, this study highlighted the similarities and differences of degassing in basaltic melts, and the different factors that can affect the degassing process. Furthermore, the degassing behavior of long-lived cinder cones of the MGVF is very similar to larger basaltic volcanoes, like Mt. Etna in Italy, suggesting that in spite of the differences in eruption longevity and volume, these systems are not all that different. Again, cinder cone systems are not well studied and this research only sampled a very small portion of the population, and thus I hope that this study leads to further research on degassing in cinder cone systems worldwide.

From these studies of arc cinder cone eruptions, I broadened the scope of my research to investigate the complex process of producing such subduction-zone melts (Chapter IV). Using a variety of datasets, I sought to better understand the origin of H_2O-rich components added to the mantle wedge beneath the MGVF. In studying the compositions and volatile contents across the arc in the MGVF, I found that magmatic H_2O remains high (3-5.3 wt%) for large distances (150 km) behind the volcanic front. These results were surprising, given that the young age, and therefore relatively high temperature, of the subducting plate beneath the MGVF would suggest that the subducting material should dehydrate beneath the forearc. Analyses of the oxygen isotopic composition of olivine phenocrysts in the MGVF reveal that oxygen isotopic ratios are higher (5.6-6‰) than for typical mantle-derived magmas, but do not vary

systematically across the arc. Based on the high $\delta^{18}O_{olivine}$ values measured for the MGVF, I suggested that the compositions of the H_2O-rich subduction-related components added to the mantle wedge appear to be mixtures of slab-derived fluids and sediment-derived melts. This hypothesis was supported by a 1:1 correlation of Th/Rb in MGVF magmas and subducting sediment Th/Rb, suggesting involvement of sediment melts in formation of the MGVF magmas. Using these data combined with new 2-D thermal models of the subduction zone beneath the MGVF, I proposed two models, not mutually exclusive, to explain the origin of H_2O-rich subduction-related components: 1) fluids released from the dehydration of the altered oceanic crust flux-melt the overlying subducted sediment, and these melts then mix with or melt the hydrated, downdragged mantle wedge; and 2) a shallower slab geometry at ~ 3 Ma facilitated dehydration and melt production (in a scenario similar to (1)) far behind the current volcanic front.

Overall, this study illuminated the complexities of dehydration and melt production in subduction zones. It also demonstrated the need for utilizing a multi-disciplinary approach when addressing such complex systems. Without the combination of datasets that I used in this study, it would not have been possible to pinpoint the origin of the H_2O-rich subduction components, nor to assess where these components were added to the mantle wedge.

In summary, my dissertation addresses both the small scale processes in subduction zone volcanism, such as degassing and compositional evolution of melts at basaltic cinder cones, and the large scale issues of melt generation in subduction settings. This work illustrates that basaltic cinder cones, in spite of their relatively small size, are complex and similar in many ways to larger-volume basaltic volcanoes. Furthermore, the

generation of these melts in subduction zones is exceedingly complex. Factors such as the type of material being subducted, the age/temperature of the subducting slab, and the tectonic history of the subduction zone need to be considered when assessing fluid fluxing and melt production in a subduction zone setting. Finally, this work illustrates the importance of utilizing multiple types of data in order to deal with these complexities and assess the origin of H_2O-rich components in a subduction zone.

APPENDIX A

SUPPLEMENTARY DATA TABLE 1: UNCORRECTED MELT INCLUSION COMPOSITIONS

Group	Early	Early	Early	Early	Early	Early	Early	Early	Early	Early	Early	Early	Early	Early	Early	Early
Inclusion	1	12_1	12_2	12_3	13_1	13_2	14	17_1	17_2	17_A	20	23	24	28	29_1	29_3
SiO_2	51.98	50.49	51.80	50.78	49.19	49.27	50.83	51.66	50.01	49.71	50.05	49.22	49.19	52.23	49.64	50.07
TiO_2	0.90	0.71	0.68	0.89	0.88	0.76	0.76	0.68	0.87	0.81	0.89	0.80	0.90	0.85	0.79	0.77
Al_2O_3	17.65	17.32	18.77	17.98	18.89	19.81	19.46	17.49	18.57	18.31	18.05	18.43	20.55	19.14	18.36	19.01
FeO^T	7.23	6.35	5.95	5.70	7.24	6.86	5.65	6.04	5.82	6.14	5.76	5.56	5.32	6.12	6.95	5.30
MnO	0.16	0.13	0.07	0.06	0.08	0.21	0.02	0.10	0.15	0.04	0.12	0.07	0.06	0.12	0.14	0.10
MgO	5.13	6.29	4.13	5.28	6.14	5.53	3.26	5.32	4.70	4.96	4.88	4.99	2.81	2.92	5.16	5.22
CaO	10.37	9.64	9.32	9.42	8.91	9.38	10.23	8.26	9.18	8.95	9.87	9.34	10.05	9.54	9.25	9.97
Na_2O	4.24	5.01	5.14	4.92	4.43	5.07	5.85	5.01	5.61	5.18	4.42	4.30	5.62	5.16	4.77	5.00
K_2O	0.86	0.67	0.84	0.75	0.81	0.84	0.80	0.71	0.73	0.73	0.70	0.74	0.83	0.98	0.80	0.72
P_2O_5	0.21	0.16	0.17	0.14	0.16	0.16	0.19	0.15	0.16	0.15	0.18	0.24	0.15	0.17	0.17	0.17
S ppm	1339	1284	1574	1958	1648	1632	2093	1926	1903	2288	2089	2091	2237	839	1899	1848
Cl ppm	1286	1266	1366	1386	1332	1471	1683	1363	1494	1424	1433	1328	1492	1348	1285	1356
Total	99.17	97.05	97.18	96.28	97.07	98.22	97.50	96.18	96.14	95.42	95.34	94.10	95.88	96.99	96.36	96.72

Group	Middle	Middle	Middle	Middle	Middle	Late	Late	Late	Late	Late	Late	Late	Late
Inclusion	4	5	6	7_1	10	1	3_1	3_2	4	5	p1	p2	p3a
SiO_2	53.03	55.05	48.94	50.31	53.39	51.90	53.09	56.02	54.30	51.14	51.13	53.91	55.04
TiO_2	0.79	0.96	0.89	0.92	0.85	1.02	1.00	1.19	0.94	0.84	1.10	1.06	0.93
Al_2O_3	18.10	19.74	19.91	20.34	22.75	20.74	20.11	19.11	19.28	20.35	21.09	20.05	18.14
FeO^T	7.17	6.46	6.06	6.85	4.85	5.96	6.52	5.45	6.59	6.42	5.98	4.68	5.65
MnO	0.12	0.12	0.10	0.12	0.08	0.08	0.16	0.03	0.07	0.10	0.08	0.06	0.04
MgO	5.28	4.03	5.04	5.36	2.62	4.29	3.54	3.06	2.88	4.42	4.53	1.69	5.09
CaO	9.41	9.68	10.50	10.01	8.15	10.16	9.46	8.79	8.71	9.52	9.89	8.91	8.85
Na_2O	4.20	5.02	4.26	4.46	5.70	4.49	4.58	4.31	4.99	4.22	4.69	4.61	3.78
K_2O	0.85	1.26	0.82	0.87	1.03	0.77	0.90	0.90	1.09	0.83	0.75	0.81	0.61
P_2O_5	0.16	0.19	0.19	0.21	0.19	0.23	0.24	0.21	0.22	0.24	0.20	0.18	0.17
S ppm	1478	1392	2039	1856	1887	1442	1143	74	918	1490	1477	2106	1479
Cl ppm	956	1336	1094	1171	1503	1239	1162	1020	994	1065	1206	1298	936
Total	99.47	102.86	97.24	99.93	100.11	100.10	100.01	99.25	99.39	98.51	100.02	100.00	99.96

APPENDIX B

CORRECTION PROCEDURES FOR MELT INCLUSION COMPOSITIONS

All melt inclusion data were corrected for post-entrapment crystallization of olivine (Sobolev and Chaussidon, 1996) and diffusive loss of Fe (Danyushevsky et al.,2000). Post-entrapment crystallization correction involves adding equilibrium olivine, in incremental fractions of 0.1 wt%, back into the melt inclusion until the melt inclusion composition is in equilibrium with its host olivine (as analyzed by electron microprobe). There are two variables used in calculating the equilibrium olivine composition: the K_D value and the FeO/FeO^T ratio. We used a K_D of 0.3 ± 0.01 (Toplis, 2005), and we used an FeO/FeO^T value of 0.78 ± 0.01, based on the Jorullo whole rock lava data from Luhr and Carmichael (1985). Following the procedure of Danyushevsky et al. (2000) we also corrected the inclusions, if necessary, post-entrapment Fe-loss. We plotted the melt inclusion FeO^T vs MgO data along with the whole rock data from Luhr and Carmichael (1985), and those inclusions with low FeO^T compared to the whole rock trend had Fe added into their compositions until they fell along the trend. We calculated an error for this procedure by fitting a regression line to the whole rock FeO^T vs MgO data, and we used the maximum residuals, ± 0.16, as the error in our Fe addition calculation. Using these three potential sources of error, K_D, FeO/FeO^T, and the error in Fe-addition, we ran melt inclusion compositions through the post-entrapment correction varying one variable at a time. This resulted in a range of compositions for each inclusion, with our restored values representing the average value. The errors (absolute) we report are maximum errors, as they are the maximum differences between our average composition and the most and least corrected runs: SiO_2: ± 0.29, Al_2O_3: ± 0.39, FeO^T: ± 0.23, MgO: ± 0.79,

CaO: ± 0.21, Na_2O: ± 0.09, K_2O: ± 0.02, TiO_2: ± 0.02, MnO: ±0.002, P_2O_5: ± 0.004. The most affected element is Mg, however, even the errors in our MgO data are relatively small (± 0.8).

APPENDIX C

SUPPLEMENTARY TABLE 2: BULK TEPHRA XRF

Unnormalized Major Elements (Wt %):			
	Early	**Middle**	**Late**
SiO_2	52.84	51.36	52.89
TiO_2	0.67	0.70	0.88
Al_2O_3	15.56	14.86	15.96
FeO*	7.18	7.58	7.54
MnO	0.13	0.13	0.13
MgO	11.46	11.53	10.39
CaO	7.82	7.77	7.41
Na_2O	3.36	3.11	3.44
K_2O	0.70	0.69	0.82
P_2O_5	0.14	0.14	0.19
Total	99.86	97.88	99.66
Unnormalized Trace Elements (ppm):			
Ni	357	318	256
Cr	625	630	448
Sc	23	24	21
V	162	170	163
Ba	222	221	248
Rb	11	11	13
Sr	443	408	465
Zr	78	79	100
Y	14	14	16
Nb	3	2	5
Ga	16	16	17
Cu	51	57	37
Zn	71	72	76
Pb	3	3	4
La	5	5	10
Ce	18	20	18
Th	0	0	0
Nd	14	12	15

X-Ray Fluorescence (XRF) analyses conducted at the GeoAnalytical Laboratory at Washington State University. LOI (loss on ignition) values were less than zero for all samples. Detailed discussion of analytical techniques and sample preparation can be found in Johnson et al. (1999).

APPENDIX D

SUPPLEMENTARY DATA TABLE 3: TEPHRA GROUNDMASS GLASS COMPOSITIONS

Oxides (wt%)	Early		Middle		Late	
SiO_2	58.28	(0.27)	58.36	(0.43)	58.34	(0.38)
TiO_2	1.33	(0.15)	1.37	(0.19)	1.46	(0.13)
Al_2O_3	14.70	(0.31)	14.74	(0.30)	14.52	(0.22)
FeO	8.92	(0.24)	8.63	(0.39)	8.74	(0.19)
MnO	0.17	(0.07)	0.19	(0.04)	0.15	(0.04)
MgO	4.32	(0.13)	3.86	(0.16)	3.68	(0.09)
CaO	7.56	(0.34)	6.90	(0.37)	6.62	(0.40)
Na_2O	4.29	(0.17)	4.44	(0.28)	3.79	(0.30)
K_2O	1.30	(0.03)	1.43	(0.08)	1.62	(0.06)
P_2O_5	0.26	(0.02)	0.28	(0.03)	0.34	(0.03)
S ppm	35	(71)	35	(70)	12	(63)
Cl ppm	1074	(127)	865	(161)	1063	(103)
Total	101.34		100.37		99.44	

Groundmass glass analyses by electron microprobe for tephra from early, middle and late samples. Averages are reported based on 10-25 points per sample with standard deviations in parentheses.

APPENDIX E

SUPPLEMENTARY DATA TABLE 4: MELT INCLUSION TRACE ELEMENT CONCENTRATIONS MEASURED BY LA ICP-MS.

Trace element (ppm)	Early 12_3	Early 13_1	Early 20	Early 24	Early 28	Middle 4	Middle 6	Middle 10	Late 1	Late 3_1	Late 3_2	Late 4
Rb	9	10	7	6	10	12	10	13	13	15	16	16
Ba	195	236	184	164	231	236	257	233	265	300	264	242
Th	0.3	0.4	BDL	0.4	1	1	1	1	1	1	2	1
Nb	2	3	2	2	3	3	3	2	7	6	5	5
Ta	0.2	BDL	BDL	BDL	BDL	0.2	BDL	BDL	0.4	0.4	0.3	BDL
U	0.1	0.2	BDL	BDL	0.2	0.1	BDL	0.2	0.4	0.3	0.3	0.2
La	7	8	6	6	8	9	9	6	12	13	14	12
Ce	16	17	16	12	17	19	24	14	26	26	25	23
Pb	3	4	4	9	4	4	4	3	4	5	6	5
Sr	467	523	463	402	424	467	622	492	614	586	551	525
Nd	12	11	9	8	13	12	15	9	17	17	16	18
Zr	72	94	70	69	83	88	107	89	134	169	165	144
Sm	6	2	2	1	1	3	3	2	4	3	5	4
Eu	1	1	1	1	1	1	2	1	1	1	1	1
Y	15	17	13	12	17	17	20	16	24	27	26	25
Yb	2	1	1	1	2	2	2	2	1	3	1	2
Ti	4088	4715	3900	3148	3989	4614	5862	4104	6582	5907	5676	5451

Above values are corrected for post-entrapment crystallization (PEC) of olivine

Trace element (ppm)	Early 12_3	Early 13_1	Early 20	Early 24	Early 28	Middle 4	Middle 6	Middle 10	Late 1	Late 3_1	Late 3_2	Late 4
Rb	10	11	8	8	13	12	10	15	13	16	17	17
Ba	219	244	208	207	282	248	262	263	277	319	282	263
Th	0.4	0.4		0.6	1	1	1	1	1	1	2	1
Nb	3	4	2	2	3	3	3	2	7	6	5	6
Ta	0.2	BDL	BDL	BDL	BDL	0.2	BDL	BDL	0.4	0.4	0.3	BDL
U	0.1	0.2	BDL	BDL	0.2	0.1	BDL	0.3	0.4	0.3	0.3	0.2
La	8	8	7	8	10	9	10	7	13	14	15	13
Ce	17	18	18	15	20	20	24	16	27	28	26	25
Pb	4	4	4	11	4	4	4	4	4	5	6	6
Sr	523	542	524	506	517	491	634	554	642	623	589	571
Nd	14	11	10	10	16	13	15	10	18	18	17	20
Zr	80	98	79	87	101	92	109	100	140	179	176	157
Sm	7	2	3	2	1	3	3	2	4	4	5	5
Eu	1	1	1	1	1	1	2	1	1	1	1	1
Y	17	18	15	15	20	18	21	18	25	29	28	27
Yb	2	2	1	2	2	2	2	2	1	3	1	3
Ti	4572	4886	4412	3965	4864	4847	5976	4622	6892	6277	6064	5932

Above values are original LA ICP-MS values.

Laser ablation ICP-MS analyses of melt inclusions from early, middle and late samples. BDL indicates element was below detection limit. Average 1 standard error values (in ppm) are as follows: Rb: 0.7, Ba: 10.9, Th: 0.2, Nb: 0.5, Ta: 0.1, U: 0.1, La: 0.6, Ce: 0.9, Pb: 0.8, Sr: 18.4, Nd: 1.7, Zr: 4.8, Sm: 0.9, Eu: 0.2, Y: 1.3, Yb: 0.5, Ti: 169

APPENDIX F

MAJOR ELEMENT AND VOLATILE CONTENTS OF MELT INCLUSIONS FROM ALL MGVF CINDER CONES

Table 1: Major element and volatile compositions of melt inclusions, and host olivine composition (corrected values)

	Cerro San Juan												
	CSJ-1	CSJ-5	CSJ-31	CSJ-32	CSJ-33	CSJ-39	CSJ-41	CSJ-44	CSJ-45s	CSJ-45L	CSJ-46	CSJ-48	CSJ-51
SiO_2	51.79	51.52	50.40	52.01	51.29	50.61	51.59	51.54	52.30	51.79	51.43	50.91	51.56
TiO_2	1.18	1.04	1.03	1.08	1.07	1.23	1.31	0.97	1.08	1.11	0.93	1.17	1.19
Al_2O_3	17.64	18.11	18.54	17.21	17.92	18.74	18.79	18.35	18.04	18.12	18.36	18.59	17.95
FeO^T	9.35	9.24	9.41	9.48	9.41	9.41	9.03	9.15	9.25	9.29	9.41	9.26	8.97
MnO	0.08	0.12	0.09	0.14	0.10	0.10	0.11	0.11	0.06	0.08	0.10	0.06	0.11
MgO	7.12	6.76	7.31	7.17	7.09	6.88	6.26	6.62	6.93	6.95	6.49	7.16	6.83
CaO	8.34	8.58	8.68	7.88	8.76	8.35	8.24	8.37	7.36	8.04	8.53	8.21	8.43
Na_2O	3.39	3.52	3.48	3.72	3.28	3.52	3.52	3.71	3.65	3.19	3.52	3.45	3.79
K_2O	0.86	0.84	0.86	1.07	0.85	0.93	0.93	0.92	1.11	1.14	0.98	0.95	0.90
P_2O_5	0.23	0.27	0.21	0.23	0.23	0.25	0.22	0.25	0.23	0.29	0.24	0.23	0.25
H_2O	2.39	2.30	1.65	0.83	2.30	2.36	2.88	1.21	2.67	3.40	2.18	1.66	0.35
S ppm	834	988	957	451	852	1049	1105	1083	1232	1162	1044	1095	1024
Cl ppm	582	597	619	570	485	832	793	820	833	775	782	771	735
Fo	84.62	84.19	84.60	84.51	84.49	84.11	83.62	84.09	84.50	84.50	83.33	84.88	84.77

	Cerro el Hungaro										
	CeH 15	CeH 24	CeH 39a	CeH 39b	CeH 86	CeH 88	CeH 91	CeH 93	CeH 95	CeH 98	CeH 99
SiO_2	53.53	54.21	55.80	54.53	52.93	53.98	53.64	52.95	53.33	52.56	53.12
TiO_2	0.95	0.97	0.93	0.81	0.91	0.85	0.93	1.00	0.92	0.96	0.92
Al_2O_3	18.56	18.09	16.05	17.43	17.65	17.47	18.20	18.42	18.71	19.41	18.15
FeO^T	7.52	7.38	7.54	7.20	7.59	7.35	7.39	7.82	7.40	7.47	7.71
MnO	0.07	0.10	0.10	0.08	0.08	0.08	0.10	0.08	0.10	0.06	0.09
MgO	5.92	7.31	7.39	7.00	7.83	7.71	6.86	7.29	6.81	7.01	7.17
CaO	8.27	8.22	6.68	7.48	7.87	7.60	7.77	8.04	8.38	8.07	7.95
Na_2O	4.09	2.61	4.07	4.23	4.13	3.90	3.98	3.51	3.55	3.54	4.06
K_2O	0.85	0.87	1.22	1.01	0.80	0.84	0.94	0.70	0.64	0.73	0.65
P_2O_5	0.24	0.24	0.22	0.23	0.21	0.21	0.19	0.19	0.17	0.19	0.18
H_2O	0.00	1.85	0.55	0.00	1.37	0.00	0.56	2.59	2.49	1.77	1.51
S ppm	1490	1507	57	168	1457	255	386	1404	1423	1435	1439
Cl ppm	721	725	703	643	679	540	1025	909	1059	1056	1061
Fo	87.40	87.80	87.53	87.53	88.07	88.21	87.01	86.70	86.95	87.12	87.27

Table 1 (cont.): Major element and volatile compositions of melt inclusions, and host olivine composition (corrected values)

	Jorullo															
	1	12 1	12 2	12 3	13 1	13 2	14	17 1	17 2	17 A	20	23	24	28	29 1	29 3
SiO_2	51.15	51.54	52.06	51.58	50.60	50.11	50.93	52.90	51.32	51.19	51.22	50.63	49.89	51.57	51.01	50.26
TiO_2	0.79	0.68	0.63	0.75	0.88	0.75	0.67	0.74	0.80	0.74	0.88	0.75	0.73	0.65	0.76	0.71
Al_2O_3	15.66	16.77	17.25	16.96	18.90	19.46	17.15	16.44	17.21	17.46	16.74	17.15	17.87	16.63	17.69	17.55
FeO^T	7.84	7.38	7.30	7.36	7.65	7.26	7.46	7.47	7.52	7.41	7.55	7.56	7.62	7.48	7.65	7.57
MnO	0.15	0.13	0.06	0.08	0.08	0.21	0.02	0.10	0.10	0.04	0.15	0.07	0.05	0.10	0.14	0.09
MgO	10.51	9.23	9.00	9.44	7.75	7.43	9.99	9.29	9.64	9.25	9.91	10.03	10.46	9.82	8.69	9.56
CaO	9.20	9.34	8.57	8.91	8.92	9.21	9.01	8.28	8.55	8.93	9.14	8.96	8.60	8.55	8.92	9.21
Na_2O	3.74	4.13	4.20	4.04	4.26	4.59	3.89	4.01	4.04	4.17	3.60	4.00	3.92	4.25	4.21	4.21
K_2O	0.77	0.65	0.77	0.73	0.81	0.83	0.70	0.65	0.67	0.68	0.61	0.66	0.72	0.84	0.77	0.66
P_2O_5	0.18	0.15	0.16	0.15	0.16	0.16	0.17	0.13	0.15	0.14	0.19	0.19	0.14	0.12	0.16	0.16
H_2O	0.95	4.58	4.74	2.47	4.16	3.47	1.23	5.31	2.51		1.52	3.95	2.27	1.02	3.01	3.42
S ppm	1149	1195	1379	1751	1591	1560	1718	1751	1665	2066	1847	1882	1776	688	1737	1644
Cl ppm	1103	1179	1197	1239	1285	1406	1381	1239	1308	1286	1267	1196	1185	1105	1176	1206
Fo	91.05	90.29	89.93	90.36	88.37	88.44	90.48	90.14	90.28	90.14	90.54	90.70	90.61	90.03	89.32	90.21

	Cerro el Astillero									
	CA-2	CA-5	CA-6-1	CA-7	CA-10	CA-11	CA-12	CA-12b	CA-14	CA-15
SiO_2	53.56	49.67	51.85	51.75	51.50	50.87	50.31	50.64	50.50	50.34
TiO_2	16.25	17.97	19.02	15.41	17.75	17.94	17.49	16.01	17.88	17.94
Al_2O_3	8.74	8.03	7.98	9.58	8.05	8.09	8.06	8.79	8.10	8.13
FeO^T	7.04	10.11	8.59	9.55	8.76	8.93	9.49	10.50	8.66	9.28
MnO	8.39	8.56	9.00	8.37	9.12	8.88	9.08	7.93	8.98	8.95
MgO	3.75	3.89	1.63	3.72	3.08	3.55	3.81	4.26	3.95	3.70
CaO	1.01	0.60	0.59	0.59	0.58	0.61	0.60	0.77	0.61	0.61
Na_2O	0.96	0.91	0.94	0.77	0.83	0.91	0.84	0.88	1.02	0.83
K_2O	0.14	0.10	0.21	0.09	0.14	0.07	0.16	0.08	0.12	0.07
P_2O_5	0.16	0.18	0.18	0.17	0.19	0.16	0.15	0.14	0.19	0.14
H_2O	1.12	2.51	2.42	2.95	2.86	3.29	4.13	2.86	-	-
S ppm	400	1513	1583	1876	1486	1969	1735	1914	-	-
Cl ppm	1200	1029	983	1078	1049	1148	986	1059	-	-
Fo	87.28	89.29	86.91	89.27	88.81	88.91	89.43	89.43	88.58	89.19

Table 1 (cont.): Major element and volatile compositions of melt inclusions, and host olivine composition (corrected values)

	Paricutin									
	P506-1	P506-2	P506-3_1	P506-3_3	P506-4	P506-5	P506-6	P506-7	P506-8	P506-10
SiO_2	52.79	52.81	52.35	52.19	53.61	53.22	53.08	53.33	54.19	53.59
TiO_2	18.94	18.55	19.09	19.29	18.50	19.26	18.42	18.90	19.01	19.24
Al_2O_3	7.16	7.24	7.21	7.13	7.23	7.25	7.15	7.15	7.26	7.02
FeO^T	6.52	6.84	6.96	6.85	6.51	6.28	6.60	5.98	5.90	5.95
MnO	8.15	8.14	8.04	8.04	8.24	8.18	8.36	8.11	7.99	8.34
MgO	4.38	4.38	4.26	4.43	3.80	3.70	4.45	4.43	3.52	3.73
CaO	0.80	0.79	0.80	0.78	0.80	0.79	0.78	0.81	0.81	0.79
Na_2O	0.95	0.94	0.97	0.95	1.02	1.01	0.85	0.97	0.91	0.98
K_2O	0.09	0.07	0.09	0.08	0.08	0.07	0.06	0.07	0.15	0.11
P_2O_5	0.22	0.24	0.25	0.26	0.20	0.24	0.25	0.24	0.24	0.23
H_2O	4.01	4.21	3.44	3.73	3.87	3.92	3.93	3.52	4.24	-
S ppm	1524	1749	1895	1579	1662	1691	1669	1613	1324	-
Cl ppm	980	905	936	930	889	952	946	954	957	-
Fo	86.88	86.96	87.35	87.35	86.59	85.97	86.85	85.35	86.66	86.10

	Cerro San Miguel								
	CSM-A_2	CSM-A_3	CSM-A_4	CSM-A_6	CSM-A_7	CSM-A_8	CSM-A_12	CSM-A_13	CSM-A_14
SiO_2	51.06	57.74	53.69	55.12	55.63	57.24	51.75	49.81	50.50
TiO_2	20.17	15.88	18.34	19.37	16.37	15.71	19.38	19.86	18.69
Al_2O_3	6.64	8.99	6.75	8.55	9.66	10.00	6.40	6.78	7.09
FeO^T	6.32	4.48	5.69	3.27	5.05	4.16	6.54	7.25	7.66
MnO	10.12	6.11	9.41	6.65	6.06	6.35	10.10	10.73	10.46
MgO	3.81	3.89	4.17	4.07	4.36	3.78	3.86	3.71	3.76
CaO	0.62	1.29	0.66	1.52	1.26	1.23	0.54	0.50	0.54
Na_2O	0.97	1.19	0.98	1.13	1.24	1.12	1.10	1.00	1.02
K_2O	0.11	0.15	0.09	0.02	0.11	0.19	0.11	0.19	0.11
P_2O_5	0.20	0.28	0.21	0.31	0.27	0.23	0.22	0.19	0.16
H_2O	2.40	2.89	3.61	3.31	3.86	3.26	1.13	3.26	2.96
S ppm	2092	1190	1690	1220	1190	1260	1944	2107	2036
Cl ppm	904	877	883	881	753	895	911	848	731
Fo	87.98	75.17	87.15	72.54	75.78	74.08	88.27	88.61	88.76

Table 1 (cont.): Major element and volatile compositions of melt inclusions, and host olivine composition (corrected values)

Cerro el Pelon

	CeP-1	CeP-2	CeP-7	CeP-8	CeP-9_1	CeP-9_2	CeP-10	CeP-11	CeP-12	CeP-14	CeP-15	CeP-16	CeP-17_1	CeP-17_2	CeP-18
SiO_2	53.84	53.18	53.17	52.80	52.42	52.45	52.40	51.80	53.07	53.98	53.89	54.85	53.76	53.41	54.51
TiO_2	18.62	18.70	19.02	19.24	19.23	19.67	19.44	19.54	19.02	18.32	18.62	18.06	19.08	19.07	16.64
Al_2O_3	7.45	7.55	7.52	7.59	7.60	7.45	7.52	7.60	7.51	7.58	7.42	7.57	7.43	7.48	8.43
FeO^T	5.10	5.68	5.31	5.36	5.31	5.24	5.25	5.42	5.17	5.54	4.96	5.32	4.72	4.82	5.73
MnO	8.63	8.16	8.55	8.27	8.69	8.69	8.55	8.85	8.45	8.38	8.35	8.17	8.42	8.90	7.49
MgO	3.98	4.28	4.04	4.23	4.13	4.08	4.33	4.25	4.11	3.75	4.23	3.67	4.03	3.73	4.43
CaO	0.81	0.80	0.89	0.89	0.85	0.90	0.86	0.88	0.90	0.91	0.92	0.88	0.91	0.94	1.03
Na_2O	1.23	1.29	1.16	1.21	1.23	1.11	1.20	1.27	1.25	1.14	1.20	1.04	1.22	1.26	1.31
K_2O	0.06	0.02	0.02	0.09	0.19	0.05	0.12	0.07	0.20	0.09	0.11	0.13	0.12	0.09	0.13
P_2O_5	0.27	0.33	0.33	0.32	0.35	0.35	0.32	0.31	0.31	0.31	0.30	0.33	0.31	0.31	0.30
H_2O	3.32	2.58	2.09	2.75	0.91		2.38	1.47	2.66	2.52	2.56	3.67	2.00	2.11	1.37
S ppm	1337	2108	1398	1514	1536	1439	1417	1384	1458	1280.33	1392	555	1309	1489	532
Cl ppm	907	1017	1029	956	1044	1036	1005	989	983	919.53	924	873	990	992	1082
Fo	83.53	84.51	83.93	83.76	83.70	83.70	83.69	84.03	83.44	84.03	81.10	83.82	82.50	82.50	83.21

Cerro La Loma

	CLL-1 in1	CLL-1 in2	CLL-1 in3	CLL-2	CLL-3	CLL-1_2	CLL-1_3	CLL-1_4	CLL-1 5_1	CLL-1 5_2	CLL-1 6	CLL-1 7	CLL-1 8	CLL-1 9	CLL-1 10
SiO_2	53.09	53.45	54.13	52.47	51.62	51.15	52.66	52.66	51.80	51.68	52.79	52.86	54.59	53.33	51.84
TiO_2	17.84	18.08	17.55	16.45	15.26	14.81	18.59	18.59	18.72	18.99	18.42	18.88	18.29	18.52	19.16
Al_2O_3	8.48	8.08	8.03	8.46	8.28	8.78	8.14	8.14	8.20	8.14	8.17	8.20	7.99	7.87	8.84
FeO^T	6.13	5.39	5.49	8.02	10.66	11.54	6.19	6.19	6.91	6.85	6.78	5.75	5.16	5.52	5.75
MnO	8.11	8.41	8.45	10.33	9.68	9.44	8.24	8.24	9.74	9.95	10.02	9.02	7.73	9.40	8.97
MgO	3.69	3.88	3.79	2.72	2.62	2.77	3.83	3.83	3.22	2.97	2.30	3.36	3.82	3.42	3.44
CaO	1.07	1.07	1.11	0.68	0.76	0.77	0.91	0.91	0.53	0.55	0.65	0.67	0.94	0.66	0.65
Na_2O	1.25	1.25	1.09	0.68	0.89	0.59	1.08	1.08	0.68	0.66	0.70	1.00	1.12	0.99	1.02
K_2O	0.11	0.15	0.13	0.10	0.13	0.08	0.16	0.16	0.10	0.12	0.09	0.14	0.12	0.16	0.19
P_2O_5	0.24	0.25	0.23	0.09	0.10	0.07	0.21	0.21	0.10	0.10	0.09	0.14	0.23	0.15	0.14
H_2O	2.95	2.28	2.77	1.27	4.06	2.71	3.81	3.51	4.20	3.27	2.75	2.70	2.34	3.25	3.25
S ppm	651	684	611	931	953	942	711	783	1633	1075	1963	1005	1010	2021	1872
Cl ppm	618	645	598	1022	1024	1172	632	782	829	960	720	794	656	685	749
Fo	82.01	82.01	82.01	87.38	90.24	90.25	82.05	80.47	86.13	86.13	86.01	81.76	82.06	82.25	79.69

Table 1 (cont.): Major element and volatile compositions of melt inclusions, and host olivine composition (corrected values)

	Hoya Alvarez													
	HA-A_1	HA-A_1-2	HA-A_2	HA-A_3	HA-A_6	HA-A_7	HA-A_8	HA-A_10	HA-A_12	HA-A_13-1	HA-A_13-2	HA-A_14	HA-A_15	HA-A_17
SiO_2	46.35	46.60	46.74	45.81	47.59	46.17	47.29	48.07	46.98	46.40	46.40	46.96	49.40	47.30
TiO_2	18.19	18.14	17.36	18.46	17.81	18.10	17.59	16.72	17.57	17.33	17.46	17.79	16.97	17.41
Al_2O_3	12.17	12.25	11.10	11.89	11.02	11.89	12.01	12.19	12.27	12.32	12.27	12.18	13.01	11.91
FeO^T	4.96	5.03	6.49	5.80	5.14	5.52	5.77	5.18	5.31	6.27	6.23	4.91	3.06	3.77
MnO	8.40	8.44	7.81	8.46	8.43	8.48	8.02	7.66	8.16	8.56	8.53	8.32	6.54	7.54
MgO	4.14	3.44	3.11	3.95	4.23	4.19	4.02	4.63	4.10	3.99	4.05	4.10	5.19	4.76
CaO	1.83	1.86	1.57	1.71	1.85	1.70	1.74	1.82	1.86	1.82	1.76	1.80	2.52	2.37
Na_2O	3.21	3.45	2.94	3.16	3.18	3.20	2.70	2.98	2.99	2.58	2.52	3.13	2.00	3.04
K_2O	0.14	0.17	0.12	0.16	0.18	0.20	0.18	0.15	0.17	0.09	0.13	0.20	0.22	0.21
P_2O_5	0.61	0.63	0.59	0.60	0.59	0.55	0.57	0.59	0.60	0.63	0.64	0.60	1.11	0.78
H_2O	1.26	1.42	1.05	0.83	0.82	1.15	1.06	0.96	0.83	0.56	1.01	0.42	0.61	
S ppm	1180	1147	1040	1116	1101	948	806	979	950	1008.63	943	1101	1166	
Cl ppm	550	536	413	404	592	411	633	551	473	394.36	440	1002	684	
Fo	75.55	75.55	76.78	77.29		77.25	77.19	76.26	76.44	78.67	78.67	74.77	63.62	78.36

APPENDIX G

CALIBRATION FOR H_2O-TRACE ELEMENT CORRELATIONS

We tested the H_2O-trace element correlations by using them to calculate H_2O for melt inclusions in which H_2O had previously been measured by FTIR. This plot shows the calculated H_2O vs measured H_2O for the MGVF melts from this study as well as for volcanoes from the Chichináutzin Volcanic Field (CVF; Cervantes and Wallace, 2003). Shown in this plot are the 1-to-1 line (solid grey) and the root mean squared error (± 1.2, dotted lines).

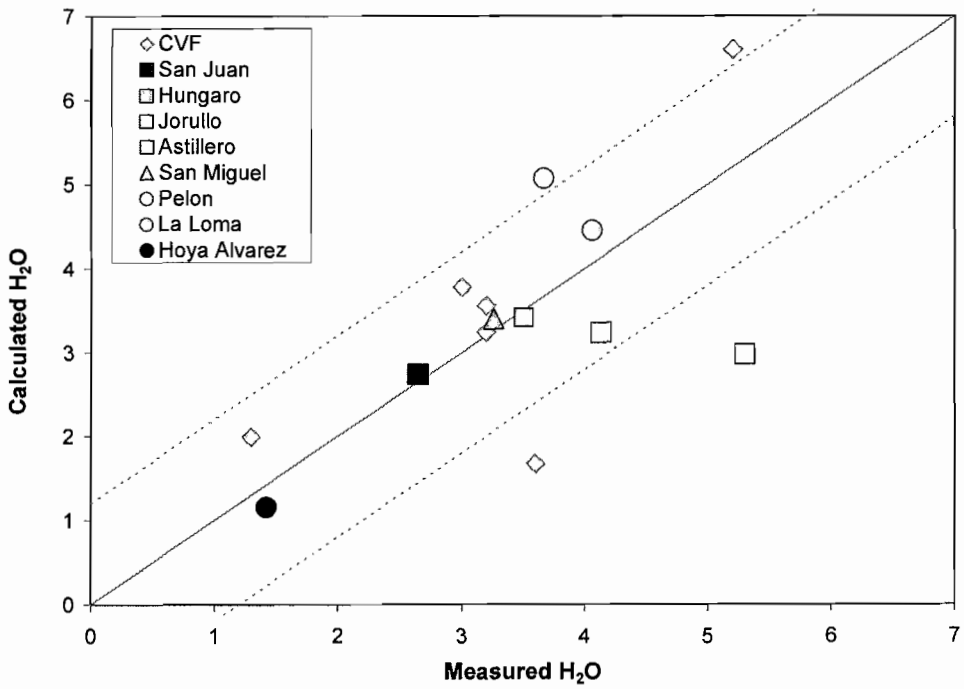

REFERENCES

Chapter II

Annen, C., Blundy, J.D., Sparks, R.S.J., 2006. The genesis of intermediate and silicic magmas in Deep Crustal Hot Zones. J. Petrol. 47 (3),.505-539.

Asimow, P.D., Ghiorso, M.S., 1998. Algorithmic modifications extending MELTS to calculate subsolidus phase relations. Amer. Mineral. 83, 1127-1131.

Atlas, Z.D., Dixon, J.E., Sen, G., Finny, M., Martin-Del Pozzo, A.L., 2006. Melt inclusions from Volcán Popocatépetl and Volcán de Colima, Mexico: Melt evolution due to vapor-saturated crystallization during ascent. J. Volcanol. Geotherm. Res. 153, 221-240.

Baker, D.R., Freda, C., Brooker, R.A., Scarlato, P., 2005. Volatile diffusion in silicate melts and its effects on melt inclusions. Annals of Geophysics 48 (4/5), 699-717.

Blundy, J., Cashman, K., Humphreys, M., 2006. Magma heating by decompression-driven crystallization beneath andesite volcanoes. Nature 443, 76-80.

Cervantes, P., Wallace, P.J., 2003. Role of H_2O in subduction-zone magmatism: New insights from melt inclusions in high-Mg basalts from central Mexico. Geology 31, 235-238.

Costa, F., Chakraborty, S., 2004. Decadal time gaps between mafic intrusion and silicic eruption obtained from chemical zoning patterns in olivine. Earth Planet. Sci. Lett. 227, 517-530.

Davidson, J., Turner, S., Handley, H., Macpherson, C., Dosseto, A., 2007. Amphibole "sponge" in arc crust? Geology 35 (9), 787-790.

Danyushevsky, L.V., Sokolov, S., Falloon, T.J., 2002. Melt inclusions in olivine phenocrysts: Using diffusive re-equilibration to determine the cooling history of a crystal, with implications for the origin of olivine-phyric volcanic rocks. J. Petrol. 43, 1651-1671.

Dixon, J.E., Stolper, E.M., Holloway, J.R., 1995. An experimental study of water and carbon dioxide solubilities in mid-ocean ridge basaltic liquids. Part I: Calibration and solubility models. J. Petrol. 36 (6), 1607-1631.

Dixon, J.E., Pan, V., 1995. Determination of the molar absorptivity of dissolved carbonate in basanitic glass. Amer. Mineral. 80 (11-12), 1339-1342.

Dohmen, R., Chakraborty, S., Palme, H., Rammensee, W., 2003. Role of element solubility on the kinetics of element partitioning: In situ observations and a thermodynamic kinetic model. J. Geophys. Res. 108, B3, 2157, doi: 10.1029/2002JB000587.

Gadow, H, 1930. Jorullo: The history of the volcano of Jorullo and the reclamation of the devastated district by animals and plants. Cambridge Univ. Press, London, p 101.

Ghiorso, M.S., Sack, R.O., 1995. Chemical mass transfer in magmatic processes. IV. A revised and internally consistent thermodynamic model for the interpolation and extrapolation of liquid-solid equilibria in magmatic systems at elevated temperatures and pressures. Contrib. Mineral. Petrol. 119, 197-212.

Ghiorso, M.S., Hirschmann, M.M., Reiners, P.W., Kress, V.C. III, 2002. The pMELTS: A revision of MELTS aimed at improving calculation of phase relations and major element partitioning involved in partial melting of the mantle at pressures up to 3 GPa. Geochemistry, Geophysics, Geosystems 3(5), doi: 10.1029/2001GC000217.

Gonnermann, H.M., Manga, M., 2005. Nonequilibrium magma degassing: Results from modeling of the ca. 1340 AD eruption of Mono Craters, California. Earth Planet. Sci. Lett. 238, 1-16.

Grove, T.L., Elkins-Tanton, L.T., Parman, S.W., Chatterjee, N., Müntener, O., Gaetani, G.A., 2003. Fractional crystallization and mantle-melting controls on calc-alkaline differentiation trends. Contrib. Mineral. Petrol. 145, 515-533.

Hasenaka, T., Carmichael, I.S.E., 1985. The cinder cones of Michoacán-Guanajuato, central Mexico: Their age, volume and distribution, and magma discharge rate. J. Volcanol. Geotherm. Res. 25, 105-124.

Hildreth, W., Moorbath, S., 1988. Crustal contributions to arc magmatism in the Andes of central Chile. Contrib. Mineral. Petrol. 98, 455-489.

Holloway, J.R., 1973. The system pargasite-H_2O-CO_2: a model for melting of a hydrous mineral with a mixed-volatile fluid – I. Experimental results to 8 kbar. Geochim. Cosmochim. Acta 37, 651-666.

Holloway, J.R., Ford, C.E., 1975. Fluid absent melting of the fluorohydroxy-amphibole pargasite to 35 kilobars. Earth Planet. Sci. Lett. 25, 44-48.

Jurewicz, A.J.G., Watson, E.B., 1988. Cations in olivine: Part 2. Diffusion in olivine xenocrysts, with applications to petrology and mineral physics. Contrib. Mineral. Petrol. 99, 186-201.

Kent, A. J. R., Stolper, E. M., Francis, D., Woodhead, J., Frei, R., Eiler, J., 2004. Mantle heterogeneity during the formation of the North Atlantic Tertiary Province: Constraints from trace element and Sr-Nd-Os-O isotope systematics of Baffin Island picrites. Geochemistry Geophysics Geosystems (5), Q11004, DOI: 10.1029/2004GC000743

Krauskopf, K., 1948. Mechanism of eruption at Parícutin volcano, México. Geol. Soc. Amer. Bull. 59, 711-731.

Luhr, J.F., and Carmichael, I.S.E., 1985. Jorullo Volcano, Michoacán, Mexico (1759-1774): The earliest stages of fractionation in calc-alkaline magmas. Contrib. Mineral. Petrol. 90, 142-161.

Luhr, J.F., 2001. Glass inclusions and melt volatile contents at Parícutin Volcano, Mexico. Contrib. Mineral. Petrol. 142, 261-283.

McBirney, A.R., Taylor, H.P. Jr., Armstrong, R.L., 1987. Parícutin re-examined: a classic example of crustal assimilation in calc-alkaline magma. Contrib. Mineral. Petrol. 95, 4-20.

Métrich, N., Bertagnini, A., Landi, P., Rosi, M., 2001. Crystallization driven by decompression and water loss at Stromboli Volcano (Aeolian Islands, Italy). J. Petrol. 42, 1471-1490.

Moore, G., Carmichael, I.S.E., 1998. The hydrous phase equilibria (to 3 kbar) of and andesite and basaltic andesite from western Mexico: constraints on water content and conditions of phenocrysts growth. Contrib. Mineral. Petrol. 130, 304-319.

Newman, S., Lowenstern, J.B., 2002. VolatileCalc: a silicate melt-H_2O-CO_2 solution model written in VISUAL BASIC Excel. Computat. Geosci. 28, 597-604.

Nicholis, M.G., Rutherford, M.J., 2004. Experimental constraints on magma ascent rate for the Crater Flat volcanic zone hawaiite. Geology 32 (6), 489-492.

Pardo, M., Suárez, G., 1995. Shape of the subducted Rivera and Cocos plates in southern Mexico: Seismic and tectonic implications. J. Geophys. Res. 100 (B7), 12357-12373.

Pioli, L., Cashman, K.V., 2006. Application of two-phase flow models along vertical pipes for the description of basaltic explosive volcanic activity. Eost Trans. AGU, 87 (52), Fall Meet. Suppl., Abstract V43C-1812.

Portnyagin, M., Almeev, R., 2007. Experimental evidence for rapid re-equilibration of water between melt inclusions in olivine and host magma. Geochim. Cosmochim. Acta 71 (15), A804.

Roberge, J., Wallace, P.J., White, R.V., Coffin, M.F., 2005. Anomalous uplift and subsidence of the Ontong Java Plateau inferred from CO_2 contents of submarine basaltic glasses. Geology 33 (6), 501-504.

Roggensack, K., Hervig, R.L., McKnight, S.B., Williams, S.N., 1997. Explosive basaltic volcanism from Cerro Negro volcano: Influence of volatiles on eruptive style. Science 277, 1639-1642.

Roggensack, K., 2001. Sizing up crystals and their melt inclusions; a new approach to crystallization studies. Earth Planet. Sci. Lett. 187, 221-237.

Rubin, K.H., Jurado-Chichay, Z., Pyle, D., Morán-Zenteno, D., Rowland, S., 2004. El Jorullo revisited: Petrology, geochemistry & volcanology. Eos Trans. – Am. Geophys. Union 85(47), Fall Meet. Suppl., Abstract V13B-1485.

Rust, A.C., Cashman, K.V., Wallace, P.J., 2004. Magma degassing buffered by vapor flow through brecciated conduit margins. Geology 32, 349-352.

Rust, A., Blundy, J., Cashman, K., 2007. Melt CO_2 enrichment by permeable flow and resorption. Eos Trans., AGU, 88 (52), Fall Meet. Suppl., Abstract V21C-0729.

Sisson, T.W., Layne, G.D., 1993. H_2O in basalt and basaltic andesite glass inclusions from four subduction-related volcanoes. Earth Planet. Sci. Lett. 117, 619-635.

Sobelev, A.V., Chaussidon, M., 1996. H_2O concentrations in primary melts from supra-subduction zones and mid-ocean ridges; implications for H_2O storage and recycling in the mantle. Earth Planet. Sci. Lett. 137 (1-4), 45-55.

Spilliaert, N., Allard, P., Métrich, N., Sobolev, A.V., 2006. Melt inclusion record of the conditions of ascent, degassing, and extrusion of volatile-rich alkali basalt during the powerful 2002 flank eruption of Mount Etna (Italy). J. Geophys. Res. 111, doi: 10.1029/2005JB003934.

Sugawara, T., 2000. Empirical relationships between temperature, pressure, and MgO content in olivine and pyroxene saturated liquid. J. Geophys. Res. 105 (B4), 8457-8472.

Valentine, G.A., Krogh, K.E.C., 2006. Emplacement of shallow dikes and sills beneath a small basaltic volcanic center – The role of pre-existing structure (Paiute Ridge, southern Nevada, USA). Earth Planet. Sci. Lett. 246, 217-230.

Vespermann, D., Schmincke, H.-U., 2002. Scoria cones and tuff rings, in: Sigurdsson, H., Houghton, B.F., McNutt, S.R., Rymer, and H., Stix, J. (Eds.), Encyclopedia of Volcanoes, Academic Press, San Diego, pp. 683-694.

Wade, J.A., Plank, T., Melson, W.G., Soto, G.J., Hauri, E.H., 2006. The volatile content of magmas from Arenal volcano, Costa Rica. J. Volcanol. Geotherm. Res. 157, 94-120.

Wallace, P.J., 2005. Volatiles in subduction zone magmas; concentrations and fluxes based on melt inclusion and volcanic gas data. J. Volcanol. Geotherm. Res. 140 (1-3), 217-240.

Wilcox, R.E., 1954. Petrology of Paricutin volcano, Mexico. U.S. Geol. Surv. Bull. Pp. 281-354.

Wood, C.A., 1980. Morphometric evolution of cinder cones. J. Volcanol. Geotherm. Res. 7, 387-413.

Chapter III

Atlas, Z.D., Dixon, J.E., Sen, G., Finny, M., Martin-Del Pozzo, A.L., 2006. Melt inclusions from Volcán Popocatépetl and Volcán de Colima, Mexico: Melt evolution due to vapor-saturated crystallization during ascent. J. Volcanol. Geotherm. Res. 153, 221-240.

Baker, D.R. 2008. The fidelity of melt inclusions as records of melt composition. Contrib. Mineral. Petrol. DOI 10.1007/s00410-008-0291-3.

Benjamin, E.R., Plank, T., Wade, J.A., Kelley, K.A., Hauri, E.H., Alvarado, G.E., 2007. High water contents in basaltic magmas from Irazú Volcano, Costa Rica. J. Volcanol. Geotherm. Res. 168, 68-92.

Blundy, J., Cashman, K. 2005. Rapid decompression-driven crystallization recorded by melt inclusions from Mount St. Helens volcano. Geology 33, 793-796.

Blundy, J., Cashman, K., Humphreys, M., 2006. Magma heating by decompression-driven crystallization beneath andesite volcanoes. Nature 443, 76-80.

Cervantes, P., Wallace, P.J., 2003. Role of H_2O in subduction-zone magmatism: New insights from melt inclusions in high-Mg basalts from central Mexico. Geology 31, 235-238.

Danyushevsky, L.V., Sokolov, S., Falloon, T.J., 2002. Melt inclusions in olivine phenocrysts: Using diffusive re-equilibration to determine the cooling history of a crystal, with implications for the origin of olivine-phyric volcanic rocks. J. Petrol. 43, 1651-1671.

Dixon, J.E., Pan, V., 1995. Determination of the molar absorptivity of dissolved carbonate in basanitic glass. Amer. Mineral. 80 (11-12), 1339-1342.

Dixon, J.E., Stolper, E.M., Holloway, J.R., 1995. An experimental study of water and carbon dioxide solubilities in mid-ocean ridge basaltic liquids. Part I: Calibration and solubility models. J. Petrol. 36 (6), 1607-1631.

Faure F, Schiano P (2005) Experimental investigation of equilibration conditions during forsterite growth and melt inclusion formation. Earth Planet. Sci. Lett. 236, 882–898

Gurenko, A.A., Belousov, A.B., Trumbull, R.B., Sobolev, A.V., 2005. Explosive basaltic volcanism of the Chikurachki Volcano (Kurile arc, Russia): Insights on pre-eruptive magmatic conditions and volatile budget revealed from phenocrysts-hosted melt inclusions and groundmass glasses. J. Volcanol. Geotherm. Res. 147, 203-232.

Hasenaka, T., Carmichael, I.S.E., 1985. The cinder cones of Michoacán-Guanajuato, central Mexico: Their age, volume and distribution, and magma discharge rate. J. Volcanol. Geotherm. Res. 25, 105-124.

Johnson, E.R., Wallace, P.J., Cashman, K.V., Delgado Granados, H., Kent, A.J.R., 2008. Magmatic volatile contents and degassing-induced crystallization at Volcán Jorullo, Mexico: Implications for melt evolution and the plumbing systems of monogenetic volcanoes. Earth Planet. Sci. Lett. doi:10.1016/j.epsl.2008.03.004.

Jugo, P.J., Luth, R.W., Richards, J.P., 2005. An experimental study of the sulfur content in basaltic melts saturated with immiscible sulfide or sulfate liquids at 1300°C and 1.0 GPa. J. Petrol. Doi:10.1093/petrology/egh097.

Luhr, J.F., and Carmichael, I.S.E., 1985. Jorullo Volcano, Michoacán, Mexico (1759-1774): The earliest stages of fractionation in calc-alkaline magmas. Contrib. Mineral. Petrol. 90, 142-161.

Luhr, J.F., 2001. Glass inclusions and melt volatile contents at Parícutin Volcano, Mexico. Contrib. Mineral. Petrol. 142, 261-283.

Mastin, L.G., Christiansen, R.L., Thornber, C., Lowenstern, J., Beeson, M., 2004. What makes hydromagmatic eruptions violent? Somet insights from the Kanakako'I Ash, Kilauea Volcano, Hawai'i. J. Volcanol. Geotherm. Res. 137, 15-31.

McBirney, A.R., Taylor, H.P. Jr., Armstrong, R.L., 1987. Parícutin re-examined: a classic example of crustal assimilation in calc-alkaline magma. Contrib. Mineral. Petrol. 95, 4-20.

Metrich, N., Clocchiatti, R., Mosbah, M., Chaussidon, M., 1993. The 1989-90 activity of Etna. Magma mingling and ascent of a H2O-Cl-S rich basalt. Evidence from the melt inclusions. J. Volcanol. Geotherm. Res. 59, 131-144.

Métrich, N., Bertagnini, A., Landi, P., Rosi, M., 2001. Crystallization driven by decompression and water loss at Stromboli Volcano (Aeolian Islands, Italy). J. Petrol. 42, 1471-1490.

Newman, S., Lowenstern, J.B., 2002. VolatileCalc: a silicate melt-H_2O-CO_2 solution model written in VISUAL BASIC Excel. Computat. Geosci. 28, 597-604.

Roggensack, K., Hervig, R.L., McKnight, S.B., Williams, S.N., 1997. Explosive basaltic volcanism from Cerro Negro volcano: Influence of volatiles on eruptive style. Science 277, 1639-1642

Sisson, T.W., Layne, G.D., 1993. H_2O in basalt and basaltic andesite glass inclusions from four subduction-related volcanoes. Earth Planet. Sci. Lett. 117, 619-635.

Sobelev, A.V., Chaussidon, M., 1996. H_2O concentrations in primary melts from supra-subduction zones and mid-ocean ridges; implications for H_2O storage and recycling in the mantle. Earth Planet. Sci. Lett. 137 (1-4), 45-55.

Spilliaert, N., Allard, P., Métrich, N., Sobolev, A.V., 2006a. Melt inclusion record of the conditions of ascent, degassing, and extrusion of volatile-rich alkali basalt during the powerful 2002 flank eruption of Mount Etna (Italy). J. Geophys. Res. 111, doi: 10.1029/2005JB003934.

Spilliaert, N., Metrich, N., Allard, P., 2006b. S-Cl-F degassing pattern of water-rich alkali basalt: Modelling and relationship with eruption styles on Mount Etna volcano. Earth Planet. Sci. Lett.,

Vespermann, D., Schmincke, H.-U., 2002. Scoria cones and tuff rings, in: Sigurdsson, H., Houghton, B.F., McNutt, S.R., Rymer, and H., Stix, J. (Eds.), Encyclopedia of Volcanoes, Academic Press, San Diego, pp. 683-694.

Wade, J.A., Plank, T., Melson, W.G., Soto, G.J., Hauri, E.H., 2006. The volatile content of magmas from Arenal volcano, Costa Rica. J. Volcanol. Geotherm. Res. 157, 94-120.

Wallace, P.J., Carmichael, I.S.E., 1994. Sulfur speciation in submarine basaltic glasses as determined by measurements of SKα X-ray wavelength shifts. Am. Mineral. 79, 161-167.

Wallace, P.J., 2005. Volatiles in subduction zone magmas; concentrations and fluxes based on melt inclusion and volcanic gas data. J. Volcanol. Geotherm. Res. 140 (1-3), 217-240.

Webster, J.D., Kinzler, R.J., Mathez, E.A., 1999. Chloride and water solubility in basalt and andesite melts and implications for magmatic degassing, Geochim. Cosmochim. Acta, 63, 729-738.

Chapter IV

Abers, G.A., T. Plank, and B.R. Hacker (2003) The wet Nicaraguan slab, *Geophys. Res. Lett., 30*, doi:10.1029/2992GL015649.

Abers, G.A., P.E. van Keken, E.A. Kneller, A. Ferris, and J.C. Stachnik (2006), The thermal structure of subduction zones constrained by seismic imaging: Implications for slab dehydration and wedge flow, *Earth Planet. Sci. Lett., 241*, 387-397.

Alt, J.C., K. Muehlenbacks, and J. Honnorex (1986), An oxygen isotopic profile through the upper kilometer of the oceanic crust, DSDP hole 504B, *Earth Planet. Sci. Lett., 80*, 217-229.

Alt, J.C., and W.C. Shanks III (2006), Stable isotope compositions of serpentinite seamounts in the Mariana forearc: Serpentinization processes, fluid sources and sulfur metasomatism, *Earth Planet. Sci. Lett., 242*, 272-285.

Arthur, M.A., T.F. Anderson, and I.R. Kaplan (1983), *Stable Isotopes in Sedimentary Geology, SEPM Short Course*, 10, 432 pp.

Ban, M., T. Hasenaka, H. Delgado-Granados, and N Takaoka (1992), K-Ar ages of lavas from shield volcanoes in the Michoacan-Guanajuato volcanic field, Mexico, *Geofisica Internacional, 31*, 467-473.

Baker, M. B. and E. M. Stolper (1994), Determining the composition of high-pressure mantle melts using diamond aggregates, *Geochim. Cosmochim. Acta., 58*, 2811-2827.

Benjamin, E.R., T. Plank, J.A. Wade, K.A. Kelley, E.H. Hauri, and G.E. Alvarado (2007), High water contents in basaltic magmas from Irazú Volcano, Costa Rica, *J. Volcanol. Geotherm. Res., 168*, 68-92, doi:10.1016/j.jvolgeores.2007.08.008.

Blatter, D.L., I.S.E. Carmichael, A.L. Deino, and P.R. Renne (2001), Neogene volcanism at the front of the central Mexican volcanic belt: Basaltic andesites to dacites, with contemporaneous shoshonites and high-TiO2 lava, *GSA Bull., 113*, 1324-1342.

Blatter, D.L., G.L. Farmer, and I.S.E. Carmichael (2007), A north-south transect across the Central Mexican Volcanic Belt at ~100°W: Spatial distribution, petrological, geochemical, and isotopic characteristics of Quaternary volcanism, *J. Petrol., 48*, 901-950.

Carr, M.J., M.D. Feigenson, and E.A. Bennett (1990), Incompatible element and isotopic evidence for tectonic control of source mixing and melt extraction along the Central American arc, *Contrib. Mineral. Petrol., 105*, 369-380.

Cervantes, P., and P.J. Wallace (2003), Role of H_2O in subduction-zone magmatism: New insights from melt inclusions in high-Mg basalts from central Mexico, *Geology, 31*, 235-238.

Danyushevsky, L.V., S. Sokolov, and T.J. Falloon (2002), Melt inclusions in olivine phenocrysts: Using diffusive re-equilibration to determine the cooling history of a crystal, with implications for the origin of olivine-phyric volcanic rocks, *J. Petrol., 43*, 1651-1671.

Davidson, J., S. Turner, H. Handley, C. Macpherson, and A. Dosseto, (2007), Amphibole "sponge" in arc crust? *Geology, 35*, 787-790.

Dixon, J.E., E.M. Stolper, and J.R Holloway (1995), An experimental study of water and carbon dioxide solubilities in mid-ocean ridge basaltic liquids. Part I: Calibration and solubility models, *J. Petrol., 36*, 1607-1631.

Dixon, J.E., and V. Pan (1995), Determination of the molar absorptivity of dissolved carbonate in basanitic glass, *Amer. Mineral., 80*, 1339-1342.

Dixon J.E., D.A. Clague, P. Wallace, and R. Poreda (1997), Volatiles in alkalic basalts from the North Arch volcanic field, Hawaii: Extensive degassing of deep submarine-erupted alkalic series lavas, *J. Petrol. 38*(7) 911-939.

Dorendorf, F., U. Wiechert, and G. Wörner (2000), Hydrated sub-arc mantle: a source for the Kluchevskoy volcano, Kamchatka/Russia, *Earth Planet. Sci. Lett.*, 175, 69-86.

Eiler, J.M., A. Crawford, T. Elliott, K.A. Farley, J.W. Valley, and E.M. Stolper (2000a), Oxygen isotopic geochemistry of oceanic arc lavas, *J. Petrol., 41*, 229-256.

Eiler, J.M. (2001), Oxygen isotope variations of basaltic lavas and upper mantle rocks, in *Stable Isotope Geochemistry*, edited by J.W. Valley and D.R. Cole, *Rev. Mineral. Geochem., 43*, 319-364.

Eiler, J.M., M.J. Carr, M. Reagan, and E. Stolper (2005), Oxygen isotope constraints on the sources of Central American arc lavas, *Geochem. Geophys. Geosyst.*, *6*, Q07007, doi:10.1029/2004GC000804.

Eiler, J. M., P. Schiano, J. W. Valley, N. T. Kita, and E. M. Stolper (2007), Oxygen-isotope and trace element constraints on the origins of silica-rich melts in the subarc mantle, *Geochem. Geophys. Geosyst.*, *8*, Q09012, doi:10.1029/2006GC001503.

Ferrari, L., V.H. Garduno, G. Pasquare, and A Tibaldi (1994), Volcanic and tectonic evolution of central Mexico: Oligocene to present, *Geofis. Int., 33*, 91-105.

Gaetani, G.A., T.L. Grove, and W.B. Bryan (1993), The influence of water on the petrogenesis of subduction-related igneous rocks, *Nature*, *365*, 332-334.

Gaetani, G.A., and T.L. Grove (1998), The influence of water on melting of mantle peridotite, *Contrib. Mineral. Petrol.*, *131*, 323-346.

Ghiorso, M.S., and R.O. Sack (1995), Chemical mass transfer in magmatic processes. IV. A revised and internally consistent thermodynamic model for the interpolation and extrapolation of liquid-solid equilibria in magmatic systems at elevated temperatures and pressures, *Contrib. Mineral. Petrol.*, *119*, 197-212.

Gomez-Tuena, A., C.H. Langmuir, S.L. Goldstein, S.M. Straub, and F. Ortega-Gutierrez (2007), Geochemical Evidence for slab melting in the Trans-Mexican Volcanic Belt, *J. Petrol., 48,* 537-562.

Grove, T.L., N. Chatterjee, S.W. Parman, and E. Médard (2006), The influence of H_2O on mantle wedge melting, *Earth Planet. Sci. Lett.*, *249*, 74-89, doi:10.1016/j.epsl.2006.06.043.

Harmon, R.S., and J. Hoefs (1995), Oxygen isotope heterogeneity of the mantle deduced from global ^{18}O systematics of basalts from different geotectonic settings, *Contrib. Mineral. Petrol.*, *120*, 95-114.

Hasenaka, T. and I. S. E. Carmichael (1985), The cinder cones of Michoacan Guanajuato, central Mexico: Their age, volume and distribution and magma discharge rate, *J. Vol. Geotherm. Res. 25*(1-2), 105-124.

Hochstaedter, A.G., J.G. Ryan, J.F. Luhr, and T. Hasenaka (1996), On B/Be ratios in the Mexican Volcanic Belt, *Geochim. Cosmochim. Acta*, *60*, 613-628.

Johnson, M.C., and T. Plank (1999), Dehydration and melting experiments constrain the fate of subducted sediments, *Geochem. Geophys. Geosyst.*, *1*, Paper number 1999GC000014.

Johnson, E.R., P.J. Wallace, K.V. Cashman, H. Delgado Granados, and A. Kent (2008), Magmatic volatile contents and degassing-induced crystallization at Volcán Jorullo, Mexico: Implications for melt evolution and the plumbing systems of monogenetic volcanoes, *Earth Planet. Sci. Lett.*, doi:10.1016/j.epsl.2008.03.004.

Kelemen, P.B., G.M. Yogodzinski, and D.W. Scholl (2003), Along strike variation in the Aleutian Island arc: Genesis of high Mg# andesite and implications for continental crust, in *The Subduction Factory, Geophys. Monogr. Ser.*, vol.138. edited by J. Eiler, pp. 223-276, AGU, Washington, D.C.

Kelley, K.A., T. Plank, T.L. Grove, E.M. Stolper, S. Newman, and E. Hauri (2006), Mantle melting as a function of water content beneath back-arc basins, *J. Geophys. Res., 111*, B09208, doi:10.1029/2005JB003732.

Kent, A. J. R., E. M. Stolper, D. Francis, J. Woodhead, R. Frei, and J. Eiler (2004), Mantle heterogeneity during the formation of the North Atlantic Tertiary Province: Constraints from trace element and Sr-Nd-Os-O isotope systematics of Baffin Island picrites, *Geochem. Geophys. Geosyst., 5*, Q11004, DOI: 10.1029/2004GC000743

Kerrick, D.M., and J.A.D. Connolly (2001), Metamorphic devolatilization of subducted marine sediments and the transport of volatiles into the Earth's mantle, *Nature, 411*, 293-296.

Kessel, R., M.W. Schmidt, P. Ulmer, and T. Pettke (2005), Trace element signature of subduction-zone fluids, melts and supercritical liquids at 120-180 km depth, *Nature, 437*, doi:10.0038/nature03971.

Kolodny, Y. and S. Epstein (1976), Stable isotope geochemistry of deepsea cherts, *Geochim. Cosmochim. Acta, 40*, 1195-1209.

Lagatta, A. (2003), Arc magma genesis in the eastern Mexican volcanic belt, Ph.D. thesis, Columbia University, New York.

Luhr, J. (1997), Extensional tectonics and the diverse primitive volcanic rocks in the western Mixican volcanic belt, *Can. Mineral., 35*, 473-500.

Manea, V.C., M. Manea, V. Kostoglodov, C. Currie, and G. Sewell (2004), Thermal structure, coupling and metamorphism in the Mexican subduction zone beneath Guerrero. *Geophys. J. Int., 58*, 775–784.

Manea, V.C., M.Manea, V. Kostoglodov, and G. Sewell (2005), Thermo-mechanical model of the mantle wedge in Central Mexican stubduction zone and a blob tracing approach for the magma transport, *Earth Planet. Sci. Lett., 149*, 165-186.

Mattey, D., D. Lowry, and C. Macpherson (1994), Oxygen isotope composition of mantle peridotite, *Earth Planet. Sci. Lett.*, *128*, 231-241.

McMillan, N.J., A.P. Dickin, and K. Haag (2000), Evolution of magma source regions in the Rio Grande rift, southern New Mexico, *GSA Bull.*, *112*, 1582-1593.

Nichols, G.T., P.J. Wyllie, and C.R. Stern (1996), Experimental melting of pelagic sediment: Constraints relevant to subduction, *in Subduction: Top to Bottom, Geophys. Monogr. Ser., vol. 96*, edited by G.E. Bebout et al., pp. 293-298, AGU, Washington, D.C.

Nixon, G.T., A Demant, R.L. Armstrong, and J.E. Harakal (1987), K-Ar and geoligc data bearing on the age and evolution of the Trans-Mexican Volcanic Belt, *Geofis. Int., 26,* 109-158.

Ownby, S., H. Delgado Granados, R. A. Lange, and C. M. Hall (2007), Volcan Tancitaro, Michoacan, Mexico, $^{40}Ar/^{39}Ar$ constraints on its history of sector collapse, *J. Vol. Geotherm. Res. 161*(1-2), 1-14.

Pardo, M., and G. Suárez (1995), Shape of the subducted Rivera and Cocos plates in southern Mexico: seismic and tectonic implications, *J. Geophys. Res.*, *100*, 12,357-12,373.

Pearce, J.A. and D.W. Peate (1995), Tectonic implications of the composition of volcanic arc magmas, *Annual Rev. Earth Planet. Sci.*, *23*, 251-285.

Plank, T., and C.H. Langmuir (1992), Effects of the melting regimen on the composition of the oceanic crust, *J. Geophys. Res.*, *97*, 19,749-19,770.

Plank, T. and C.H. Langmuir (1998), The chemical composition of subducting sediment and its consequences for the crust and mantle, *Chem. Geol. 143,* 325-394.

Portnyagin, M., K. Hoernle, P. Plechov, N. Mironov, and S. Khubunaya (2007), Constraints on mantle melting and composition and nature of slab components in volcanic arcs from volatiles (H_2O, S, Cl, F) and trace elements in melt inclusions from the Kamchatka Arc, *Earth Planet. Sci. Lett.*, *255*, 53-69.

Plank, T. (2005), Constraints from thorium/lanthanum on sediment recycling at subduction zones and the evolution of the continents, *J. Petrol.*, *46*, 921-944.

Roggensack, K., R.L. Hervig, S.B. McKnight, and S.N. Williams (1997), Explosive basaltic volcanism from Cerro Negro volcano: Influence of volatiles on eruptive style, *Science*, *277*, 1639-1642.

Roggensack, K. (2001), Unraveling the 1974 eruption of Fuego volcano (Guatemala) with small crystals and their young melt inclusions, *Geology*, *29*, 911-914.

Rüpke, L.H., J.P. Morgan, M. Hort, and J.A.D. Connolly (2002), Are the regional variations in Central American arc lavas due to differing basaltic versus peridotitic slab sources of fluids?, *Geology*, *30*, 1035-1038.

Rüpke, L.H., J.P. Morgan, M. Hort, and J.A.D. Connolly (2004), Serpentine and the subduction zone water cycle, *Earth Planet. Sci. Lett.*, *223*, 17-34.

Sadofsky, S.J., M. Portnyagin, K. Hoernle, and P. van den Bogaard (2007), Subduction cycling of volatiles and trace elements through the Central American volcanic arc: evidence from melt inclusions, *Contrib. Mineral. Petrol.*, doi:10.1007/s00410-007-0251-3.

Salters, V.J.M., and A. Stracke (2004), Composition of the depleted mantle, *Geochem. Geophys. Geosyst.*, *5*, Q05B07, doi:10.1029/2003GC000597.

Scambelluri, M., O. Muntener, L. Ottolini, T.T. Pettke, and R. Vannucci (2004), The fate of B, Cl and Li in the subducted oceanic mantle and in the antigorite breakdown fluids, *Earth Planet. Sci. Lett., 222*, 217-234.

Schmidt, M.W. and S. Poli (1998), Experimentally based water budgets for dehydrating slabs and consequences for arc magma generation, *Earth Planet. Sci. Lett.*, *163*, 361-379.

Schmidt, M.W., and S. Poli (2004) Generation of mobile components during subduction of oceanic crust, in *Treatise on Geochemistry Volume 3: The Crust* Elsevier Ltd., Oxford, UK, p. 567-591, edited by R.L. Rudnick, H.D. Hollard, and K.K. Turekian.

Siebert, L. G. Carrasco-Nunez (2002), Late Pleistocene to precolumbian behind-the-arc mafic volcanism in the eastern Mexican Volcanic Belt; implications for future hazards, *J. Volcanol. Geotherm. Res., 115*, 179-205.

Singer, B.S., B.R. Jicha, W.P. Leeman, N.W. Rogers, M.F. Thirwall, J. Ryan, and K.E. Nicolaysen (2007), Along-strike trace element and isotopic variation in Aleutian Island arc basalt: Subduction melts sediments and dehydrates serpentine, *J. Geophys. Res.*, *112*, B06206, doi:10.1029/2006JB004897.

Sisson, T.W., and S. Bronto (1998), Evidence for pressure-release melting beneath magmatic arcs from basalt at Galunggung, Indonesia, *Nature*, *391*, 883-886.

Sisson, T.W., and T.L. Grove (1993a), Experimental investigations of the role of H_2O in calc-alkaline differentiation and subduction zone magmatism, *Contrib. Mineral. Petrol.*, *113*, 143-166.

Sisson, T.W., and T.L. Grove (1993b), Temperatures and H_2O contents of low-MgO high-alumina basalts, *Contrib. Mineral. Petrol.*, *113*, 167-184.

Sisson, T.W., and G.D. Layne (1993), H_2O in basalt and basaltic andesite glass inclusions from four subduction-related volcanoes, *Earth Planet. Sci. Lett.*, *117*, 619-635.

Sobelev, A.V. and M. Chaussidon (1996), H_2O concentrations in primary melts from supra-subduction zones and mid-ocean ridges; implications for H_2O storage and recycling in the mantle, *Earth Planet. Sci. Lett,. 137*, 45-55.

Spandler, C., J. Hermann, K. Faure, J.A. Mavrogenes, and R.J. Arculus (2008), The importance of talc and chlorite "hybrid" rocks for volatile recycling through subduction zones; evidence from the high-pressure subduction mélange of new Caledonia, *Contrib. Mineral. Petrol., 155*, doi:10.1007/s00410-007-0236-2.

Staudigel, H., G.R. Davies, S.R. Hart, K.M. Marchant, and B.M. Smith (1995), Large-scale isotopic Sr, Nd and O isotopic anatomy of altered oceanic crust – DSDP/ODP sites 417/418, *Earth Planet. Sci. Lett.*, *130*, 169-185.

Stolper, E., and S. Newman (1994), The role of water in the petrogenesis of Mariana trough magmas, *Earth Planet. Sci. Lett.*, *121*, 293-325.

Sun, S., and W.F. McDonough (1989), Chemical and isotopic systematics of oceanic basalts: implications for mantle composition and processes, in: *Magmatism in the Ocean Basins,* edited by A.D. Saunders and M.J. Norry, Geological Society, London, 1989, pp. 313– 345.

Suter M., M. L. Martinez, O. Q. Legorreta, and M. C. Martinez (2001), Quaternary intra-arc extension in the central Trans-Mexican volcanic belt, *Geol. Soc. Am. Bull. 133*(6), 693-703.

Toplis, M. J. (2005), The thermodynamics of iron and magnesium partitioning between olivine and liquid: criteria for assessing and predicting equilibrium in natural and experimental systems *Contrib. Min. Petrol. 149*(1), 22-39, doi: 10.1007/s00410-004-0629-4 .

Verma, S. (2000), Geochemistry of the subducting Cocos plate and the origin of subduction-unrelated mafic volcanism at the front of the central Mexican Volcanic Belt, in *Cenozoic Tectonics and Volcanism of Mexico*, edited by H. Delgado-Granados, G. Aguirre-Dias, and J. Stock, *Geological Society of America, Special Papers, 334*, 1-28.

Wade, J.A., T. Plank, W.G. Melson, G.J. Soto, and E.H. Hauri (2006), The volatile content of magmas from Arenal volcano, Costa Rica, *J. Volcanol. Geotherm. Res.*, *157*, 94-120, doi:10.1016/j.jvolgeores.2006.03.045

Wallace, P.J. and I.S.E. Carmichael (1994) Sulfur speciation submarine basaltic glasses as determined by measurements of SKα X-ray wavelength shifts, *Am. Mineral.*, *79*, 161-167.

Wallace, P.J. and A.T. Anderson (1998), Effects of eruption and lava drainback on the H_2O contents of basaltic magmas at Kilauea Volcano, *Bull. Volcanol.*, *50*, 327-344.

Workman, R. K., and S.R. Hart (2005), Major and trace element composition of the depleted MORB mantle (DMM), *Earth Planet. Sci. Lett.*, *231*, 53-72.

Wallace, P.J. (2005), Volatiles in subduction zone magmas; concentrations and fluxes based on melt inclusion and volcanic gas data, *J. Volcanol. Geotherm. Res.*, *140*, 217-240.

Walker, J.A., K. Roggensack, L.C. Patino, B.I. Cameron, and O. Matais (2003), The water and trace element contents of melt inclusions across as active subduction zone, *Contrib. Mineral. Petrol.*, *146*, 62-77.

Webster, J.D., R.J. Kinzler, and E.A. Mathez (1999), Chloride and water solubility in basalt and andesite melts and implications for magmatic degassing, *Geochim. Cosmochim. Acta, 63*, 729-738.

Wysoczanski, R.J., I.C. Wright, J.A. Gamble, E.H. Hauri, J.F. Luhr, S.M. Eggins, and M.R. Handler (2006), Volatile contents of Kermadec Arc-Havre Trough pillow glasses: Fingerprinting slab-derived aqueous fluids in the mantle sources of arc and back-arc lavas, *J. Volcanol. Geotherm. Res.*, *152*, 51-73, doi:10.1016/j.jvolgeores.2005.04.021.

Zheng, Y.F. (1993), Calculation of oxygen isotope fractionation in anhydrous silicate minerals, *Geochim. Cosmochim. Acta*, *57*, 1079-1091.